Investigation of τ Pair Production at PETRA

H. Küster
Institut für Kern- und Teilchenphysik

Kernforschungszentrum Karlsruhe
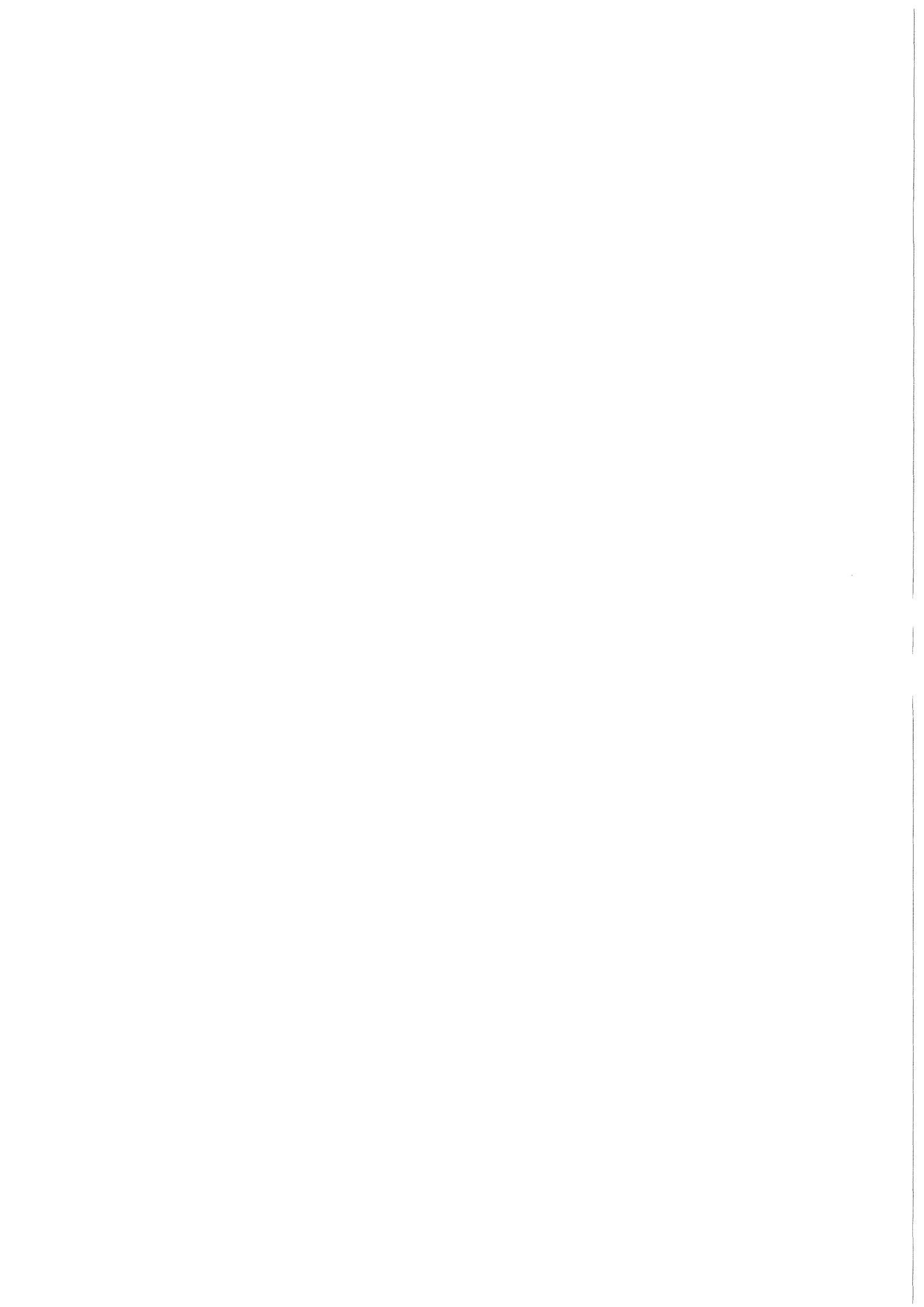
KERNFORSCHUNGSZENTRUM KARLSRUHE
Institut für Kern- und Teilchenphysik

KfK 3610

Investigation of τ Pair Production at PETRA

Hermann Küster

Kernforschungszentrum Karlsruhe GmbH, Karlsruhe

ABSTRACT

The reaction $e^+e^- \rightarrow \tau^+\tau^-$ has been measured at center of mass energies around 34 GeV. The selection is sensitive to 93 % of the τ pair decays, thus making possible a high identification efficiency of $\sim$ 70 % over a large solid angle. The total cross section has been measured to $R_\tau = \sigma_{\tau\tau}/\sigma_{point} = .94 \pm .06(\text{stat.}) \pm .06(\text{syst.})$. In the differential cross section a charge asymmetry of $A_\tau = -(9.0 \pm 6.6)$ % was observed, corresponding to a τ axial vector coupling to the weak neutral current of $a_\tau = -.94 \pm .69$.

Moreover, final states from the decays $\tau \rightarrow \pi\nu$, $\tau \rightarrow e\nu\nu$, and $\tau \rightarrow \mu\nu\nu$ have been isolated and branching ratios into these channels have been determined. From the inclusive momentum spectra of the observed decay products (including the channel $\tau \rightarrow \rho\nu$) the forward backward asymmetry of τ polarization has been determined to $A_{P,\tau} = -(1 \pm 22)$ % which corresponds to $v_\tau = -.1 \pm 2.9$. Tests on factorization are discussed.

ZUSAMMENFASSUNG

Die Reaktion $e^+e^- \rightarrow \tau^+\tau^-$ wurde untersucht bei Schwerpunktsenergien um 34 GeV. Die Selektion erfaßt 93 % der τ Paar Zerfälle, so daß eine hohe Nachweiswahrscheinlichkeit von $\sim$ 70 % über einen großen Raumwinkel möglich wurde. Der totale Wirkungsquerschnitt wurde gemessen zu $R_\tau = \sigma_{\tau\tau}/\sigma_{point} = .94 \pm .06(\text{stat.}) \pm .06(\text{syst.})$. Im differentiellen Wirkungsquerschnitt wurde eine Ladungsasymmetrie von $A_\tau = -(9.0 \pm 6.6)$ % beobachtet. Das entspricht einer Axialvektorkopplung des τ's an den schwachen neutralen Strom von $a_\tau = -.94 \pm .69$.

Außerdem wurden Endzustände aus den Zerfällen $\tau \rightarrow \pi\nu$, $\tau \rightarrow e\nu\nu$ und $\tau \rightarrow \mu\nu\nu$ isoliert und Verzweigungsverhältnisse für diese Kanäle bestimmt. Aus den inklusiven Impulsspektren der Zerfallsprodukte (einschließlich des Kanals $\tau \rightarrow \rho\nu$) wurde die Vorwärts-Rückwärts-Asymmetrie der τ-Polarisation bestimmt zu $A_{P,\tau} = -(1 \pm 22)$ %. Das entspricht $v_\tau = -.1 \pm 2.9$. Tests von Faktorisierung werden diskutiert.

CONTENTS

In 1946 it was found that the particle discovered in 1937 was not the long awaited pion, but rather a new kind of lepton. Since then, one of the greatest puzzles in particle physics is, why this new lepton, called muon, exists. The generation puzzle, introduced with the discovery of the muon, remained one of the most intriguing questions of physics and we have no clue of a solution yet.

Since the muon happens to exist in Nature, it is natural to ask whether there are further heavy leptons. The first experimental hint for such a new heavy lepton was the observation of an anomalously high rate of e μ events in e^+ e^- collisions at SPEAR by Perl and collaborators /1/ in 1975.

This observation was confirmed in 1976 by the results of an independent measurement by PLUTO at DORIS /2/. A final proof that these e μ events were not due to charm decay was the observation of τ production below charm threshold at the ψ' resonance by the DASP collaboration /3/.

The most natural way to explain those events was to assume pair production of a new heavy lepton.

Today the existence of the τ as a new lepton is firmly established and many of it's properties have been measured accurately /4/.

In the 'Standard Model' of electro weak interaction /5/ leptons and quarks are put into left handed isospin doublets and right handed singlets:

$$\begin{pmatrix} \nu_e \\ e \end{pmatrix}_L \quad \begin{pmatrix} \nu_\mu \\ \mu \end{pmatrix}_L \quad e_R, \quad \mu_R \qquad \begin{pmatrix} u \\ d \end{pmatrix}_L \quad \begin{pmatrix} c \\ s \end{pmatrix}_L \quad u_R, \quad d_R, \quad c_R, \quad s_R$$

If the neutrinos are massless there are no right handed neutrinos.

Today it can be shown that the τ must have its own neutrino /6/ (see " 1.3   Does the τ Have it's Own Neutrino ?" on page 16) and all measurements agree perfectly well with the interpretation of the τ as a new sequential heavy lepton, i.e. the τ together with it's associated neutrino ν_τ form a third generation in the 'Standard Model':

$$\begin{pmatrix} \nu_e \\ e \end{pmatrix} \quad \begin{pmatrix} \nu_\mu \\ \mu \end{pmatrix} \quad \begin{pmatrix} \nu_\tau \\ \tau \end{pmatrix}$$

This notion is backed further by the discovery of a new quark flavor (bottom) in 1977 /7/. So both the quark and the lepton sector are extended by a further generation to restore the old symmetry:

$$\begin{pmatrix} \nu_e \\ e \end{pmatrix}_L \quad \begin{pmatrix} \nu_\mu \\ \mu \end{pmatrix}_L \quad \begin{pmatrix} \nu_\tau \\ \tau \end{pmatrix}_L \qquad \begin{pmatrix} u \\ d \end{pmatrix}_L \quad \begin{pmatrix} c \\ s \end{pmatrix}_L \quad \begin{pmatrix} t? \\ b \end{pmatrix}_L$$

$$e_R, \quad \mu_R, \quad \tau_R \qquad u_R, \quad d_R, \quad c_R, \quad s_R, \quad t_R, \quad b_R$$

The only deficiency of this scheme is the fact that the sixth quark flavor (top) has still escaped detection, probably due to it's high mass (see for example /8/).

The purpose of this work has been on one hand the study of τ properties, and on the other the use of τ's for both, testing the validity of QED, and probe into electro weak interference effects in the PETRA energy range.

I will discuss here theoretical predictions on τ production and decay based on the interpretation of the τ as a conventional, sequential heavy lepton.

Further I will discuss predictions made by SU(2)×U(1) models of electro weak interaction on effects due to interference between γ and Z^0 exchange. These effects start to become observable at the highest PETRA energies.

1. THE τ AS A CONVENTIONAL SEQUENTIAL LEPTON

Today it is generally believed that the electromagnetic and weak interaction can be described by models based on a local SU(2)×U(1) gauge symmetry /9/.

The Standard Model is based on the two gauge groups SU(2) and U(1), corresponding to 4 gauge bosons:

W^+, W^3, W^- corresponding to the SU(2)$_L$ with coupling constant g
      B   corresponding to the U(1) with coupling constant g′

So we have two neutral currents with

$$L_{int,NC} = g \; T^3_\alpha W^{3\alpha} + g' \; Y_\alpha B^\alpha$$

The normal e.m. current can be identified as $j_\alpha = T^3_\alpha + Y_\alpha$.

To couple the photon to this current it has to be a linear combination of W^3 and B:

$$A_\alpha = \sin\Theta_W \; W^3_\alpha + \cos\Theta_W \; B_\alpha$$
$$Z_\alpha = \cos\Theta_W \; W^3_\alpha - \sin\Theta_W \; B_\alpha$$

Then the neutral current Lagrangian can be written as

$$L_{int,NC} = e \; j_\alpha A^\alpha + g/\cos\Theta_W \left[\; T^3_\alpha - \sin^2\Theta_W \; j_\alpha \; \right] Z^\alpha$$

with $e = g \sin\Theta_W$ and $g'/g = \tan\Theta_W$. So the two gauge couplings are related by the only free parameter of the theory, the Weinberg angle Θ_W .

This perfect SU(2)×U(1) symmetry is spontaneously broken down to U(1)$_{em}$ by a set of weak scalars. That is neccessary in order to give masses to the

three weak gauge bosons W^+, W^-, and Z^0 while the photon remains massless, corresponding to the unbroken $U(1)_{em}$.

In the Weinberg Salam model /5/ (the so called minimal SU(2)×U(1), i.e. the model with the smallest Higgs sector) this is accomplished by introducing a doublet of (complex) Higgs scalars $\Phi = (\Phi^+, \Phi^0)$ which has a non vanishing vacuum expectation value. The complex doublet corresponds to 4 states. Three of them are non physical degrees of freedom, they are needed to give masses and therefore longitudinal polarization states to the W^+, W^-, and Z^0. One remains as a physical particle and should be observable.

In the Standard Model the fermions have the following weak isospin assignments:

$$T_3 = +\tfrac{1}{2}: \quad \begin{pmatrix} \nu_e \\ e \end{pmatrix}_L \begin{pmatrix} \nu_\mu \\ \mu \end{pmatrix}_L \begin{pmatrix} \nu_\tau \\ \tau \end{pmatrix}_L \qquad \begin{pmatrix} u \\ d \end{pmatrix}_L \begin{pmatrix} c \\ s \end{pmatrix}_L \begin{pmatrix} t? \\ b \end{pmatrix}_L$$

$$T_3 = -\tfrac{1}{2}:$$

$$T = T_3 = 0: \quad e_R, \quad \mu_R, \quad \tau_R \qquad u_R, \quad d_R, \quad c_R, \quad s_R, \quad t_R, \quad b_R$$

i.e. the left handed fermions are put into doublets and the right handed ones into singlets. The sequential lepton hypothesis says that the τ and it's neutrino form just another generation of leptons after (e, ν_e) and (μ, ν_μ).

Other possibilities are conceivable, e.g. the ortholepton hypothesis in which the ν_τ is actually identical with the ν_e , ν_μ, or a mixing of both, but all of these are ruled out meanwhile (see " 1.3 Does the τ Have it's Own Neutrino ?" on page 16).

So always one lepton doublet (generation) corresponds to one quark doublet. This symmetry between quarks and leptons is needed in order to make the Weinberg Salam model renormalizable. To cancel out so called Adler anomalies which occur for instance in computing the triangle graph in Figure 1 on page 5, the total charge in one generation of quarks and leptons has to be zero (notice that quarks come in three colors) /10/. However, neither the Standard Model nor theories beyond it as Grand Unification give a clue on why there is more than one generation of particles and they also don't account for the fermion masses, for instance why the τ is $\sim$ 3500 times as massive as the electron.
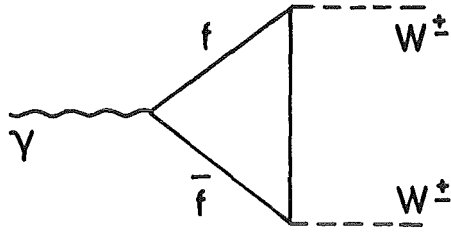
Figure 1.   Triangle graph causing Adler anomalies

1.1   Production

There exist many processes for the production of a heavy sequential lepton. Some of them are shown in Figure 2.
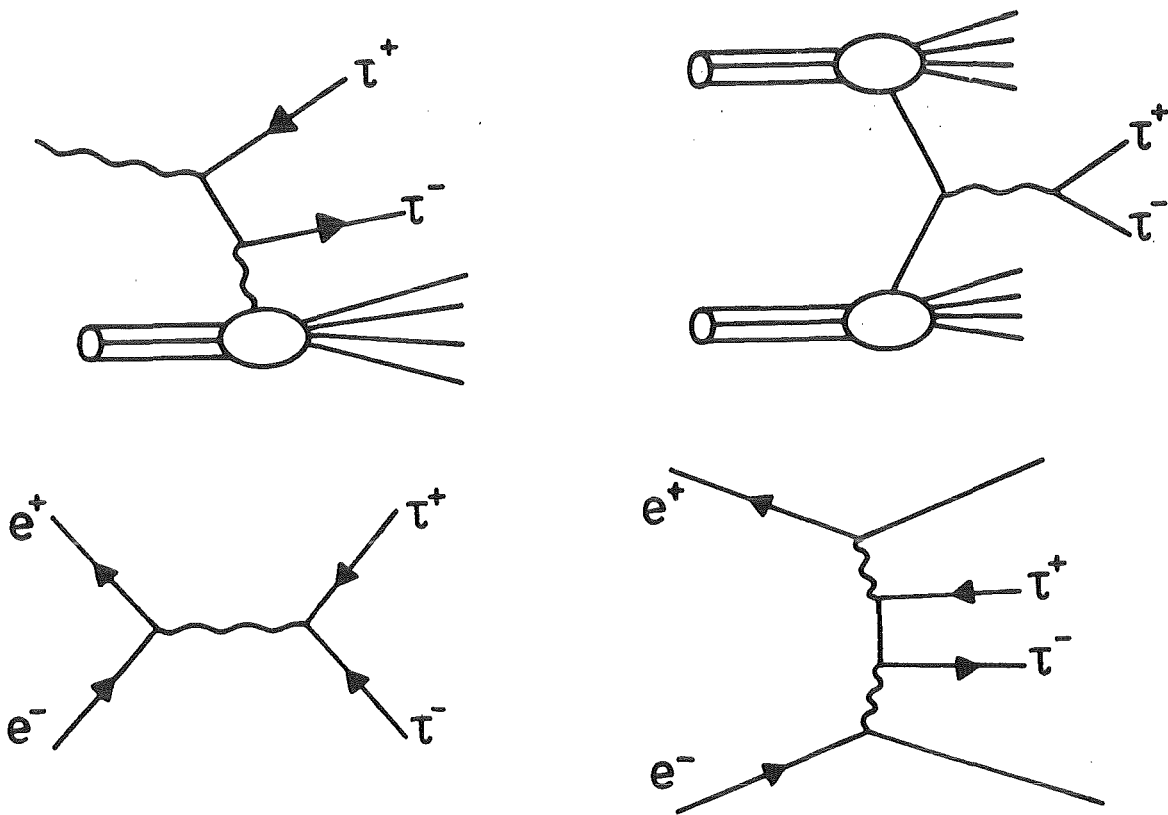
Figure 2.   Some τ production processes:

- photo production
- Drell–Yang process
- $e^+ e^-$ annihilation
- two gamma collision

The best way to produce τ's and to study their properties is pair production in $e^+ e^-$ annihilation:
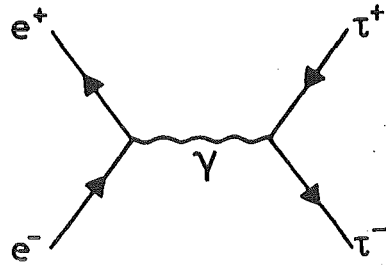
Figure 3. τ pair production via $e^+ e^-$ annihilation

The cross section of this process is (except for a threshold factor $f(\beta)$ due to the higher τ mass) identical with the one of μ pair production, namely in 1st order QED:

$$\sigma_{\tau\tau} = \sigma_{\mu\mu} \frac{3\beta - \beta^3}{2}$$

$$\sigma_{\mu\mu} = \frac{4\pi \, \alpha^2}{3s} = \frac{87 \text{ nb}}{s \text{ (GeV)}}$$

$$s = E_{cm}^2$$

Thus there is a threshold for τ production at twice the τ rest mass, and at higher energies $R_{\tau\tau} = \sigma_{\tau\tau}/\sigma_{\mu\mu}$ rises asymptotically to 1 (Figure 4 on page 8). At c.m. energies of 34 GeV the threshold effect is completely negligible. The differential cross section is (neglecting the threshold factor):

$$\frac{d\sigma}{d\Omega} = \frac{\alpha^2}{8s} \, (1 + \cos^2\Theta)$$

i.e. the typical $(1 + \cos^2\Theta)$ behaviour of pointlike spin 1/2 particles.

This cross section is modified by higher order processes, e.g. initial or final state radiation, or vacuum polarization. See Figure 5 on page 9 for all processes up to order α^3.

The measured cross sections have to be corrected for these radiative effects. For this purpose I used a Monte Carlo program due to Berends and Kleiss /12/, which takes into account initial state radiation, vertex cor-

rections, and hadronic vacuum polarization. Due to the high τ mass final state radiation and box diagrams are negligible for acceptance calculations. They cause however a small positive forward backward asymmetry, which must be taken into account in the angular distribution.

To test the validity of QED even at momentum transfers up to 1200 GeV² one looks for deviations from the QED prediction for the total cross section of the process $e^+e^- \to \tau^+\tau^-$:

$$\sigma = \sigma_{QED} \left(1 + \delta_W + \delta_A\right)$$

Of course the cross sections has to be corrected for radiative effects and vacuum plolarization first. Deviations due to electro weak interference δ_W are small in the Standard Model (see " 2. Using the τ as a Probe for Electro Weak Interference" on page 17) and are neglected here.

Possible sources for a modification of QED could be

• a smeared, non pointlike charge distribution indicating a substructure of leptons or

• the existence of a heavy photonlike object

They modify either vertices or propagators and lead to a modified cross section.
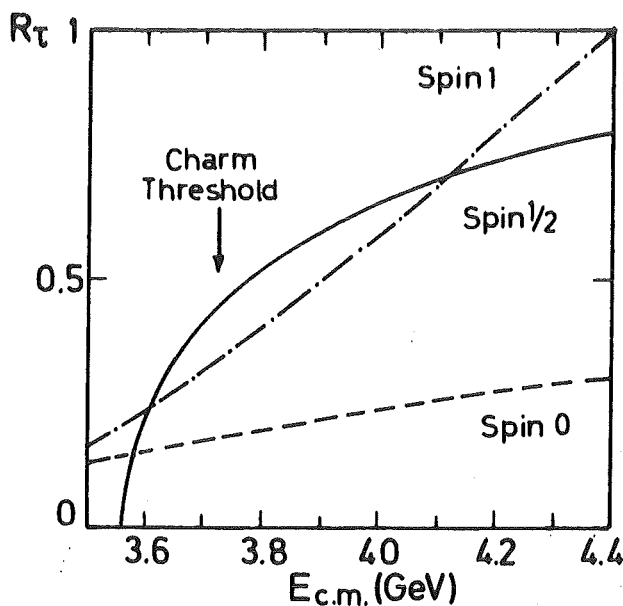
Figure 4. Energy dependence of $R_{\tau\tau} = \sigma_{\tau\tau} / \sigma_{\mu\mu}$
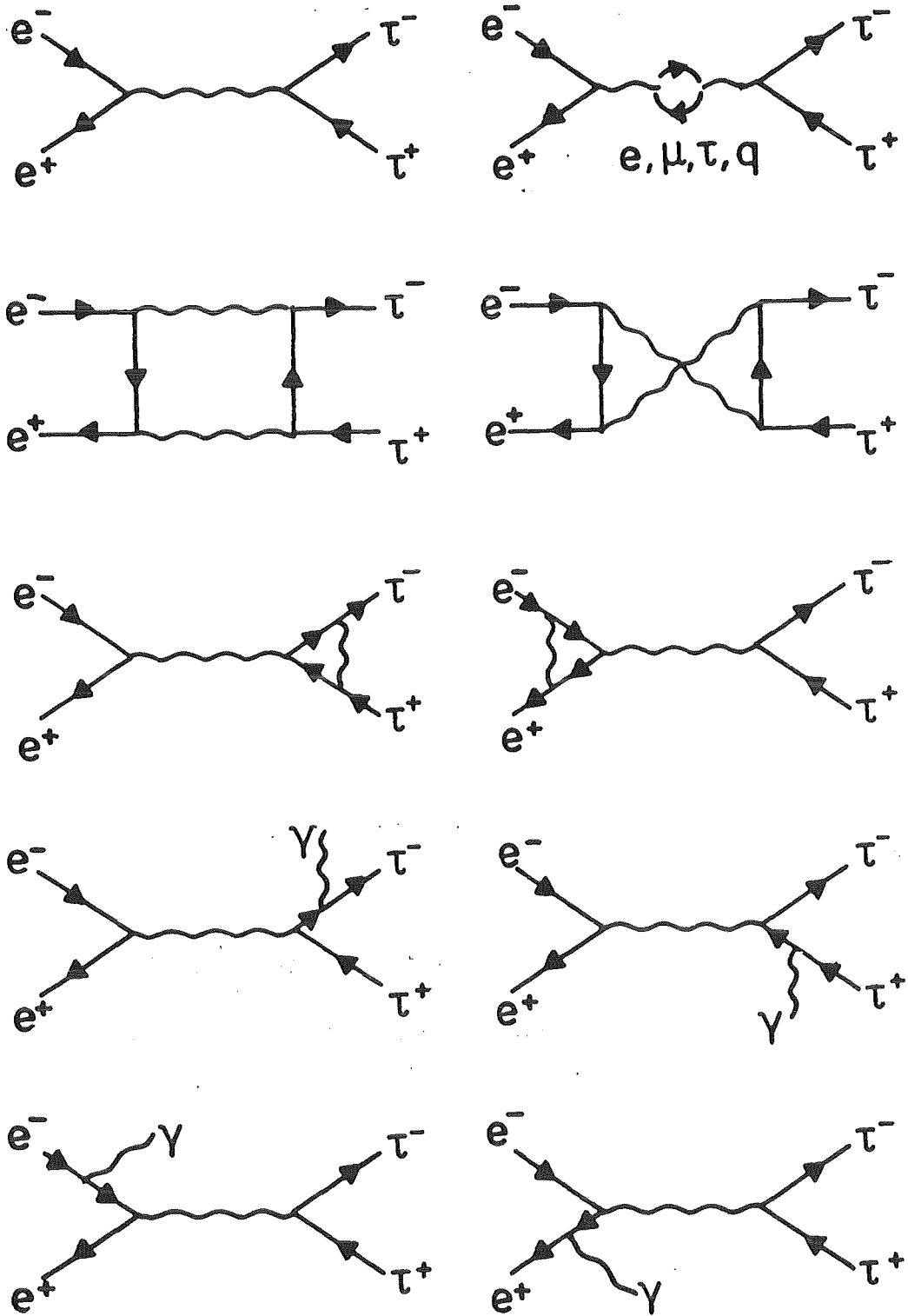
Figure 5. Higher order contributions: Contributions to the process $e^+e^- \to \tau^+\tau^-$ up to order α^3.

Deviations from QED are parametrized by introducing a form factor $F(q^2)$:

$$\sigma = \sigma_{QED} \, |F(q^2)|^2$$

$$F(q^2) = 1 \pm \frac{q^2}{q^2 - \Lambda_{\mp}^2}$$

The so called cutoff parameter Λ can be interpreted as limit on either the charge radius of the τ, or the mass of a new photonlike object.

At higher energies the two photon exchange (Figure 2 on page 6) becomes more and more important. At lower energies this process of the order α^4 is negligible but the cross section has a $\ln^2(E_{beam}/m_e)$ energy dependence, i.e. rises logarithmically with energy, whereas the one photon annihilation rate drops like $1/E^2_{beam}$ (Figure 6).
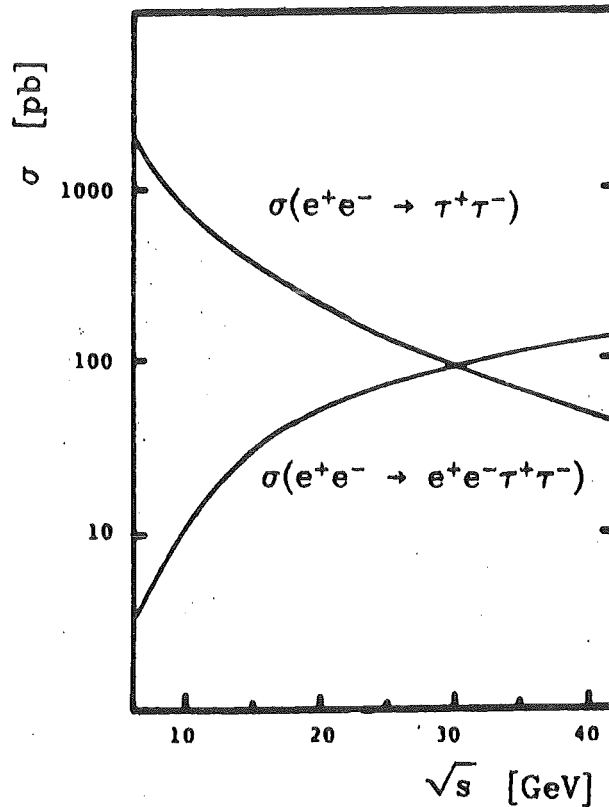
Figure 6.   Cross section of one and two photon τ production

Since we are interested in τ pairs from 1 γ annihilation only, this process represents a source of background. Although the total two photon cross section is larger as the one photon annihilation (Figure 6) it will turn out that this background is small after applying appropriate cuts.

1.2 Decay and Nature of the Weak Coupling

One of the first questions which arose when there were hints that a new heavy lepton was discovered was whether it's decay is mediated by the standard V-A weak current. Under this assumption, plus the sequential lepton hypothesis, very definite predictions on the new lepton can be made. This has been done first by Y.S. Tsai /13/, and by Thacker and Sakurai /14/ in 1971. Here I will discuss the various τ decay channels under these assumptions which were justified by experimental results later.
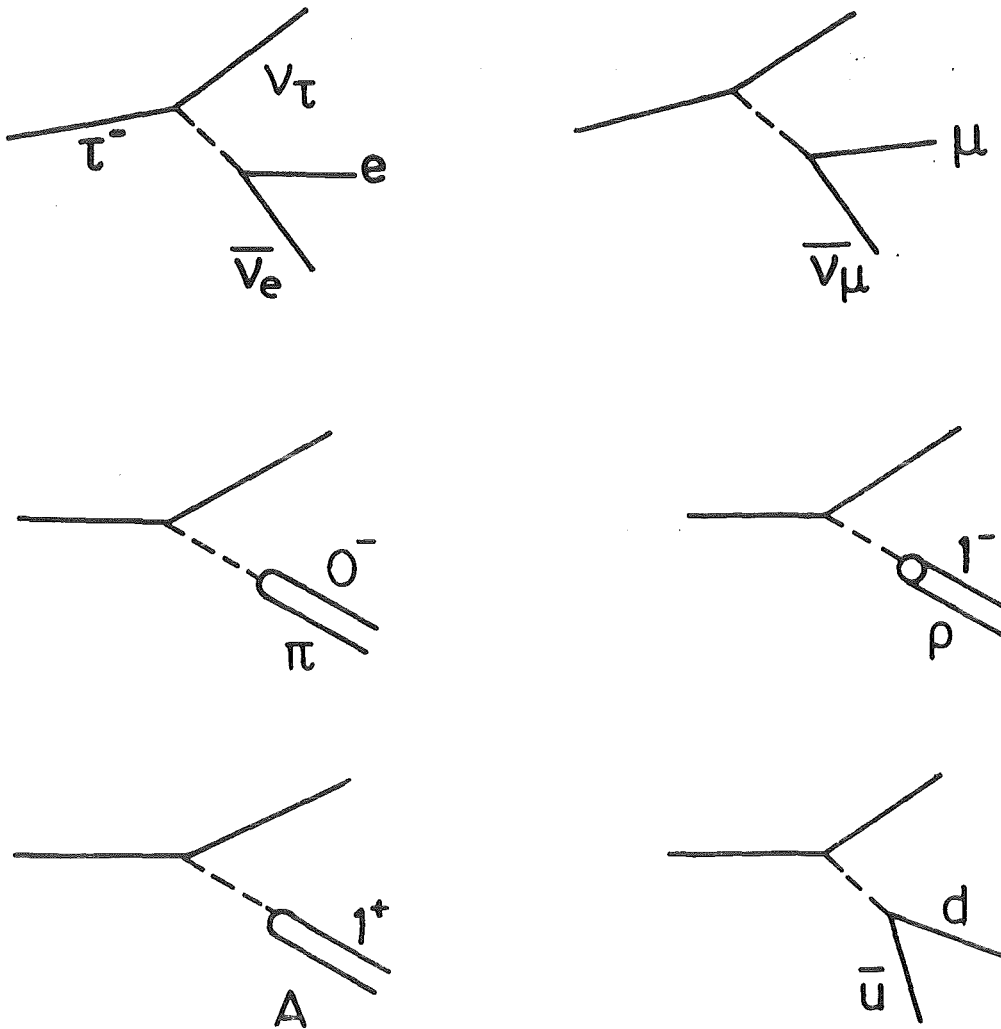
Figure 7.   Decay modes of the τ.   (Cabbibo suppressed channels $\tau \rightarrow K\nu$, $K^*\nu$, $Q_1\nu$, $\bar{u}s$ are not shown)

a.) The Purely Leptonic Channels

The purely leptonic decay rates can be predicted unambigiously by our knowledge on the decay $\mu \rightarrow e\nu\nu$:

$$\Gamma(\tau \rightarrow e\nu\nu) = \Gamma(\mu \rightarrow e\nu\nu) \left(\frac{m_\tau}{m_\mu}\right)^5$$

$$= \frac{G^2 \, m^5_\tau}{192 \, \pi^3}$$

The mass of the electron has been neglected here.

Correspondingly, for the decay into a muon

$$\Gamma(\tau \rightarrow \mu\nu\nu) = \frac{G^2 \, m^5_\tau}{192 \, \pi^3} \cdot f, \qquad f = .972$$

where f is a small phase space correction factor, taking into account the μ mass.

b.) The Semi Hadronic Decay Modes

Since the τ is much more massive than the π it can decay semi hadronically. A quick estimate of the hadronic branching fraction can be obtained by just counting the number of quarks and leptons that are energetically accessible in the τ decay: two generations of leptons, and one generation of quarks (u,d). Since quarks come in 3 coulors, one would expect naively $B_e \sim B_\mu \sim 20 \%$ and $B_{semihad.} \sim 60 \%$ which agrees pretty well with more detailed calculations.

Since the charged weak current has both, a vector and an axial vector component, there are three different kinds of currents which can contribute to the hadronic final state in the τ decay:

| V coupling, | $J^P = 1^-$ | $\rightarrow$ decay in ρ |
| A coupling, | $J^P = 1^+, \, 0^-$ | $\rightarrow$ decay in A_1, π |

Due to CVC no 0^+ final states appear.

CVC and $e^+e^- \to \rho^0$ data can be used to calculate the decay rate $\Gamma(\tau \to \rho\nu)$:
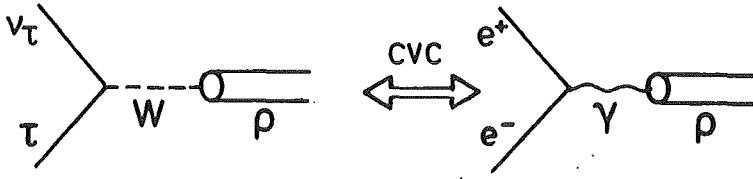
The rate $\Gamma(\tau \to \pi\nu)$ can be predicted using our knowledge on the π decay. From this we know the π-W coupling f_π .
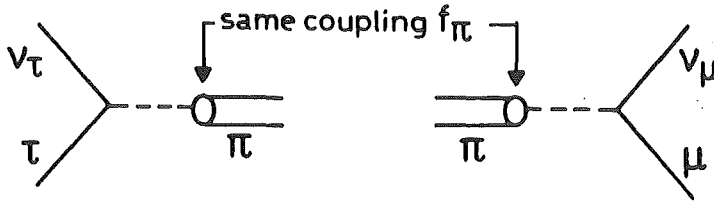
To calculate the rate for the axial vector decay $\tau \to A_1\nu$ one needs further assumptions on the relative strength of the vector and axial vector couplings (Weinberg sum rules).

Beside the resonant decay modes (and their Cabbibo suppressed counterparts) there are also non resonant decays $\tau \to \nu + n\pi$. Little is known about these. There exist calculations which use CVC and $e^+e^- \to$ hadrons data to predict rates for the non resonant decay in an even number of pions /15/, and Pham, Roiesnel, and Truong /16/ used PCAC and current algebra to predict the rates for the decay into an odd number of π's.

The various τ decay channels, their measured and predicted branching fractions, experimental references, etc. are summarized in Figure 8 on page 14.

	decay channel	J^P	best exp. BR	theor. BR	theor. input
purely leptonic decay modes				
1	$\tau \to e\nu\nu$		17.0 ± 1.1 /17.1/	17.6	e-μ-τ universality
2	$\tau \to \mu\nu\nu$		17.9 ± 1.5 /17.1/	17.2	
semihadronic decays, Cabbibo allowed				
3	$\tau \to \rho\,\nu$	1^-	21.6 ± 3.7 /17.2/	22.5	CVC + exp. data $e^+e^- \to \rho$
4	$\tau \to \pi\,\nu$	0^+	10.7 ± 1.6 /17.1/	10.5	f_π from $\pi \to \mu\nu$
5	$\tau \to A_1\nu$	1^+		8.7	Weinberg sum rules
6	$\tau \to ud\,\nu$				CVC or PCAC + exp. data $e^+e^- \to$ hadrons
semihadronic decays, Cabbibo suppressed				
7	$\tau \to K^*\nu$	1^-	1.7 ± 0.7 /17.6/	1.5	as 3 + tan θ_c
8	$\tau \to K\,\nu$	0^+	1.2 ± .45 /17.3/	.7	as 4 + tan θ_c and K $\to \mu\nu$
9	$\tau \to Q\,\nu$	1^+			as 5 + tan θ_c
10	$\tau \to us\,\nu$				as 6 + tan θ_c

Figure 8. τ decay mode summary

c.) The V, A Structure of the τ-ν Coupling

The best determination of the τ-ν_τ coupling has been derived by DELCO from the shape of the electron spectrum /18/ (see Figure 9). The spectrum can be represented by

$$\frac{dN}{dx} = x^2 \left[\; 9(1 - x) + 2\rho(4x - 3) \; \right]$$

where $x = E_e/E_{max}$ stands for the scaled electron energy in the τ rest frame and ρ is the so called Michel parameter:

pure V, A $\rho = .375$
pure V-A $\rho = .75$
pure V+A $\rho = 0$

A fit to the spectrum yields $\rho = .72 \pm .15$ in good agreement with V-A, strongly disfavouring pure V or A, and excluding a large contribution of V+A. A small right handed admixture, however, is still possible.

$$z = E_e/E_e^{max}$$
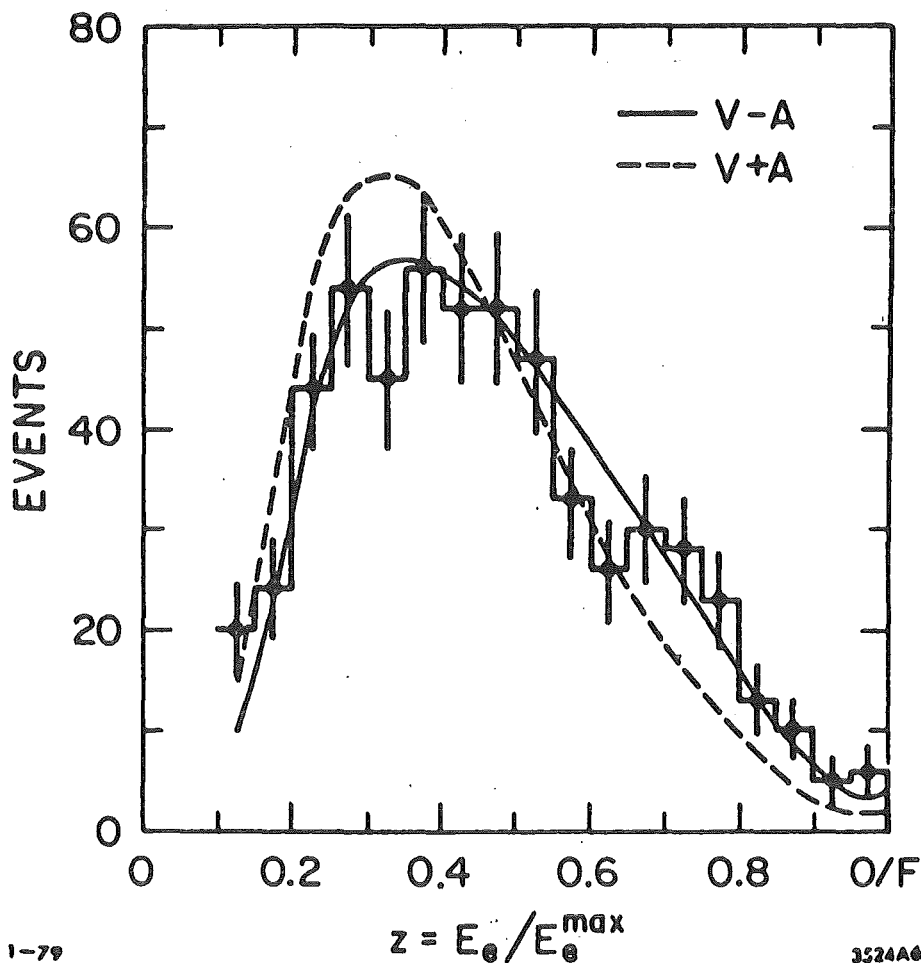
Figure 9.   Lab. momentum of electrons from τ decays (DELCO)

1.3   Does the τ Have it's Own Neutrino ?

First of all it can be shown that the τ must have it's own lepton number. Let's assume assume the τ^- has the same lepton number as the e^-. Then the τ would decay with almost 100 % into e^- via $\tau^- \to e^- \gamma$. If $L(\tau^-)$ were equal to $L(e^+)$ then the ν_τ would be identical to the $\bar\nu_e$ and the decay $\tau^- \to e^- \bar\nu_e \bar\nu_e$ would, for statistical reasons, happen twice as often as the decay $\tau^- \to \mu^- \bar\nu_\mu \bar\nu_e$. The same arguments apply for $L(\tau^-) = L(\mu^+)$ and $l(\tau^-) = L(\mu^-)$. Both possibilities are contradicted by experiment.

The new life time measurements /19/ show that the τ couples with conventional strength to the weak charged current. Using this information, it can be shown in a model independent way that the ν_τ exists. I will repeat here an argument given by G.J. Feldman /6/.

From the momentum spectrum of the τ decay products we know that there must be a light unobserved spin 1/2 particle. Let's assume the ν_τ doesn't exist. Then this particle be must either the ν_e or the ν_μ or a linear combination of these like $\nu' = \varepsilon_e \nu_e + \varepsilon_\mu \nu_\mu$. ε_μ and ε_e are defined such that for normal strength τ-ν' coupling we have $\varepsilon^2_e + \varepsilon^2_\mu = 1$. The Mark II life time measurement for instance gives us the 90 % C.L. limit

$$\varepsilon^2_e + \varepsilon^2_\mu > .75 \qquad\qquad (1)$$

From the absence of excess electrons in $\nu_\mu N$ interactions we obtain /20/

$$\varepsilon^2_\mu < .025 \qquad\qquad (2)$$

and from the absence of apparent excess neutral current events in the BEBC beam dump experiment /21/ we derive

$$\varepsilon^2_e < .35. \qquad\qquad (3)$$

Combining   (2) and (3) one obtains

$$\varepsilon^2_e + \varepsilon^2_\mu < .375 \qquad\qquad (4)$$

in contradiction with (1). Thus there must be an additional neutrino, the ν_τ.

2. USING THE τ AS A PROBE FOR ELECTRO WEAK INTERFERENCE

The process $e^+e^- \to \tau^+\tau^-$ offers the possibility to measure the coupling of the τ to the weak neutral current via electro weak interference and thus to test the Standard Model of electro weak interaction.

The neutral current interaction Lagrangian can be written as

$$L_{int,NC} = g/\cos\Theta_W \ J_\alpha^{NC} Z^\alpha$$

with

$$J_\alpha^{NC} = \sum_i \bar{f}_i \ \gamma_\alpha \ \tfrac{1}{2}(\ v_{f,i} - a_{f,i} \ \gamma_5) \ f_i$$

The Standard Model predicts for the fermion's vector and axial vector couplings v and a

$$v_f = 2 \ (T_3 - 2 \ Q_f \ \sin^2\Theta_W)$$
$$a_f = 2 \ T_3$$

The task of the experimentalist is to measure these coupling constants for both the charged leptons and the quarks as accurately as possible.

Various processes have been used to shed light on the structure of the neutral current(s), like neutrino hadron and electron deuteron reactions which yield the most accurate values for the Weinberg angle. Of particular interest are purely leptonic processes because here no uncertainties about nucleon structure functions and QCD corrections enter. Here we have two classes of reactions, namely neutrino electron scattering and electroweak interference in $e^+e^- \to$ leptons. The combined ν_μ e, $\bar{\nu}_\mu$ e, and $\bar{\nu}_e$ e scattering data yield the most accurate measurements of the lepton neutral current couplings, but they leave an ambiguity between a vector dominant solution and the axial vector dominant solution predicted by the Standard Model (see Figure 10 on page 18). This ambiguity can be resolved by $e^+e^- \to 1 \ \bar{1}$ data. Another point of interest about $e^+e^- \to$ leptons is that it extends the tests of the Standard Model into a completely new Q^2 regime where Z^0 propagator effects may become observable[1] .

---

[1]   The expected charge asymmetry at 34 GeV is -7.8 % for infinite Z^0 mass and -9.3 % including the Z^0 propagator. But already at 44 GeV, the energy planned for PETRA in summer 1983, the figures are -13 % and -17 % respectively.

But already at current PETRA energies far below the Z^0 mass interference between $e^+e^- \to \gamma \to f\bar{f}$ and $e^+e^- \to Z^0 \to f\bar{f}$ can be observed:

$$\sigma \propto \left| \begin{array}{c} e^+ \\ e^- \end{array} \gamma \begin{array}{c} \tau^+ \\ \tau^- \end{array} + \begin{array}{c} e^+ \\ e^- \end{array} Z^\circ \begin{array}{c} \tau^+ \\ \tau^- \end{array} \right|^2$$

$$\sigma \propto |A_{QED} + A_W|^2 = A^2_{QED} + 2A_{QED}A_W + A^2_W$$
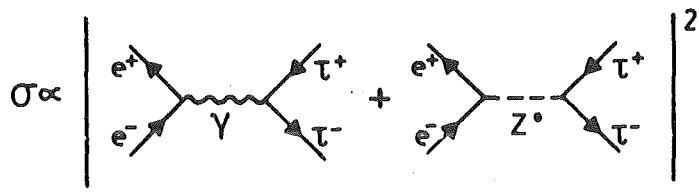
For $e^+e^- \to q\bar{q}$ it is hard to disentangle the contributions from the different quark flavours so that until now only the purely leptonic processes $e^+e^- \to \mu^+\mu^-$, $\tau^+\tau^-$, and e^+e^- (where also spacelike diagrams contribute) have been considered. (except for the total hadronic cross section, which energy
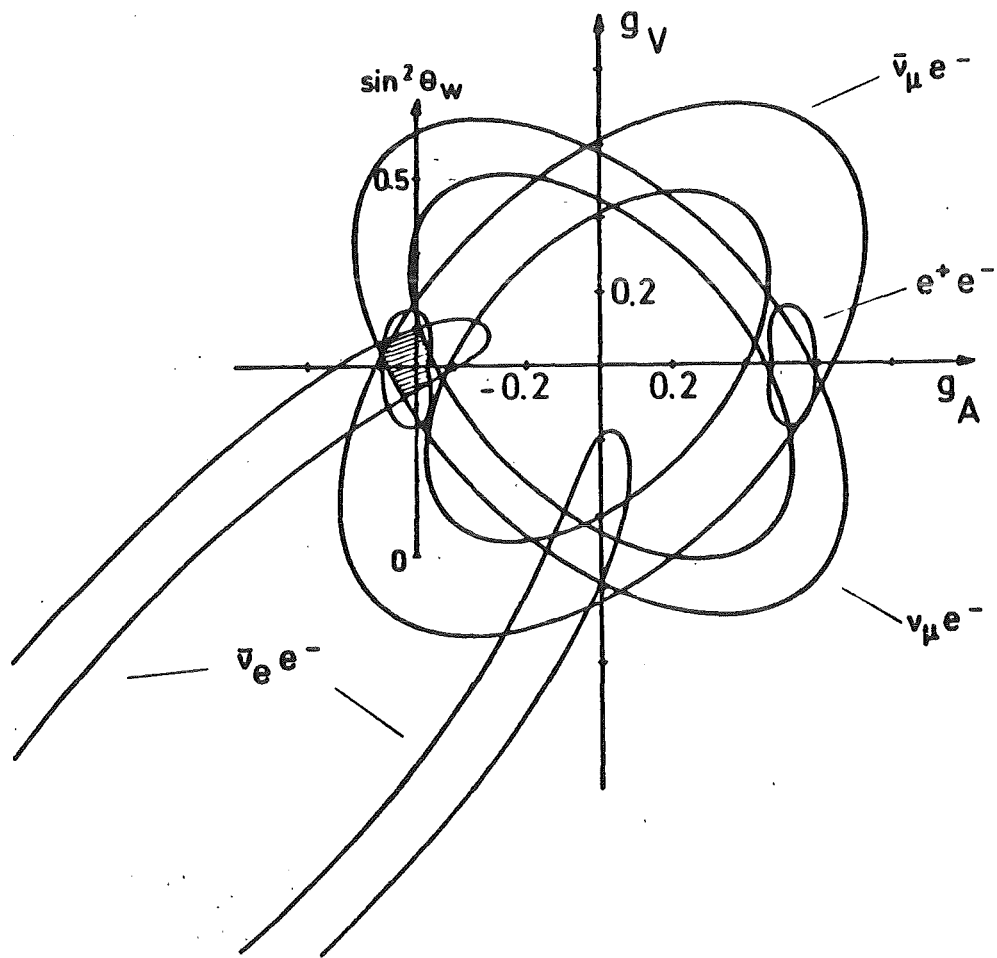
Figure 10.   Limits on v, a couplings of electrons from ν e data

dependence allows to measure $\sin^2\Theta_W$, provided that the QCD correction are really understood /22/)

Here I will consider only the process $e^+e^- \to \tau^+\tau^-$ (all said here applies for $e^+e^- \to \mu^+\mu^-$ just as well). The most general low energy ($Q^2 \ll M_Z^2$) effective Lagrangian for $e^+e^- \to Z^0 \to \tau^+\tau^-$ involving V, A currents can be written in a most model independent notation introduced by Sakurai /23/ as

$$L = -\frac{G}{\sqrt{2}} \left\{ \; h_{VV} \, (\bar{e}\gamma_\alpha e + \bar{\tau}\gamma_\alpha\tau)(\bar{e}\gamma^\alpha e + \bar{\tau}\gamma^\alpha\tau) \right.$$

$$+ \; 2 \; h_{VA} \, (\bar{e}\gamma_\alpha e + \bar{\tau}\gamma_\alpha\tau)(\bar{e}\gamma^\alpha\gamma_5 e + \bar{\tau}\gamma^\alpha\gamma_5\tau)$$

$$\left. + \; 2 \; h_{AA} \, (\bar{e}\gamma_\alpha\gamma_5 e + \bar{\tau}\gamma_\alpha\gamma_5\tau)(\bar{e}\gamma^\alpha\gamma_5 e + \bar{\tau}\gamma^\alpha\gamma_5\tau) \right\}$$

For all models involving a single Z boson one has the following factorization relations:

$$h_{VV} = 1/4 \; v^2 / \rho$$
$$h_{VA} = 1/4 \; av / \rho$$
$$h_{AA} = 1/4 \; a^2 / \rho$$

In the Standard Model, as in all models with the Higgses in doublets, one has $\rho = 1$.

Summing over the spin orientations of one of the τ's, the differential cross section can be written as

$$\left(\frac{d\sigma}{d\Omega}\right)_{h_-} = \frac{\alpha^2}{8s} \left\{ (1 + \cos^2\Theta)(1 + 2X \, v_e v_\tau) + 4X \, a_e a_\tau \cos\Theta \right.$$

$$\left. + \; h_- 2X \, [(1 + \cos^2\Theta) \, v_e a_\tau + 2\cos\Theta \, a_e v_\tau] \right\}$$

with

h_-:   helicity of τ^-

$X = gM_Z^2 \, s/(s - M_Z^2)$, $g = G_F/8\pi\alpha\sqrt{2} = 4.49 \cdot 10^{-5} \; GeV^{-2}$
$X(34 \; GeV) \sim -.06$

The purely weak terms proportional to X^2 have been neglected. They are still very small at current energies, so only the terms $\propto X$ (the interference terms) can be observed. It is apparent that the total cross section measures v^2, while the term linear in $\cos\Theta$ introduces a forward backward asymmetry in the angular distribution proportional to a^2.

The Standard Model predicts for charged leptons

$$v = -1 + 4 \sin^2\Theta_W \qquad \sim .08 \text{ for } \sin^2\Theta_W = .23$$
$$a = -1$$

Since $\sin^2\Theta_W$ happens to be close to $1/4$, v^2 becomes vanishingly small for leptons so that the only observable effect expexted is an asymmetry in the polar angular distribution:

$$A = \frac{N_F - N_B}{N_F + N_B} = \frac{3}{4}\frac{F_3}{F_1} \sim -\frac{3}{2} a^2 X = -9.3 \% \text{ at } 34 \text{ GeV}$$

The third, helicity dependent, term in the differential cross section gives rise to a parity violating polarization of the outgoing leptons:

$$P_-(\cos\Theta) = 2X \left(v_e a_\tau + \frac{2\cos\Theta}{(1+\cos^2\Theta)} a_e v_\tau \right), \qquad <P_>> = - <P_->$$

The weak decay of the τ can be used as an analyzer for this polarization /13/. Particularily useful are the two body decay modes $\tau \to \pi\nu$ and $\tau \to \rho\nu$:
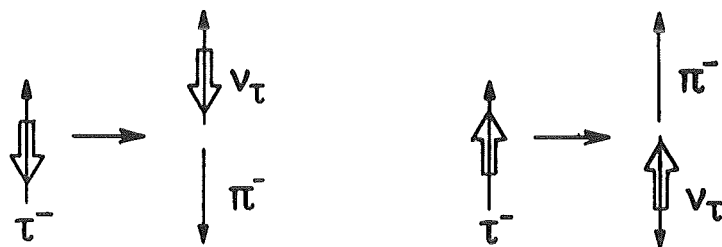
Figure 11. Decay of a left (right) handed τ^-

Let's assume the τ^- comes out left handed (see Figure 11). Then, due to angular momentum conservation, the left handed ν_τ has to be emitted preferably in forward direction, and thus the π^- in backward direction. The result is a softening of the normally box shaped π lab. momentum spectrum /24/ (see Figure 13 on page 21):

$$\frac{dN}{dx_\pm} \propto 1 \pm P_\pm \alpha \frac{x_\pm - 1/2}{1/2}, \qquad \alpha = 1 \text{ for } \pi, .46 \text{ for } \rho$$

were x is the momentum scaled to the kinematically accessible range.

The same is true for the decay $\tau \to \rho\nu$, though the effect is only about the size due to its vector structure (see Figure 12). But because of it's large branching fraction this channel is equally important.

$$W(\Theta) = 1 + \alpha \cos \Theta$$

$$\alpha(\pi) = 1$$

$$\alpha(\rho) = \frac{m_\tau^2 - m_\rho^2}{m_\tau^2 + m_\rho^2} \sim 0.46$$
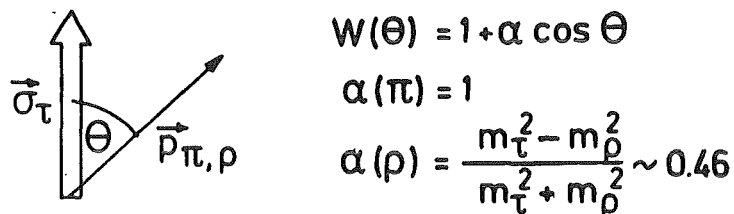
Figure 12. π (ρ) angular distribution in the τ rest frame
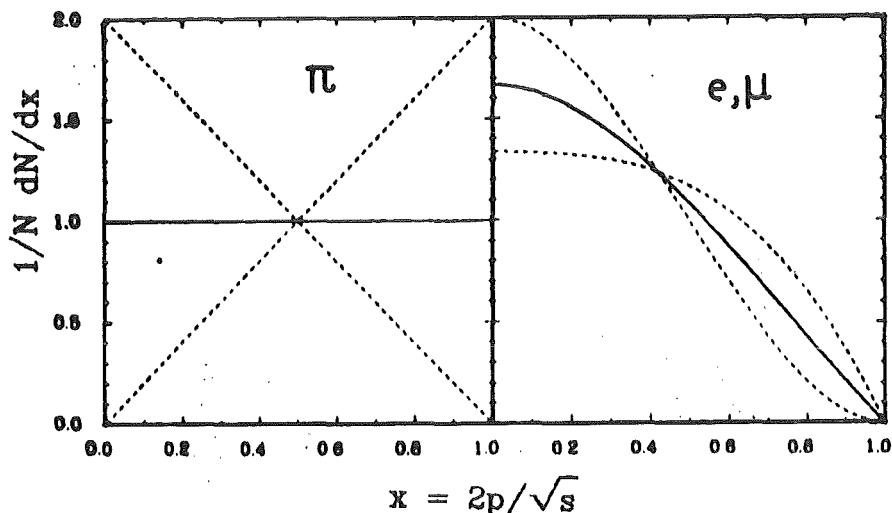
Figure 13.   Pion and lepton inclusive spectra,
solid line: no polarization
broken line: $\pm$ 100 % polarization

The inclusive lepton spectra also contain information on a possible τ polarization, though the effect is smeared out by the three body decay $\tau \to l\nu\nu$. The lepton lab. momentum distribution from τ decays in flight has the form /25/

$$\frac{dN}{dx_\pm} \propto a(x_\pm) \pm P_\pm\, b(x_\pm) \qquad \text{with}$$

$$a(x) = 1/3\ (5 - 9x^2 + 4x^3) \qquad \text{and}$$

$$b(x) = 1/3\ (1 - 9x^2 + 8x^3)$$

Looking at the expression for $P_-(\cos\Theta)$ one finds two terms: a polar angle independent term $\propto v_e a_\tau$ and a term $\propto a_e v_\tau$ dependent on $\cos\Theta$. Both a_τ and v_e in the first term as well as a_e have been measured in $\tau^+\tau^-$ charge asymmetry, and νe and Bhabha scattering respectively. Thus by measuring the angular dependence of τ polarization one gets, for the first time, a handle on the neutral current vector coupling v_τ of the τ lepton providing a check on universality[2] .

On the other hand, one can assume universality, i.e. $a_\tau = a_e$ and $v_\tau = v_e$, and obtain limits on h_{VA} and thus check factorization ($h_{VA} = 1/4\ a\cdot v/\rho$, $\rho = 1$ for all models with Higgses in doublets).

One should note, however, that in this measurement one has the same problem as in measuring v^2: Since v happens to be small in the Standard Model prediction, the expected polarization is very small, namely $<P> = 2$ av $X \sim 1\ \%$ at current energies.

---

[2]   Note that the interference term in the total cross section $\propto v_e v_\tau$ gives no constraint on v_τ since v_e experimentally is compatible with zero.

III. EXPERIMENTAL SETUP

Data was taken using the CELLO detector at the PETRA (Positron Electron Tandem Ring Accelerator) electron positron storage ring at DESY (Deutsches Elektronen SYnchroton) in Hamburg.

1. PETRA

The physics programme of the two high energy e^+e^- storage rings SPEAR and DORIS has been overwhelmingly succesful. Two new quark flavours were discovered and studied in detail, a new heavy lepton was found, the existence of jets was proved, to name only some of the exciting findings which changed our picture of particle physics dramatically.

Therefore people soon started to think about a new very high energy e^+e^- machine in the 30 .. 40 GeV range. The main motivations were the search for new particles, in particular the sixth quark flavour or new heavy leptons, the study of electro weak interference effects predicted by models of electroweak interaction, the investigation of quark and, perhaps, gluon jets, and tests of the dynamics of QCD, a strong candidate for a theory of strong interaction, and, of course the search for the unexpected. The electron positron storage ring PETRA has been built in the years 1976 to 1978. It has been designed for a peak c.m. energy around 40 to 50 GeV with luminosities in the order of 10^{31} $cm^{-2}s^{-1}$.

The general layout can bee seen in Figure 15 on page 25. Electrons are initially accelerated in LINAC I and then injected into the DESY synchroton where they are accelerated up to the PETRA injection energy of 7 GeV and then shot into PETRA. Positrons are created in LINAC II and are accumulated in PIA (Positron Intensity Accumulator). Then like electrons they are injected via DESY into PETRA. When electron and positron injection is complete the bunches are accelerated from injection energy to the desired beam energy. Some important machine parameters are summarized in Figure 14 on page 24.

In February 1981 the luminosity was improved by installing additional 'mini beta' quadrupoles close to the interaction points to increase the beam focussing. The peak luminosity was increased to $\sim 1.5 \cdot 10^{31}$ $cm^{-2}s^{-1}$. Figure 16 on page 26 shows the PETRA performance in the period March til May 1981 when the data used in this analysis was taken.

A polarization of one or both of the beams would be very helpful in studying electro weak effects. This would be particularily true for longitudinal

polarized beams since right- and left handed electrons are quite different particles with respect to weak interaction.

In e^+e^- storage rings a transverse polarization builds up spontaneously, though there are many effects which tend to destroy this polarization as for instance depolarizing resonances, beam beam interaction or the influence of the experiment solenoids.

Nevertheless, a transverse polarization of up to 80 % has been observed in colliding beam operation with luminosities of $3 \cdot 10^{30}$ cm^{-2}s^{-1}, though with the experiment magnets switched off/26/.

Experimentally, a transverse beam polarization would show up by introducing a structure in the normally flat distribution of the azimuthal angle

Measures		
Circumference		2304 m
Radius of curvature		192 m
Length of accelerating sections		108 m
Length of experimental zones		15 m
Injection energy		7 GeV
Beam energy		5-19 GeV
Energy loss of particles at 18.3 GeV		58 MeV/turn
Energy spread		0.023 E(r.m.s) MeV
Luminosity (at 15 GEV)		max $3 \cdot 10^{30}$ cm^{-2} sec^{-1}
with MINI-BETA (since 1981)		max $15 \cdot 10^{30}$ cm^{-2} sec^{-1}
Beam life time		3-5 hours
Number of bunches		2 e^+ + 2 e^-
Bunch length		10 mm r.m.s
Beam currents	currently	max 20 mA
	design	80 mA
RF frequency		500 MHz
RF power		4 MW
Number of clystrons		8
Number of resonators	(Feb 1981)	60

Figure 14. PETRA machine parameters

Φ of 1 photon final states /27/. From the Φ distribution of $e^+e^- \to \gamma\gamma$ and $e^+e^- \to \tau^+\tau^-$ final states find for the transverse polarization under data taking conditions $P^+P^- = .03 \pm .09$.
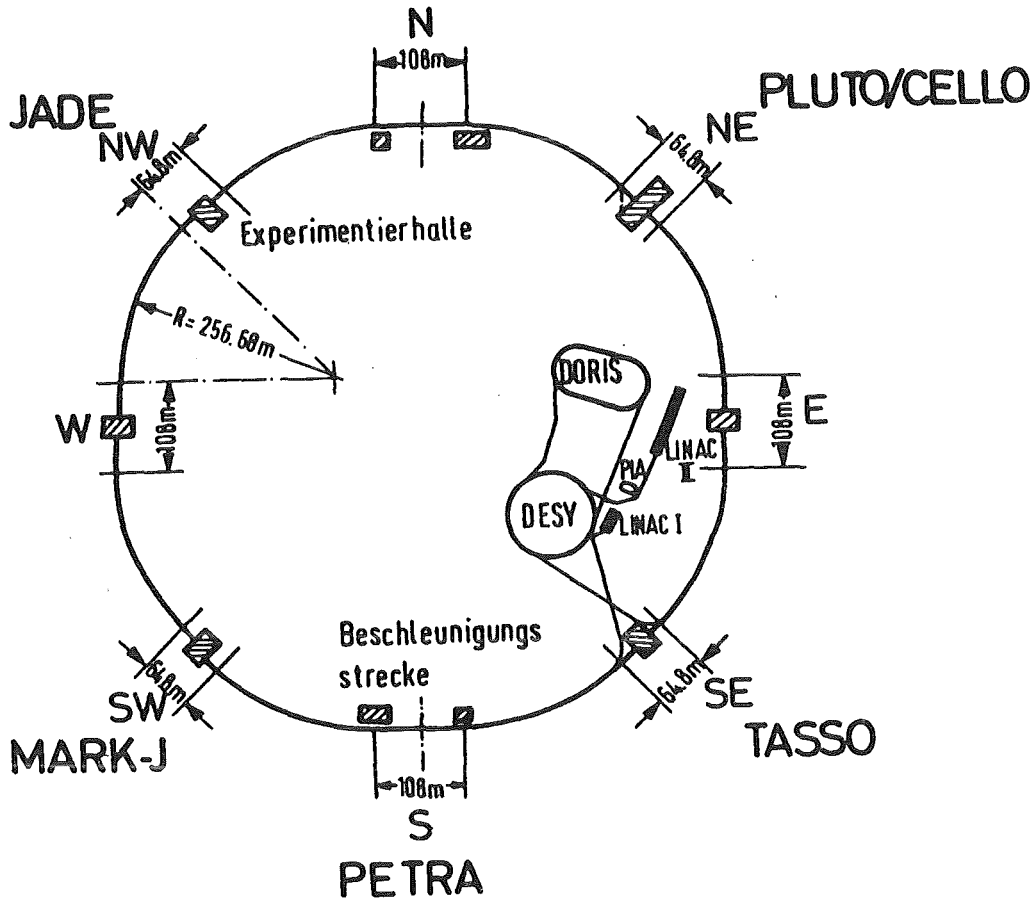
Figure 15.   Accelerators on the DESY site
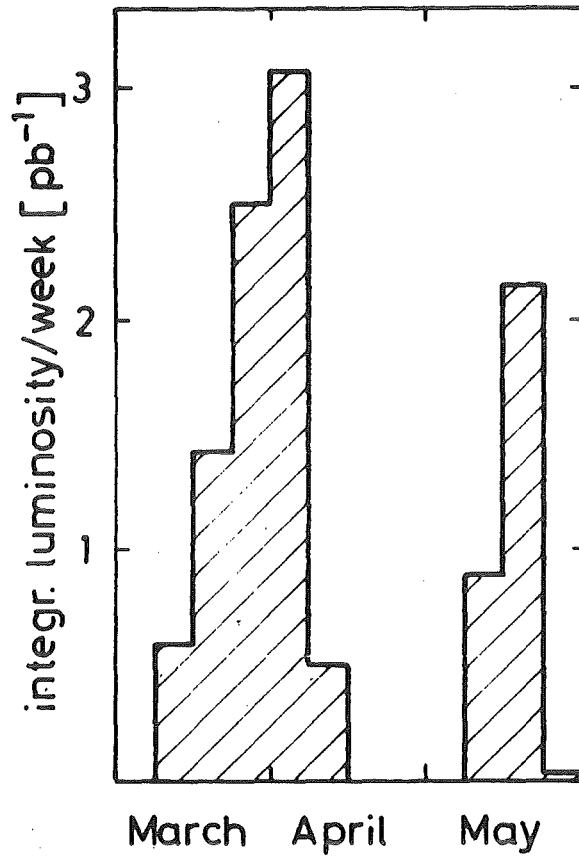
Figure 16. PETRA machine performance in terms of luminosity delivered per week in the period from March til May 1981 after istallation of the 'mini beta' quadrupoles.

2. THE CELLO DETECTOR

The CELLO detector is built and operated by a French-German collaboration /28/. CELLO is a general purpose 4π magnetic detector at the PETRA storage ring. It has been optimized for a good lepton-hadron separation and photon identification over almost the entire solid angle.

Its main components are (see Figure 17 on page 28)

- a magnetic inner detector for measuring the momentum of charged particles surrounding a beam pipe of .05 radiation lengths. It consists of 7 cylindrical drift chambers and 5 cylindrical prop. chambers surrounded by a thin (.5 X_0) superconducting solenoid producing an homogeneous magnetic field of 1.3 T.

  In addition there are endcap proportional chambers in front of the liquid argon end cap modules covering the forward region between 153 and 428 mrad.

- a finely segmented lead liquid argon calorimeter, 20 X_0 thick, for a good identification of electrons and photons, and electron-hadron separation. It consists of two parts, the barrel and two end cap modules, covering 96 % of the solid angle.

- Behind an hadron absorber of 5 .. 8 absorption length iron there is a system of 32 muon chambers covering 92 % of 4π.

- a flexible and powerful trigger system, consisting of a charged particle trigger, requiring only two tracks with p_T > 200 MeV, a neutral trigger from the liquid argon counters, and combinations of these.

I will restrict myself on a more detailed description of those components relevant for this analysis. A more complete description of the detector can be found elsewhere /29/.

Figure 17. The CELLO detector
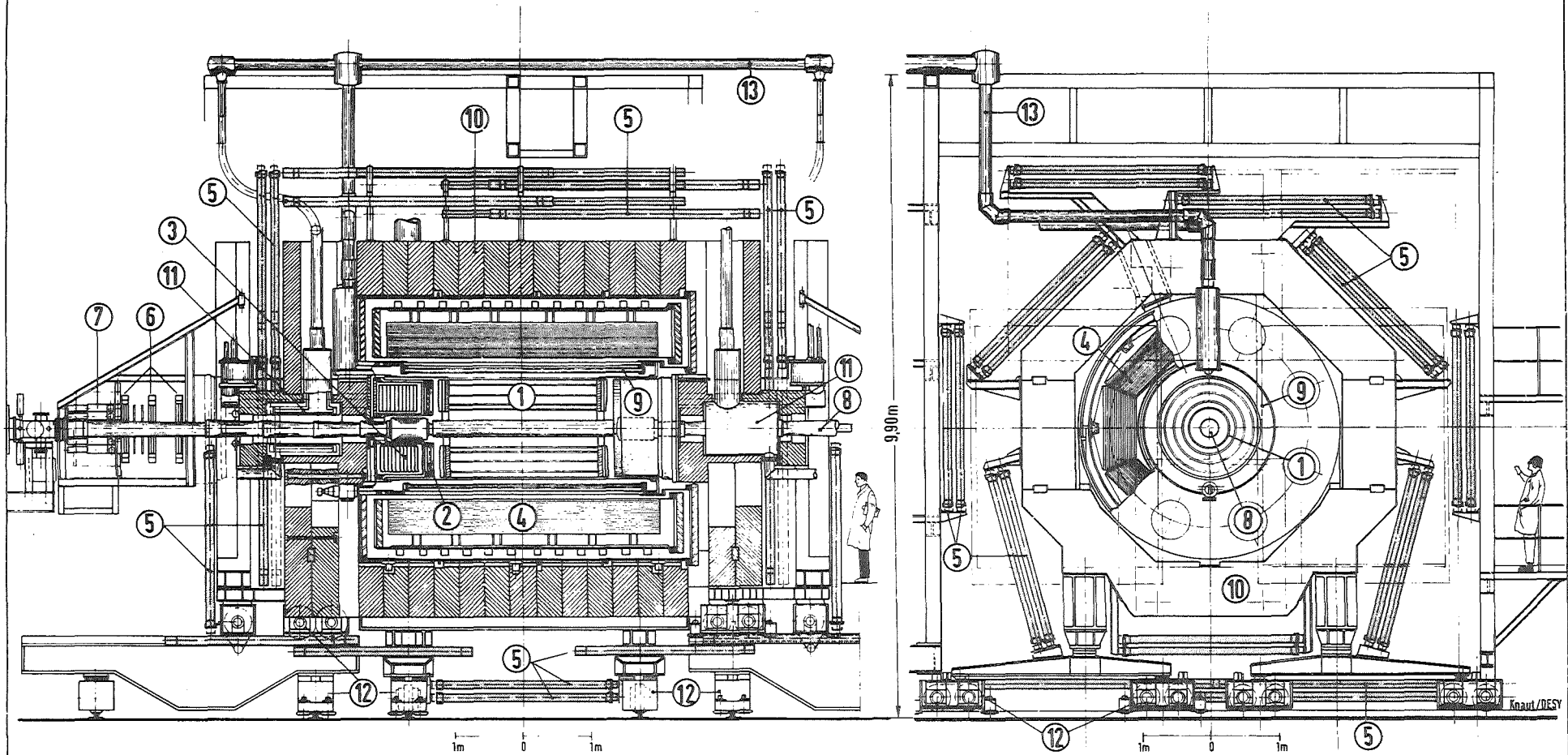
1 Central Drift-and Proportional Chambers
2 Endcap Proportional Chambers
3 Endcap Shower Counters (liquid Argon)
4 Cylindric Shower Counters (liquid Argon)
5 Proportional Chambers for Muon Detection
6 Drift Chambers for Forward Detector
7 Shower Counter for Forward Detector

8 Vacuum Beam Pipe
9 Superconducting Coil of Detector
10 Iron Yoke
11 Compensation Coils
12 Moving Devices
13 Feed Lines for Liquid Helium

Participants:
Orsay
Saclay
University (VI) of Paris
MPI, München
GfK, Karlsruhe
DESY, Hamburg

DETECTOR CELLO

Total Weight: ~1400 t
Magnet Field: 15 kΓ

2.1   Inner Detector

Charged particle tracking is done by a combination of interleaved cylindrical drift and proportional chambers (see Figure 18). They cover the polar range |cos Θ| < .87.
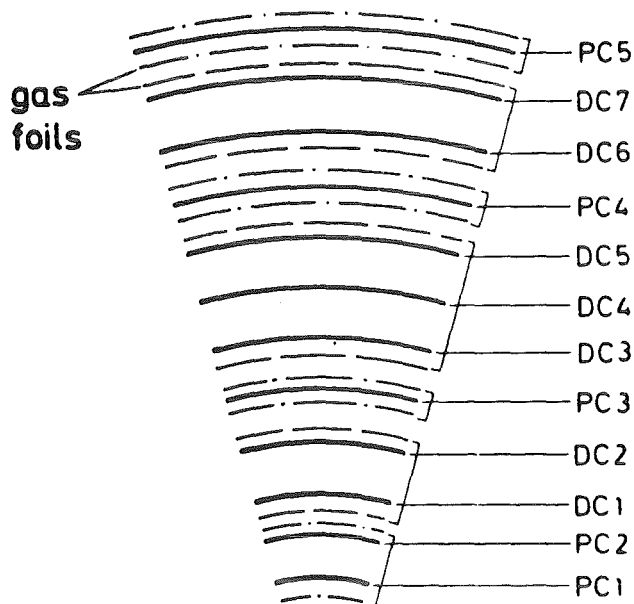
Figure 18.   Schematic cross section of the CELLO inner detector

a.) THE DRIFT CHAMBERS are used for an accurate measurement of track coordinates in the $r\phi$ plane perpendicular to the beam axis. The track curvature in this plane measures the track momentum so that a good resolution in $r\phi$ is essential for momentum measurement. The spatial resolution of the drift chambers was ~ 330 μm. Note that this value is averaged over all chambers and has been determined from Bhabha events taken over a long running period. Figure 20 on page 30 shows the residuals for Bhabha events.

b.) THE CYLINDRICAL PROPORTIONAL CHAMBERS provide an accurate measurement in the rz plane parallel to the beam direction thus facilitating a good invariant mass resolution and allowing for good track separation in high multiplicity events or events with nearby tracks like τ multi prong decays. (see Figure 30 on page 46)

Each chamber consists of anode wires parallel to the beam spaced at 2.09 to 2.86 mm, and two planes of cathode strips running at 30° and 90° with respect to the anodes. They allow, in combination with the anode wires, an unambigious reconstruction of space points.

For an accurate measurement in the rz plane, the cathodes are equipped with analog readout, thus making possible a much more accurate measurement than expaected from their width of ~ 4.5 mm. (see Figure 21 on page 31)

layer	type	radius (cm)	# of anode wires	cell width	# of cathodes 90°	30°
1	PC	17.0	512	2.09	258	256
2	PC	21.0	512	2.58	228	256
3	DC	25.5	104	15.41	-----	
4	DC	30.4	128	14.92	-----	
5	PC	35.7	1024	2.19	366	512
6	DC	40.2	168	15.03	-----	
7	DC	45.1	192	14.76	-----	
8	DC	50.0	208	15.10	-----	
9	PC	55.3	1536	2.26	420	768
10	DC	59.8	256	14.68	-----	
11	DC	64.7	256	15.88	-----	
12	PC	70.0	1536	2.86	494	768

Figure 19.   Layer structure of the CELLO inner detector
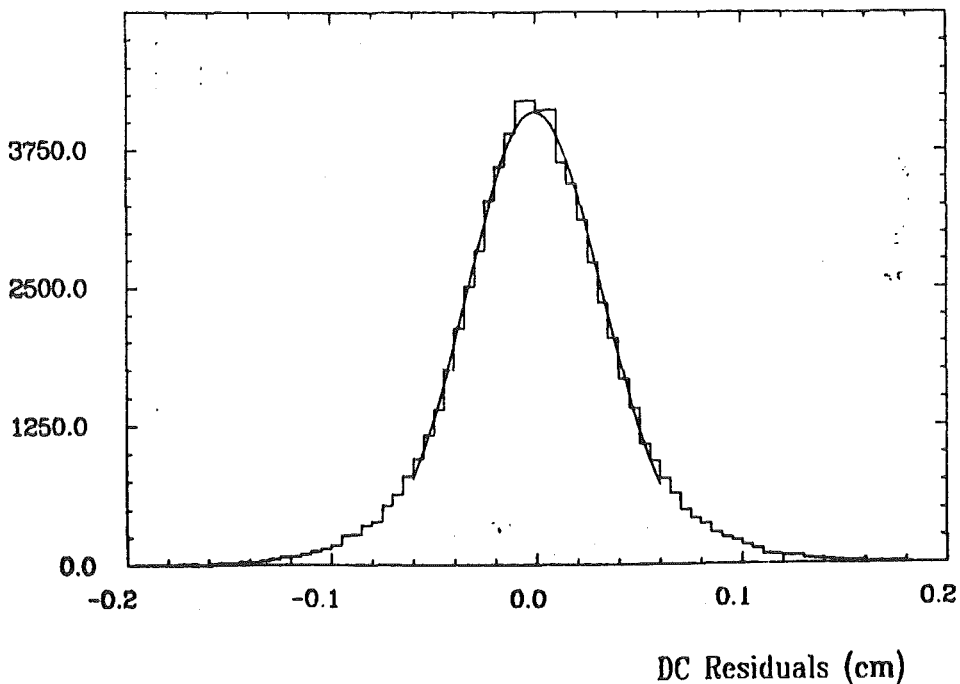
DC Residuals (cm)

Figure 20.   Drift chamber residuals in the rΦ plane for Bhabha events
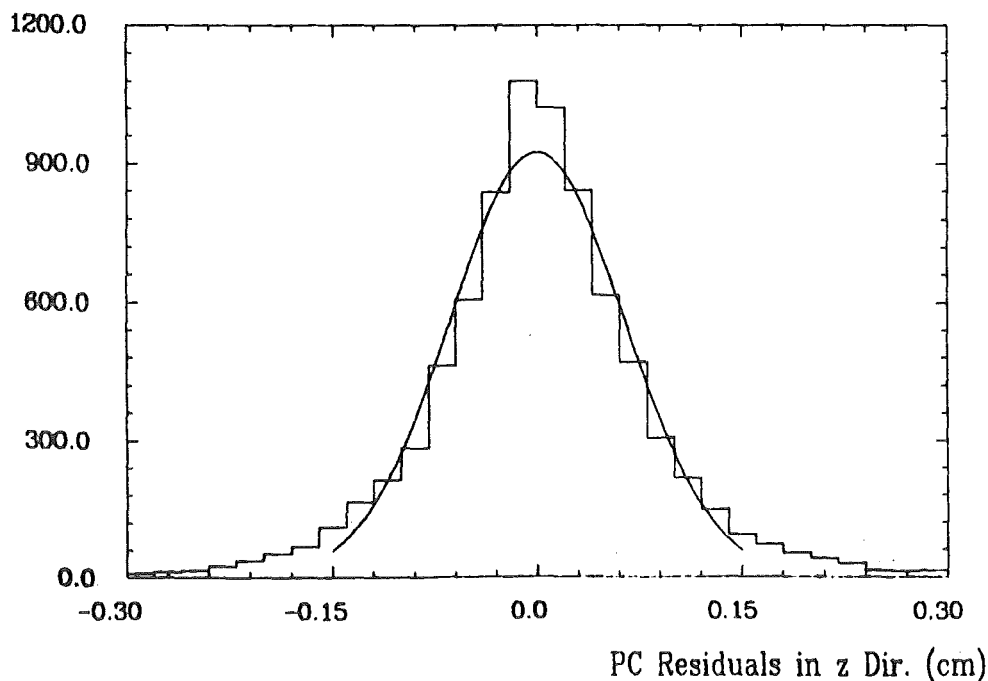
Figure 21.   Prop. chamber residuals in the rz plane

Since the momentum measurement error decreases with the length of the lever arm like $1/L^2$ it is desirable to increase L. This can be done by including the interaction vertex into the track fit.

The interaction vertex has been determined per machine filling by subjecting both tracks of collinear Bhabha events to a common fit (see Figure 24 on page 32). The momentum resolution achieved this way can be determined from Bhabha events to $\Delta p_T/p_T \sim 1.7~\%~p_T$ (GeV) (see Figure 22 on page 32).
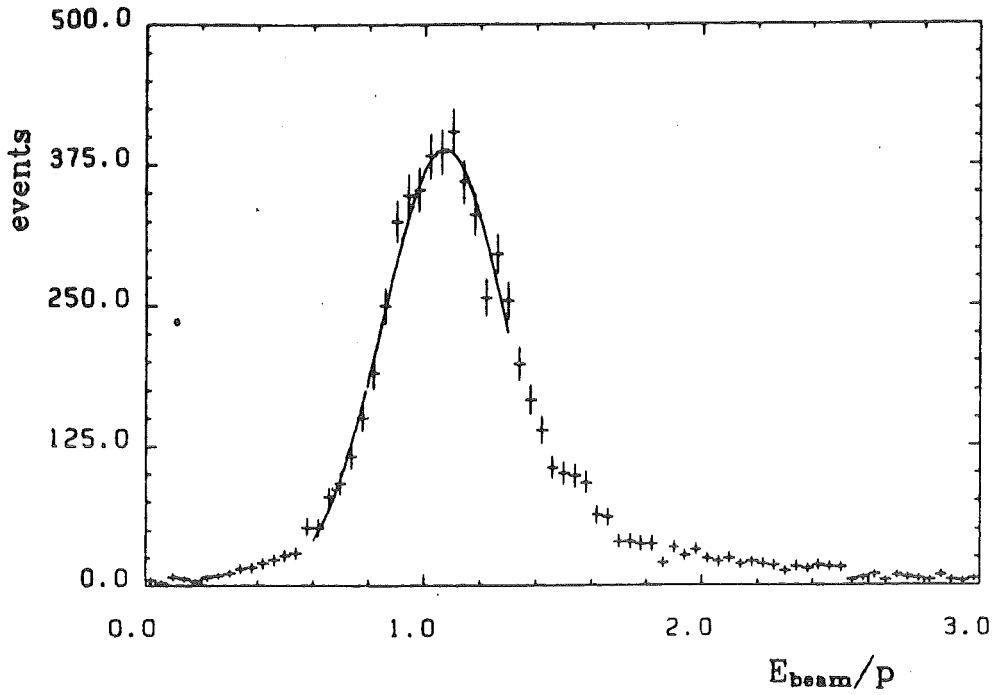
Figure 22.   E(beam)/p, Bhabha events at E(beam) = 17 GeV. The mean p_T in the angular range $|\cos \Theta| < .85$ was 13.6 GeV.
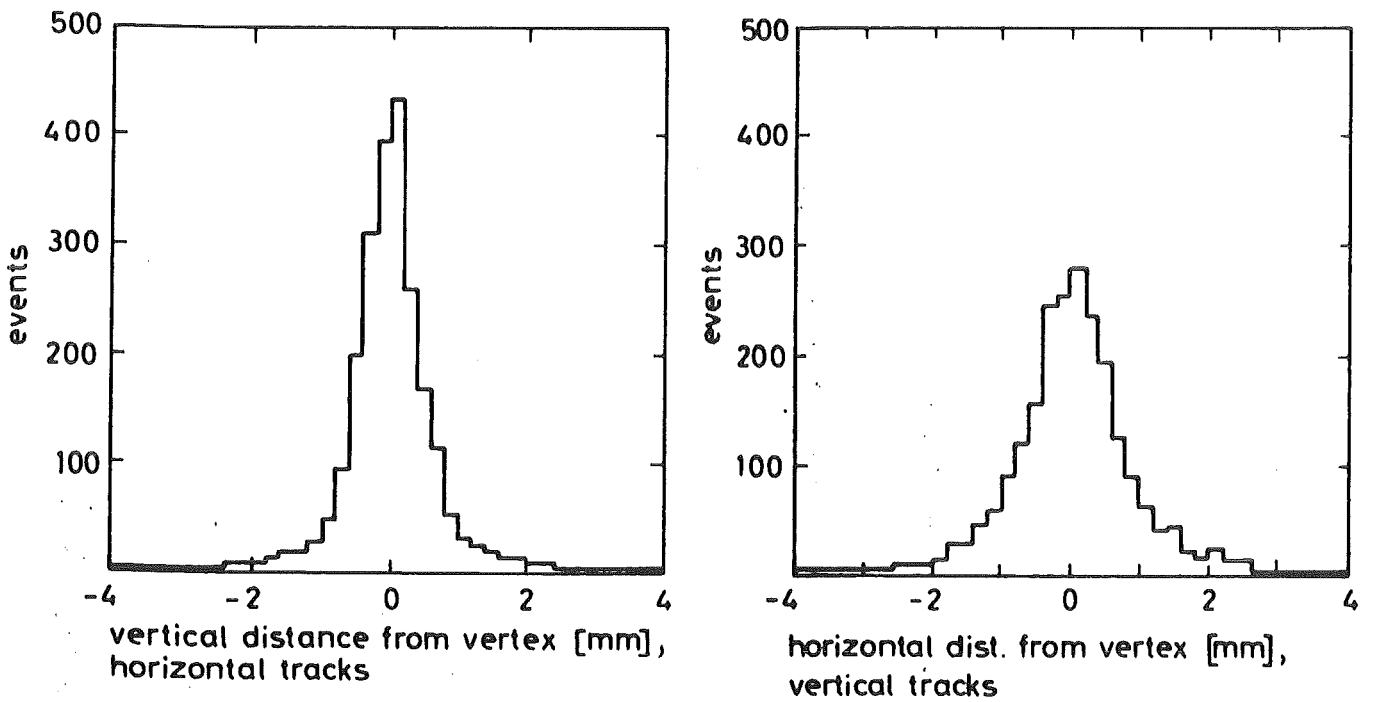
Figure 24.   Min. distance of Bhabha tracks from vertex position,
a.) horizontal tracks
b.) vertical tracks

2.2 The Lead Liquid Argon Calorimeter

For photon detection and electron identification an electromagnetic calorimeter is used. Important design goals were a good spatial and energy resolution even for low energy (> 200 MeV) photons and a good electron-hadron separation over almost the full solid angle. This was achieved by a barrel shaped central calorimeter complemented by two end caps (see Figure 17 on page 28). A fine lateral and longitudinal sampling renders a good spatial and energy resolution. In addition the fine sampling in depth allows to exploit the characteristic differences in the shower
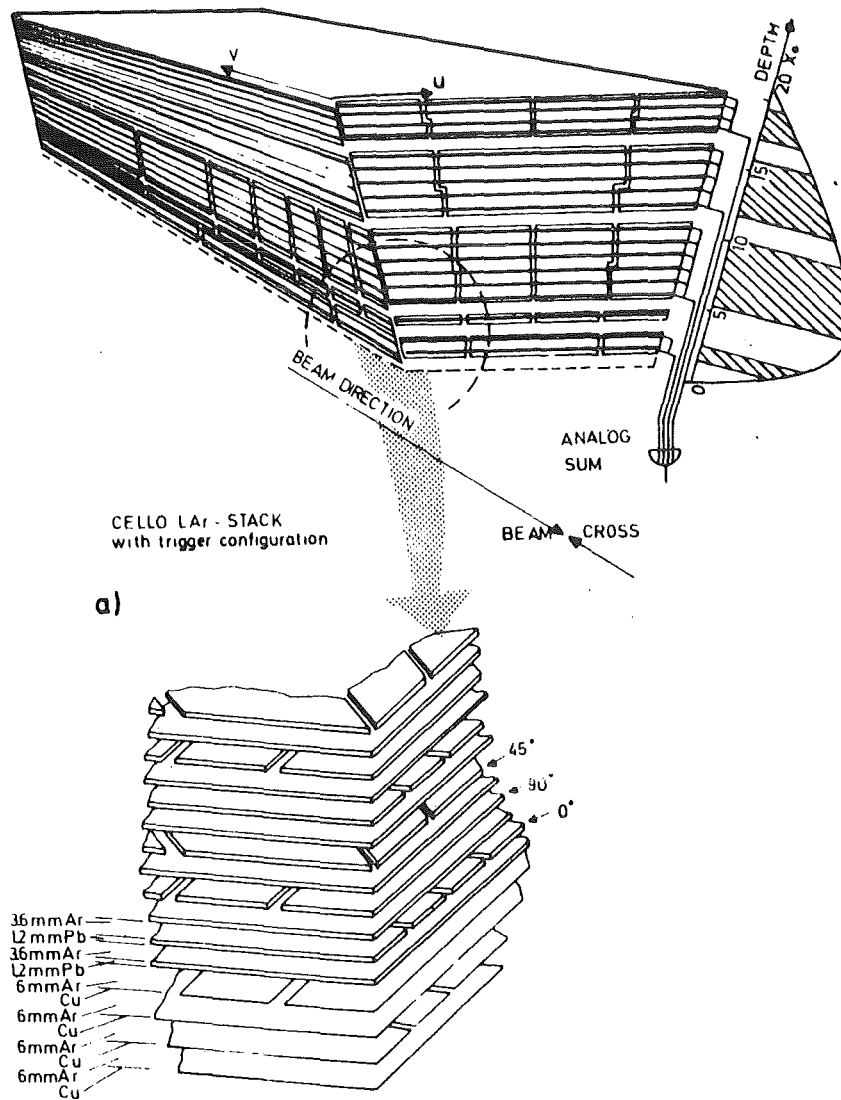
Figure 23.   Structure of the central calorimeter's lead stacks

development for electron-hadron separation. The thin coil (1/2 X_0) facilitates the detection of very low energy photons. A depth of 20 radiation lengths results in a good linearity even for highest energy electrons and photons.

Here I will describe only the central part which was used in this analysis. It covers the polar range $|\cos \Theta| < .86$ and is made up of 16 independent coffin shaped lead stacks in a single cryostat. The structure of a single stack can be seen in Figure 23 on page 33.

They consist of alternating layers of continous lead plates and lead strips running at 0°, 45°, and 90° with respect to the beam axis, the gaps in between filled with liquid argon. The lead plates are 1.2 mm thick with argon gaps of 3.6 mm. The 0° and 90° strips are 2.3 cm wide, whilst the 45° strips, used to resolve the x-y ambiguity in cases of more than one shower in a module, are 3.25 cm wide. The strip width of 2.3 cm coresponds to an angle of ~ 20 mrad seen from the interaction point. In front of each stack there are two additional layers of copper plated epoxy serving as dE/dx gaps. They are used also to determine whether an electron started a shower in the coil.

For readout the signals from the strips are summed up in six electronic layers, each of them containing strips at 0°, 90°, and 45°. (see Figure 25 on page 35) In the first layers were the showers are still narrow each strip is connected to an electronic channel to make possible a precise position measurement. In the back layers many strips are grouped into one electronic channel. For each stack an analog sum is formed using the 0° strips of the electronic layers 2, 3, and 4. They are input to the trigger logic.

The energy resolution can be described by 13% / $\sqrt{E}$ (see Figure 26 on page 35).

The fine longitudinal sampling is very useful in electron-hadron separation as can be seen in Figure 47 on page 72.
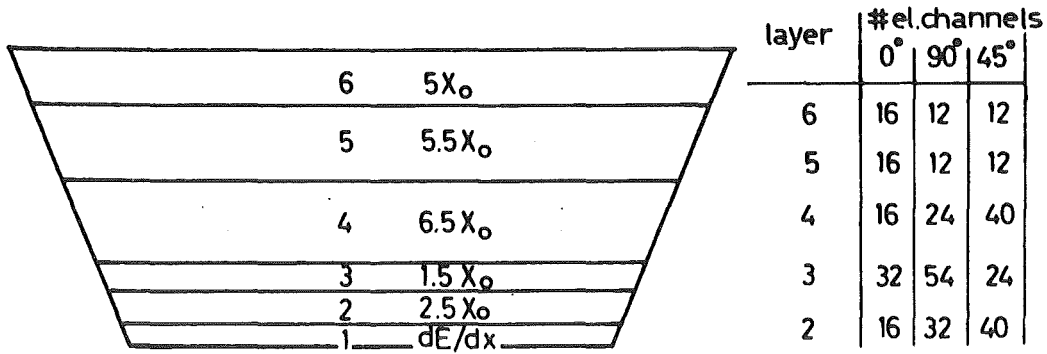
Figure 25.   Layer structure of central calorimeter modules

ENERGY RESOLUTION BEHIND 1.0 X :13.3%/ E +-0.4%
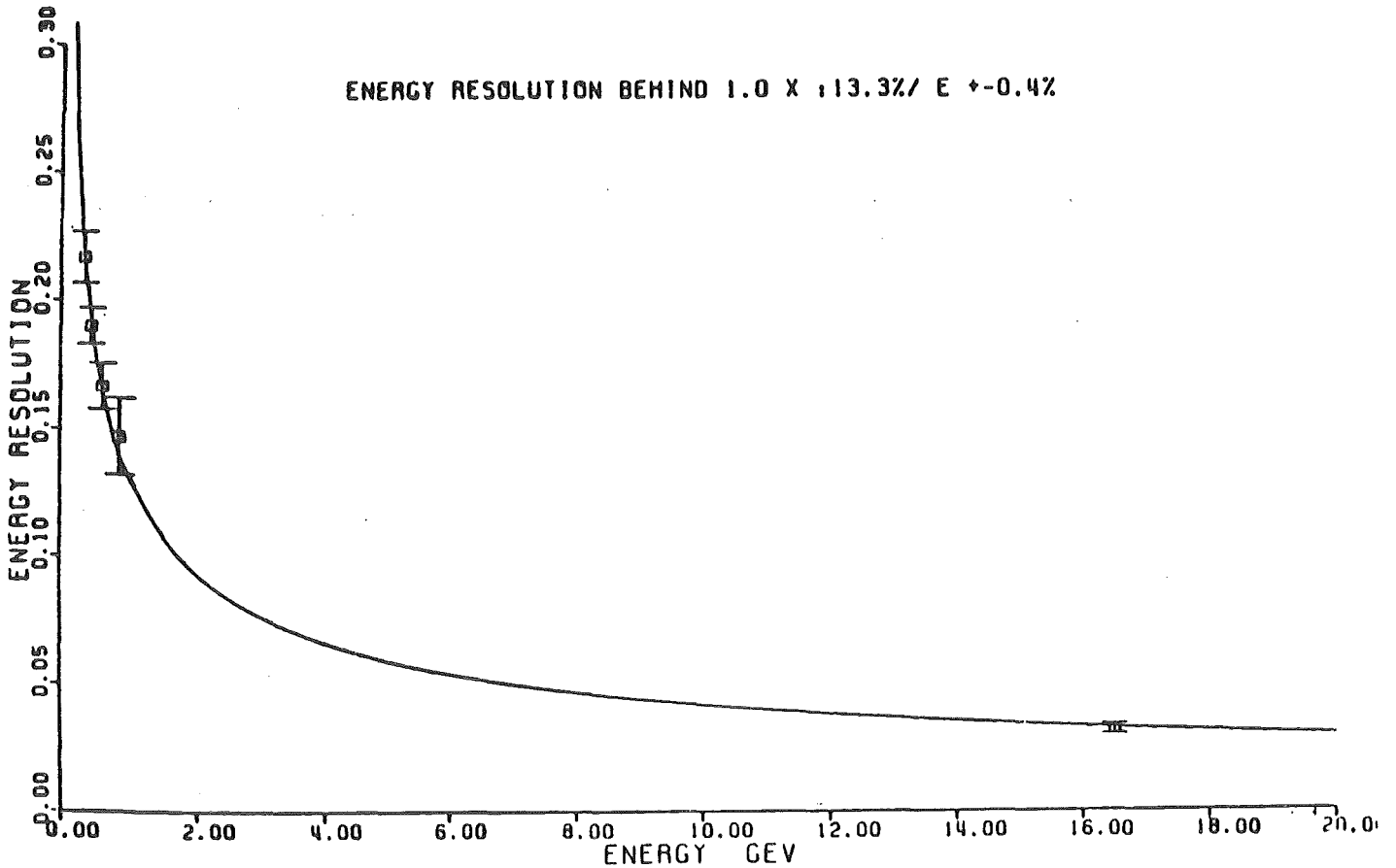
Figure 26.   Energy resolution of the central calorimeter   The low energy points have been determined by using one prong electrons, the point at 17 GeV from collinear Bhabha events.

2.3 The Muon Chambers

Muon identification is achieved by 32 large area proportional chambers behind 6 .. 8 interaction lengths of iron which at the same time serves as flux return yoke (see Figure 17 on page 28). To achieve a solid angle coverage of 91 % of 4π (see Figure 27) the chambers have to cover a total area of about 200 m². The spatial resolution needed is determined by multiple scattering and the quality of the track measurement. The track extrapolation error is ~ 5 cm for 10 GeV muons.

The chambers feature a drift cell structure with proportional chamber read out. The anode wires which are spaced at 12.7 mm and seperated by a field wire are complemented by cathode strips running at ± 34° with respect to the anodes to allow an unambigious reconstruction of space points.
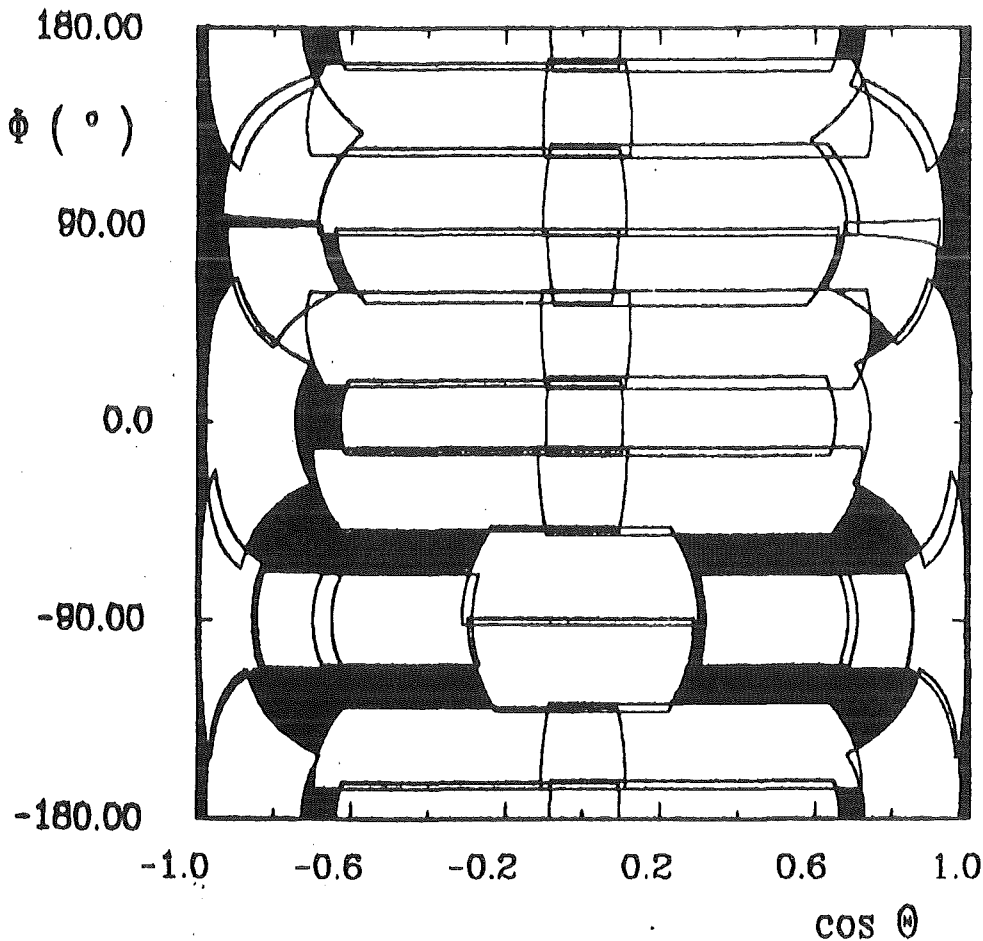
Figure 27.   Solid angle coverage of the 32 muon chambers of CELLO

The precision achieved is ± 6mm both perpendicular and parallel to the anode wires.

2.4   Trigger

The readout of the detector can be initiated by central detector, calorimeter, and forward detector trigger signals and by various combinations of these. For this analysis only the charged (central detector) and neutral (calorimeter) triggers were relevant and I will restrict myself on a brief description of these.

a.) Central Detector Trigger

For triggering on charged tracks in the inner detector and avoiding at the same time triggers due to chamber noise or beam gas events with many low p_T tracks a hardware track finding processor is employed.

It uses the signals from the proportional chamber 90° cathodes to look for straight tracks pointing to the vertex in the rz projection (rz trigger). Signals from the proportional chamber anode wires plus two drift chamber layers serve as input for the rΦ trigger which looks for curved tracks with a minimum transverse momentum of typically 200 MeV.

This is done by feeding the chamber signals into the address lines of a writable random acces memory. For each valid combination of input lines (mask) a logical one is stored in the RAM, indicating that a track candidate has been found. To reduce the number of masks the signal wires are grouped into into 64 sectors in rΦ and 37 in rz, covering the polar range |cos Θ| < .87. Since the RAM can be loaded from the online computer, the trigger can be adapted easily to the experimental conditions.

For a more detailed description of the CELLO charged particle trigger see /30/.

b.) Calorimeter Trigger

For the calorimeter trigger an analog sum is formed for each stack by summing up the charge on the 0° strips of the first three electronic layers corresponding to 10 radiation lengths. (For the resolution of the analog sums see " 1.   Preselection from the Raw Data Tapes" on page 41) The same is done for each of the four end cap modules.

c.) Trigger Conditions

The following triggers have been used in this analysis:

- central detector trigger ('trigger 5'):

  ≥ 2 track candidates in the rΦ projection   and
  ≥ 1 track candidate   in the rz projection

- calorimeter trigger ('trigger 6'):

  ≥ 2 central calorimeter modules above a threshold of 2 GeV, seperated by at least one module in rΦ

- combined central detector and calorimeter trigger ('trigger 3'):

  ≥ 1 central calorimeter module above a threshold of 1.2 GeV and
  ≥ 1 track candidate in rΦ

BD: Branch Driver
CCA1:   Camac Crate Controller TYPA1
CCA2:   Camac Crate Controller TYPA2
IOR: I/O Register
MINI: Minicomputer 32KB
SPY: Dataway Access by Mini
BAG: Block Address Generator
AX+b: Transform Digital Readout to Physical Units
ROBD: Romulus Branch Driver
ROCC: Romulus Crate Controller
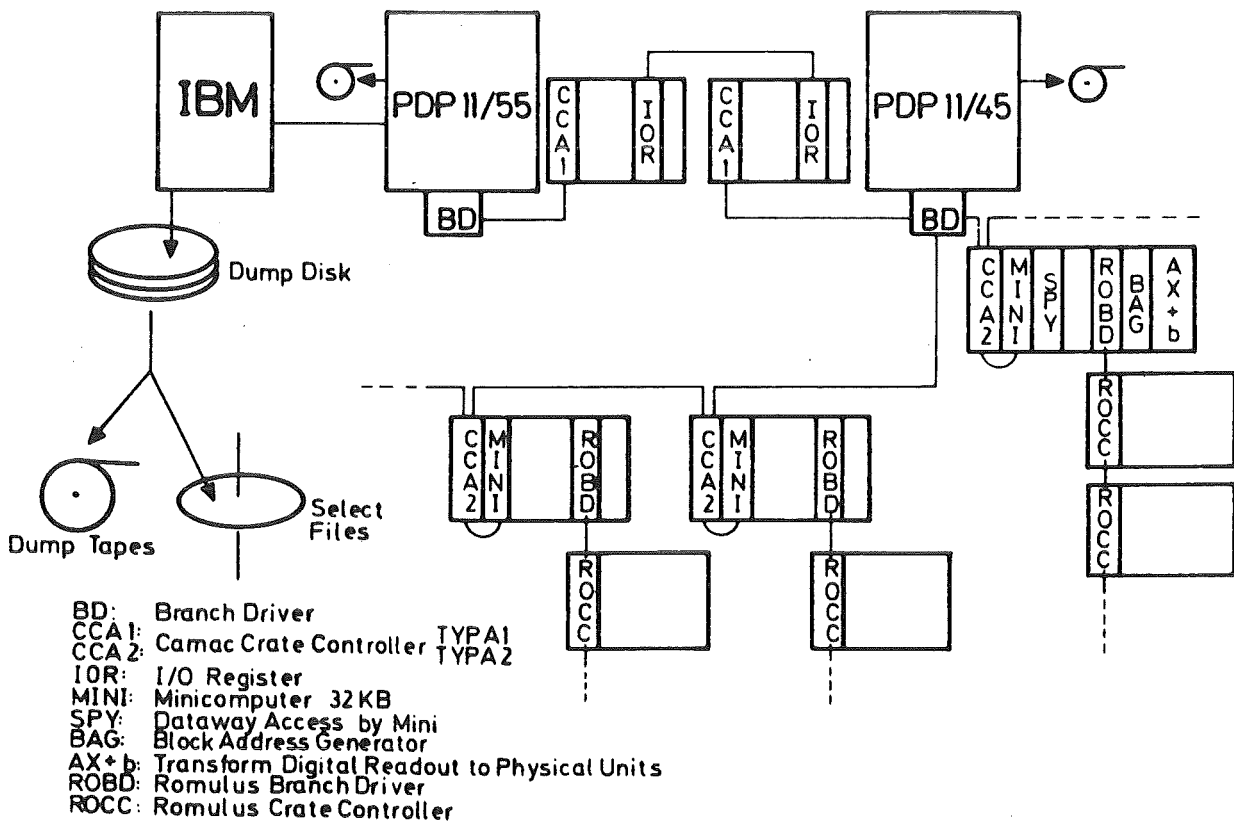
Figure 28.   CELLO data aquisition system

2.5   Data Aquisition

For an overview of the CELLO data aquisition system see Figure 28 on page
39.

The detector is read out by a CAMAC ROMULUS system /31/. It is organized
in branches, one branch for each detector component. The A2 controller
in each branch master crate permits concurrent access to the branch by
both the online computer and by a micro computer located in the crate.
This micro computer in each detector branch is used to test, calibrate,
and monitor it's detector component. .

The two online computers have dedicated tasks. The first one, a PDP
11/45, reads out the detector branches and runs a fast filter program
which discards obvious junk events. The data is passed via a CAMAC link to
a second machine, a PDP 11/55, which does an event buffering, drives the
shift operator console and passes commands to both the IBM online sys-
tem and to the online computer. It also runs various monitor and
histogramming tasks and passes the event records via a fast data link to
the IBM online system which runs on one of the three IBM mainframes of
the DESY computer center.

Here the events are buffered on disk for some hours and eventually
dumped on tape.

IV. DATA SAMPLE AND EVENT SELECTION

The data used in this analysis was accumulated in the period from March to May 1981 mainly at center of mass energies of 34 GeV. The total integrated luminosity is 7270 nb^{-1} of which $\sim$ 600 nb^{-1} were at $\sqrt{s}$ = 33 GeV.

1.   PRESELECTION FROM THE RAW DATA TAPES

To reduce the number of background events to be reconstructed and thus save computer time, a filter was used which makes strong use of the information from the liquid argon shower counters.

In this filter the analog trigger sums which are available for each of the 20 calorimeter modules are used. In addition information from the charged particle trigger was taken into account.

Some cuts were applied to reduce the number of events due to electronic noise triggers. For the events retained one of the following criteria had to be fulfilled:

- $\geqq$ 2 barrel modules above 1150 MeV

- $\geqq$ 1 barrel module above 1150 MeV   and
  one track candidate

- $\geqq$ 2 barrel modules above 600 MeV   and
  one track candidate

- $\geqq$ 1 barrel module above 1150 MeV   and
  $\geqq$ 1 end cap module above 1150 MeV

- $\geqq$ 2 barrel modules above 600 MeV   and
  $\geqq$ 1 end cap module above 1150 MeV

To do these cuts under stable conditions it is important to have a good understanding of the trigger sums, their resolution and their calibration. The resolution can be described by

$$
\frac{\Delta E}{E} = \sqrt{ \left\{ \left(\frac{20\ \%}{E} \right)^2 \right. }
$$ electr. noise

$$
+ \left(\frac{15\ \%}{\sqrt{E}} \right)^2
$$ sampling fluctuations

$$
+ \left. \left(12\ \% \right)^2 \right\}
$$ calibration errors

A more detailed description of the prefilter can be found in /32/.

The main cuts into the τ sample caused by this first step in the selection chain are due to the requirement of at least 1.2 GeV shower energy in one stack of the central calorimeter or 600 MeV in two stacks. A minimum ionizing particle like a muon or a non showering pion deposits typically 200 MeV in the shower counter. So all those τ pairs where both of the τ's decay into non showering particles are lost, namely $\tau^+\tau^-$ into $\mu\mu$, $\mu\pi$, and $\pi\pi$ where none of the π's interacts in the calorimeter. This amounts to ~ 5 % of the produced τ pairs.

In the multi prong decays $\tau \rightarrow \geq 3\pi + \geq 0\pi^0$ mostly at least one π^0 is present or at least one of the 3 charged π's starts an hadronic shower, thus fulfilling the energy selection criteria.

Including the loss of $\mu\mu$, $\mu\pi$, and $\pi\pi$ channels, the overall efficiency of this filter for τ pairs is about 70 %. Here one should note that the requirement of shower energy in the central calorimeter already implies an acceptance cut.

All events passing this filter have been fully reconstructed yielding a data sample of $\sim 77,000$ events at 34 GeV center of mass energy.

2. EVENT RECONSTRUCTION

The reconstruction of tracks in the inner detecor and showers in the calorimeter is done by three processors: CELPAT does the track finding in the inner detector, CELGEOM performs a re-fit for the tracks found by CELPAT taking into account the exact magnetic field and the position of the interaction vertex. LATRAK reconstructs showers in the calorimeter. These processors are called by a general frame program for offline reconstruction ('OFFRAM') which does the management of event records, detector constants, etc.

CELPAT consists of two parts:

ANOCAT reconstructs space points in the cylindrical proportional chambers by making associations between 90° and 30° cathode strips and the anode wires.

RFIPAT looks for tracks in the $r\Phi$ projection perpendicular to the beam axis using both drift and prop. chambers. To reduce the number of combinations the $r\Phi$ projection is divided into overlapping sectors. The track circle is required to lie within one sector, so the sector width corresponds to an implicit momentum cut. Searching for tracks whithin these sectors is done by a road method. Hits which have been used in an accepted track are eliminated for further searches.
Great flexibility is achieved by specifying parameters such as track quality criteria, sector width, search order, etc. in a program steering matrix ('PROM'). The normal mode of operation is to run CELPAT in several subsequent passes with the cuts loosened from pass to pass. So stiff tracks from the vertex are found and eliminated first and in further passes a good efficiency is maintained even for low momentum tracks which don't point to the interaction region, as for instance K^0_s decays.
After the track finding in the $r\Phi$ projection, RZPAT looks for tracks in the rz projection using only cathode hits which are associated with anode hits belonging to tracks in $r\Phi$.

CELGEOM

This program refits each track using the points found by CELPAT. For this it takes into account the real (slightly inhomogeneous) magnetic field and, optionally, also the interaction point. (for the determination of the interaction point see " 2.1 Inner Detector" on page 29) This increases the lever arm of the track measurement and improves the momentum resolution drastically.

LATRAK

This processor reconstructs showers in the calorimeter. The first step is the reconstruction of two dimensional clusters in each of the six electronic layers (each layers contains 0°, 90°, and 45 ° projections). Then the clusters are checked for a possible structure indicating a double cluster from overlapping showers. All tracks from the central detector are extrapolated into the calorimeter and it is checked whether it is possible to assign a three dimensional sequence of clusters (i.e. a shower) to the track. A line fit taking into account the center of gravity of the used 2D clusters and the extrapolated entry point of the track into the calorimeter is performed. From the remaining 2D clusters three dimensional clusters are built using the three dimensional correlation between cells. The shower axis is determined by a line fit including the interaction point. Care is taken to resolve overlapping showers and assign the proper energy to each of them.

3. τ SELECTION

Due to the good particle identification in the CELLO detector over a large solid angle it was possible to use all τ decay topologies, both the 2 prong and the various multi prong final states. Figure 30 on page 46 and Figure 29 show a typical candidate of each decay category.

2 prong and multi prong events were selected separately.
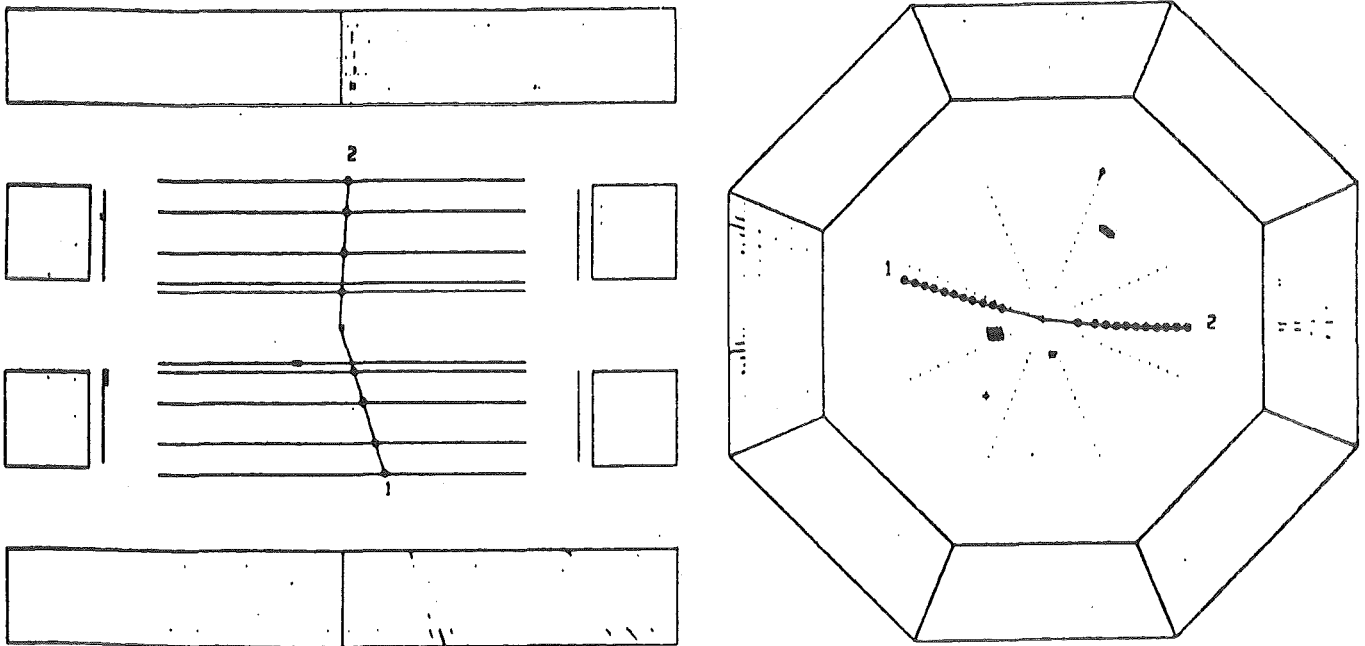
Figure 29. 2 prong τ pair candidate:

$$\tau^- \to e^- \nu \nu$$
$$\tau^+ \to \pi^+ \nu$$

The electron and the pion can be clearly distinguished by their typical showering behavior: the electron shower starts early and is fully contained in the calorimeter, the track momentum matches the shower energy. The pion starts a wide hadronic shower late in the calorimeter, most of the energy leaks out.
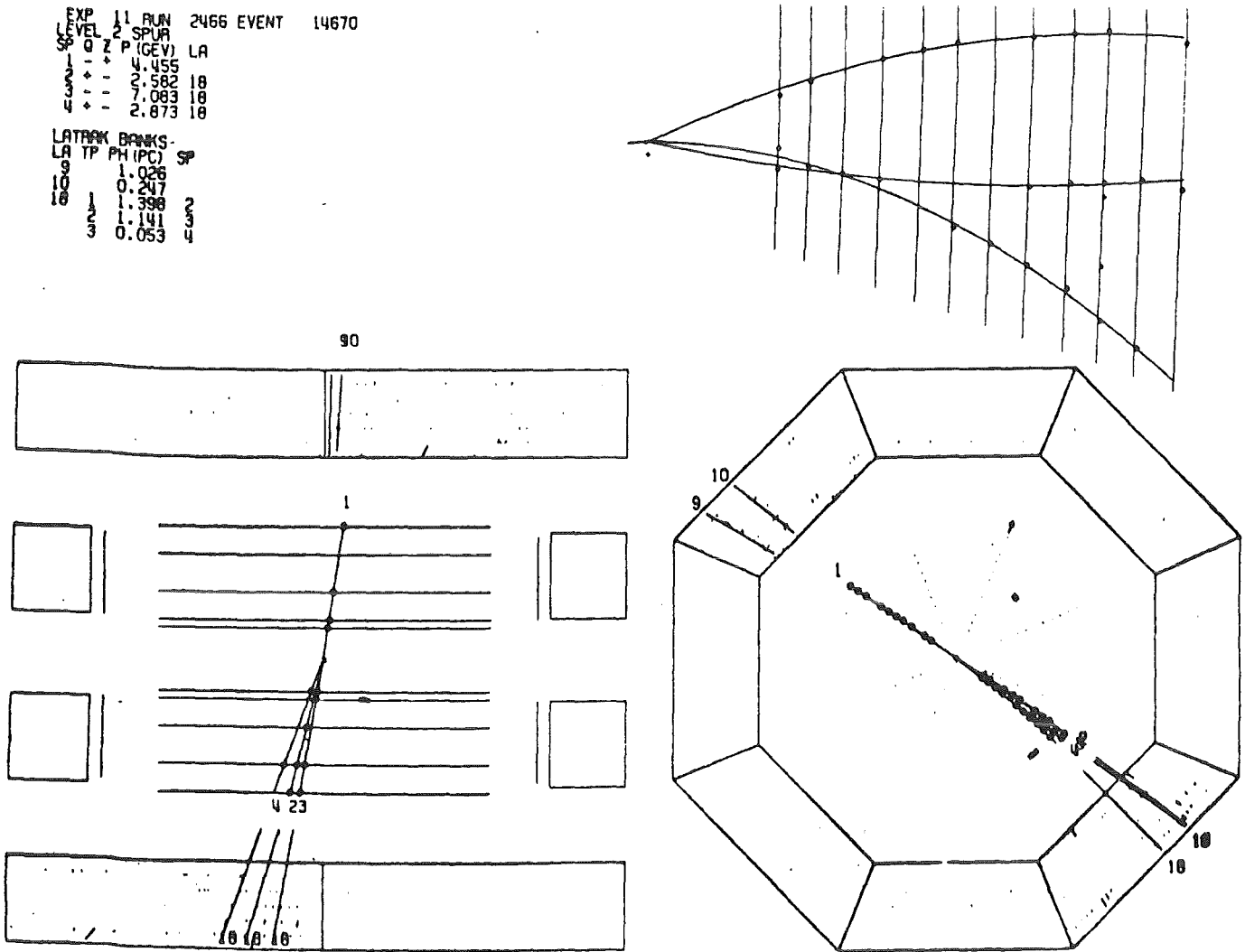
Figure 30. Multi prong τ pair candidate:

$$\tau^- \to \rho^- \nu \to \pi^- \pi^0 \nu$$

$$\tau^+ \to \pi^+ \pi^+ \pi^- + n\pi^0 + \nu$$

The π^0 from the ρ decay is clearly visible as two electromagnetic showers seperated from the charged track. The expanded view of the inner detector shows that all tracks have an opening angle relative to each other, i.e they are not due to converted photons. Owing to the proportional chambers pattern recognition is no problem even with very close by tracks.

a.)   2 Prong Selection

The most important sources of background for this topology are

* Bhabha events   and

* events from 2 photon collisions

Bhabhas can be rejected by cuts in the total e.m. energy, in acolinearity and acoplanarity (see Figure 31 on page 48 and Figure 32 on page 49).

Two photon events generally have small invariant masses and are suppressed by a minimum invariant mass cut. (see Figure 33 on page 50).

The following cuts have been chosen to select τ pairs and reject background efficiently:

* 2 tracks with p > 400 MeV within $|\cos \Theta| < .85$

* vertex cut requiring a distance from the interaction point in rz $d_{rz} < 5$ cm to suppress cosmics and beam gas events

* cuts mainly to reject Bhabhas:

    — cut in the total e.m. energy as measured by the analog sums: $E_{tot,em} < .6 \sqrt{s}$ (see Figure 32 on page 49)

    — $1.5° <$ acolinearity $< 35°$ (see Figure 31 on page 48)

    — $.7° <$ acoplanarity

* cut in the invariant mass of the two tracks (> 3.5 GeV) to suppress all kinds of 2 photon background (see Figure 33 on page 50)

* one of the 16 calorimeter modules was not operational during data taking. Events where one of the tracks pointed into this module were rejected

After these cuts we are left with 586 events which were scanned twice to remove residual background. All events with electrons on both sides were rejected on the basis of energy momentum matching and their typical showering behaviour in the calorimeter, since this channel is flooded by electron pairs from two photon reactions. Also removed were remaining events with two minimum ionizing tracks ($\mu\mu$'s, $\mu\pi$'s, or $\pi\pi$'s without pion

interaction in the calorimeter) which passed the prefilter for instance due to an additional radiative photon.

Most of the of events rejected during the scan were e-e events ($\sim$ 40 %), Bhabhas pointing into a gap between the lead modules and thus passing the energy cut ($\sim$ 25 %), and cosmics ($\sim$ 15 %).

After the scan 136 τ 2 prong candidates are left.

b.)   Multi Prong Selection

Here use has been made of the characteristic topology of τ multi prong decays: two narrow (low mass) low multiplicity back to back jets.
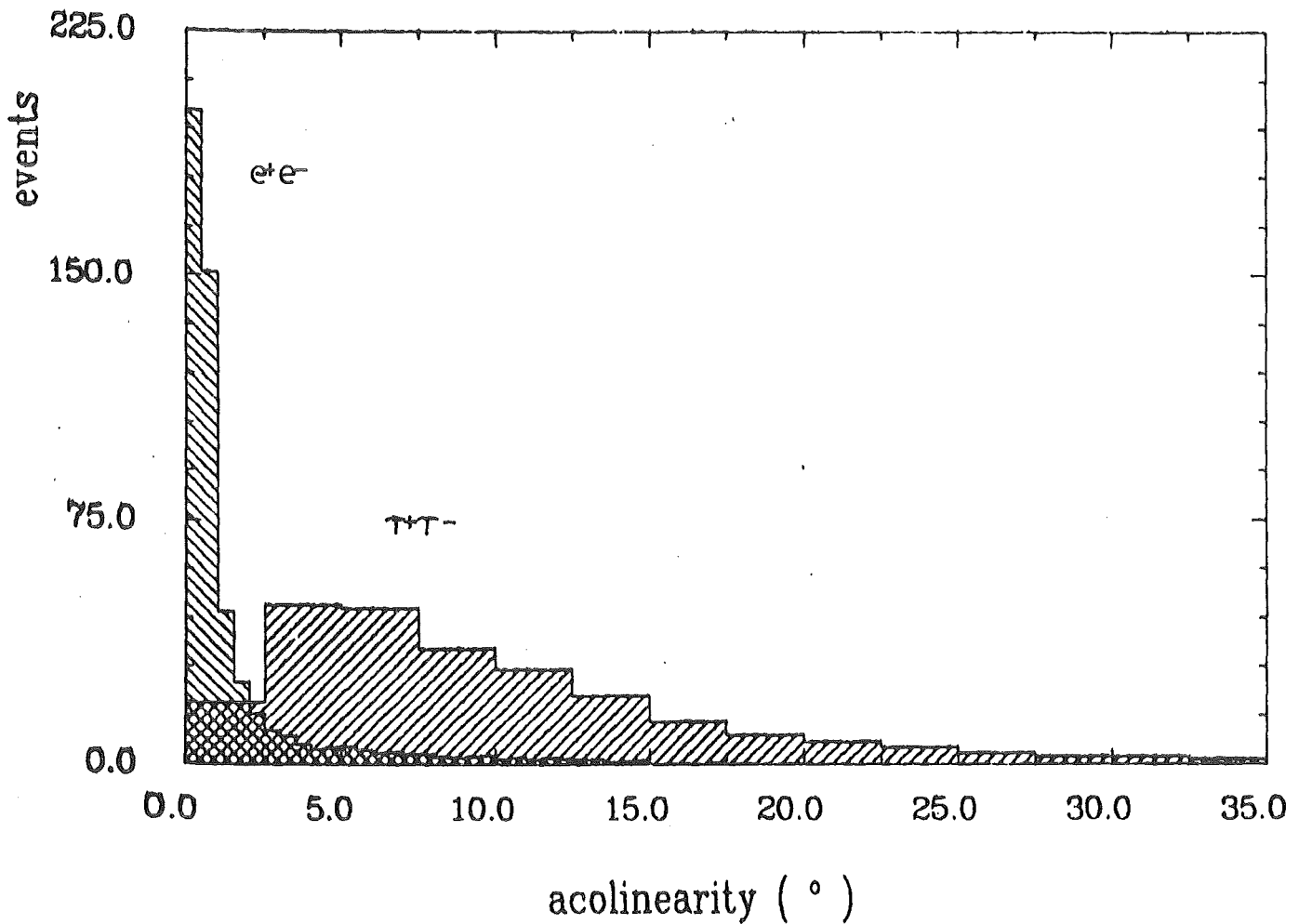
Figure 31.   Acolinearity   distribution   of   Bhabhas   and τ 2 prongs.   Bhabhas are scaled down by a factor of 200.

The following reqirements have been made:

- ≥ 3 reconstructed tracks

- from now on, only 'good' tracks are considered:
  - track found in both, rΦ and rz, projections
  - track within acceptance |cos Θ| < .85

- between 2 and 8 'good' tracks to allow for converted photons

- at least 50 % of the tracks must have a good vertex, i.e. a distance from interaction point of < 2.5 cm in the rΦ plane and < 5 cm in the rz plane. This cut rejects most of the beam gas and beam wall back-
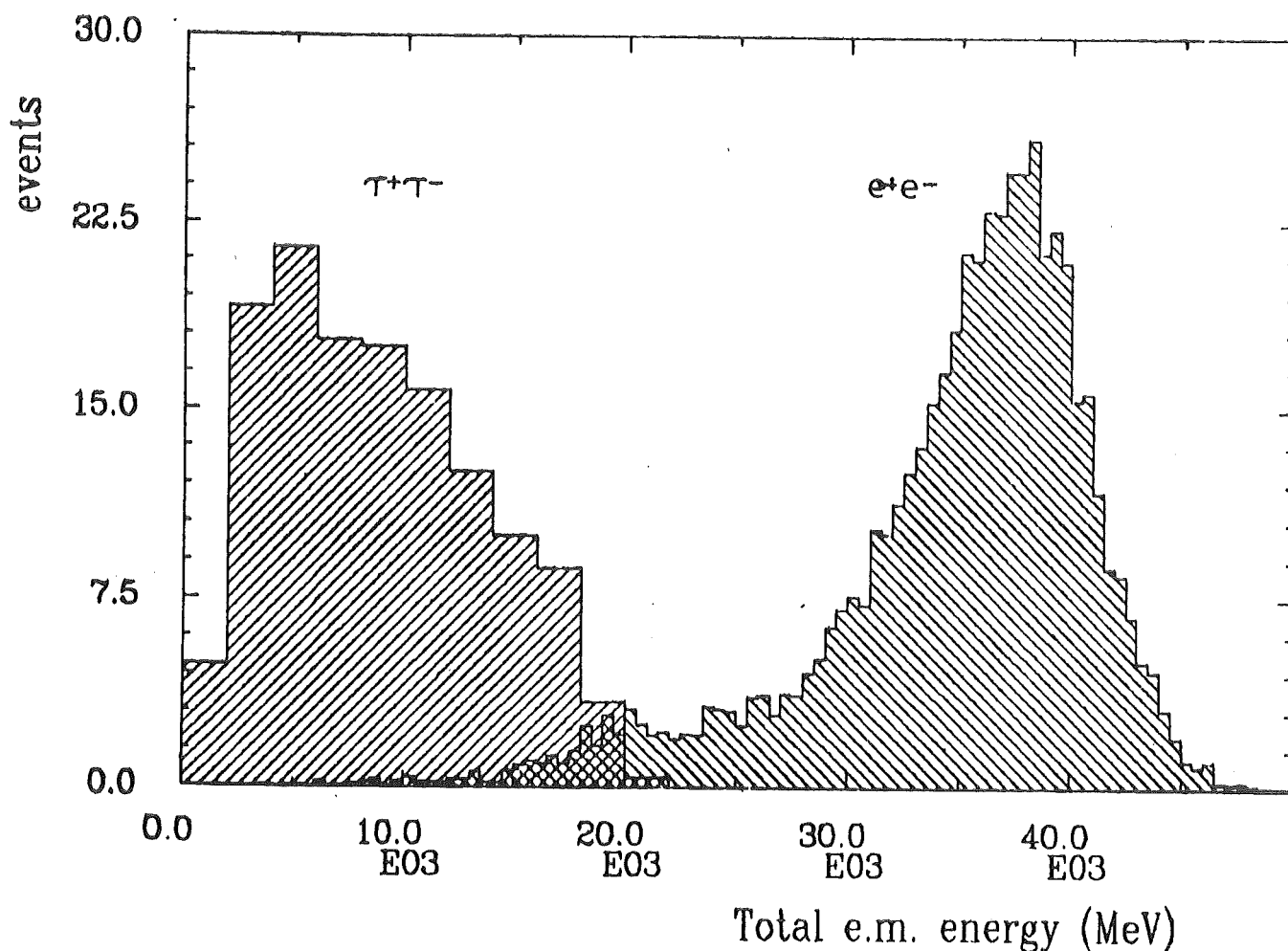
Figure 32. Total calorimeter energy as measured by the analog trigger sums. Bhabhas (scaled down by a factor of 80) and τ two prongs

ground and permits converted photon tracks which generally don't point to the vertex in the rΦ plane

- a cut in the visible momentum $p_{vis} > 5$ GeV removes 2 photon and beam gas background

- a cut in the total energy deposited in the central calorimeter $E_{tot,em} <$ 25 GeV removes most of the Bhabha events which sneaked into the multi prong sample due to a converted photon

- an acceptance cut is applied on the sphericity axis to exclude edge effects: $|\cos \theta_{sp}| < .8$
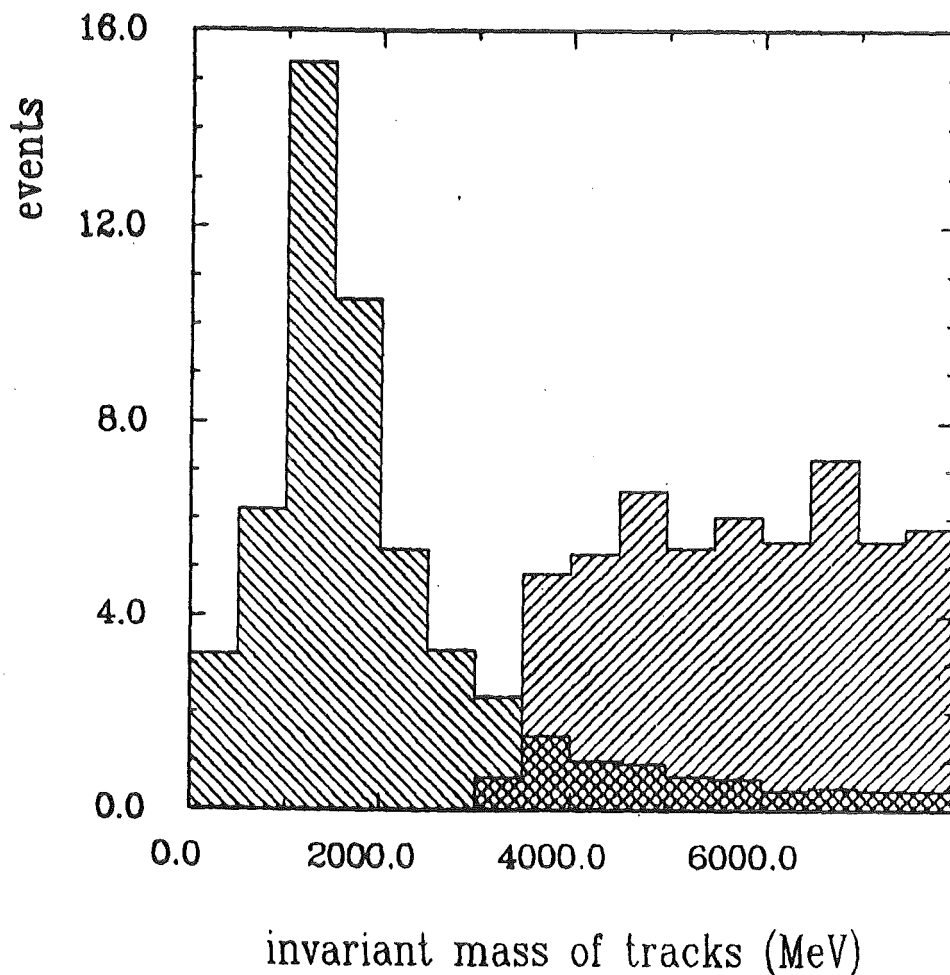
Figure 33. Invariant mass distribution of two prong events. The peak at the left shows all 2 prong events within acceptance (not normalized). It is mainly due to 2 photon processes. The other histogram shows τ 2 prong Monte Carlo events.

- the following topology requirement is made: all tracks have to lie in one of two 120° cones around the sphericity axis, at least one track in each cone

- each of the two jets have to have an invariant mass (computed from the charged tracks only) of less than 2 GeV. This requirement suppresses multi hadron background.

- the acolinearity between the two jet axes is required to be less than 35°

All 281 events remaining after the automatic selection were scanned twice to remove residual background, mainly due to Bhabhas with converted photons and hadronic events. After the scan 115 multi prong candidates are left. They include also those two prong τ pairs were a photon converted in the beam pipe, thus mimicring the multi prong topology.

c.)   The τ Sample

In conclusion, all τ decay topologies were accepted. The only channels excluded are $\tau^+\tau^- \rightarrow e^+e^-$ and $\tau^+\tau^-$ into two minimum ionizing tracks like $\tau^+\tau^- \rightarrow \mu\mu$, $\mu\pi$, or $\pi\pi$ were none of the pions interacts in the calorimeter. Thus we are sensitive to ~ 92 % of the produced τ pairs.

The final τ sample consists of 251 events, 136 2 prongs and 115 multi prongs or 2 prongs with converted gammas, from a total integrated luminosity of 7200 nb^{-1} at a mean center of mass energy of 34 GeV. From the scan we get the following decay distribution (for more detailed final state identification see chapter VII) :

>   84 electrons
>   109 muons or pions
>   175 'rhos' where we call a rho any minimum ionizing track with additional photons from π^0 decays
>   37 1 prong decays with converted photon(s)
>   91 3 prong decays
>   3 5 prong decays
>   3 other (not identified decays)

V. ACCEPTANCE AND EFFICIENCY CORRECTIONS

1. TRIGGER EFFICIENCY

τ events were triggered by 3 independent trigger requirements (see also " 2.4   Trigger" on page 38) :

* a central detector trigger requiring only two track candidates with p_t > 200 MeV in the central detector ('trigger 5')

* a pure calorimeter trigger requiring > 2 GeV energy deposition in two calorimeter modules separated by at least one module (45 °) in Φ ('trigger 6')

* a combined central detector and calorimeter trigger requiring 1 track candidate in the inner detecto and one calorimeter module above 1.2 GeV ('trigger 3')

Since the triggers are independent, their efficiency for τ pairs can be determined by mapping one class of triggers on the other. In addition, the 2 prong efficiency of the charged particle trigger has been determined with high statistics using Bhabha events.

From that the trigger efficiency can be determined to 98.7 ± .5 % for τ 2 prongs and 99.8 ± .2 for multi prongs.

2. MC SIMULATION AND DETERMINATION OF SELECTION EFFICIENCY

To correct for detector acceptance and efficiencies, selection and reconstruction losses, and for higher order QED processes a Monte Carlo Simulation has been made.

a.)   Four-Vector Generation

First τ pairs were generated using a program due to Berends and Kleiss /12/ which takes into account initial state radiation, leptonic and hadronic vacuum polarization, and vertex corrections (see Figure 5 on page 9). The energy of the radiated photon was limited to k_{max} = .97. Final state radiation and two photon exchange box diagrams can be neglected for acceptance calculations due to the high τ mass. (see also " 1.1   Production" on page 6)

Then the τ's are decayed according to V-A leptonically or either in one of the resonant channels (π, ρ, A_1) or into a non resonant multi pion final state. Cabbibo suppressed decays for instance into K or K* have been neglected.

Little is known about the non resonant decays of the τ. We treated them in the following way: generate a neutrino according to a V-A spectrum and assign the remaining momentum to the hadronic system. Then determine the charged multiplicity (2/3 3 prongs and 1/3 1 prongs). The total multiplicity is generated according to $e^+e^- \to$ hadrons data at the corresponding center of mass energy.

Figure 34 shows the branching ratios which were input to the four vector-generation.

b.) Detector Simulation

The four-vectors from the τ decays are input to a complete simulation of the detector. The simulation is done in two steps, namely first the particle tracking through the detector geometry and simulation of particle interactions with the detector material (program 'PTRAK'), and secondly the raw data record is build from the tracking information, taking into account all the information on the detector status like chamber efficiencies, dead channels, etc. (program 'CELINT').

channel	branching ratio [%]	
$\tau \to e\nu\nu$	17.5	
$\tau \to \mu\nu\nu$	17.5	
$\tau \to \rho\nu$	24.0	one prongs: 84.5 %
$\tau \to \pi\nu$	12.0	
$\tau \to A_1\nu \to \pi\pi^0\pi^0\nu$	4.5	
$\tau \to \pi + n\ \pi^0$	9.0	
$\tau \to A_1\nu \to \pi\pi\pi\nu$	4.5	multi prongs: 15.5 %
$\tau \to \pi\pi\pi + n\ \pi^0$	11.0	

Figure 34.   Branching ratios used in four-vector generation

PTRAK/33/

uses the EGS shower simulator /34/ to simulate the behaviour of electrons and photons in the detector material whereas the HETC shower code /35/ has been choosen to transport μ's, charged π's, neutrons and protons. Both programs have proved to provide a realistic simulation of particle interaction with matter over a very wide range of energies.

For EGS a very detailed description of the detector geometry is provided incorporating the beam pipe, cryo tanks, coil, and the individual lead and argon layers in the calorimeter. For HETC the calorimeter geometry has been simplified by assuming a uniform medium of lead and liquid argon. π^0's produced in the hadronic shower cascade are decayed into photons which are fed into EGS.

CELINT

builds a raw data record from the information given by PTRAK like chambers and wires hit, charge deposition in the calorimeter layers, etc. For that it uses the measured detector constants like chamber efficiencies,
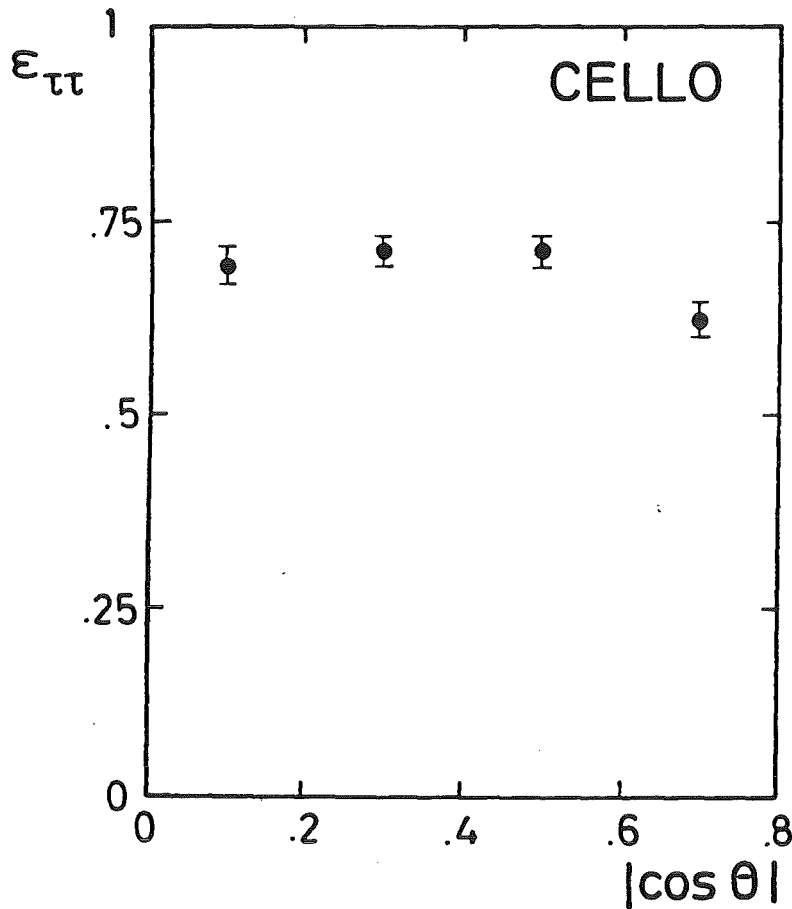
Figure 35. Detection efficiency for τ pairs

slopes and pedestals of the individual calorimeter channels, information on dead channels, etc. In addition, simulated electronic noise is interspersed into the inner detector and calorimeter channels and the trigger electronics is simulated.

c.)   Selection Efficiencies

The output of the detector simulation is a raw data record which can be treated in exactly the same way as real data. First the pre filter program is run, and it's output is passed through the same reconstruction chain (track finding and shower reconstruction) as the data.

After the reconstruction, the events are subjected to the τ selectors. The events left are used to determine the losses due to detector acceptance, detector inefficiencies, reconstruction inefficiencies, and selection cuts. The efficiency of the pre-selector has been found to be 69 % for 2 prongs and 75 % for the multi prong topologies. The total efficiency taking into account reconstruction and τ selection cuts is 44 % for 2 prongs and 58 % for multi prongs, the total efficiency beeing 48 %. (all the efficiency numbers are with respect to 1st order QED expectation, i.e. for events without hard radiation)

Figure 35 on page 55 shows the variation of the detection efficiency with the polar angle. It can be seen that the good solid angle coverage and particle identification in CELLO leads to a high and uniform efficiency, comparable with what can be achieved for μ pair production.

VI. BACKGROUND DETERMINATION

Background sources for the 2 prong topology are

- Bhabha events

- electron pairs from the two photon process $e^+e^- \to e^+e^-e^+e^-$

- τ pairs from 2 photon collisions

- $e\mu$ events faked by 2 photon μ pair production $e^+e^- \to e^+e^-\mu^+\mu^-$

- μ pairs with hard radiation faking $\mu\rho$ events
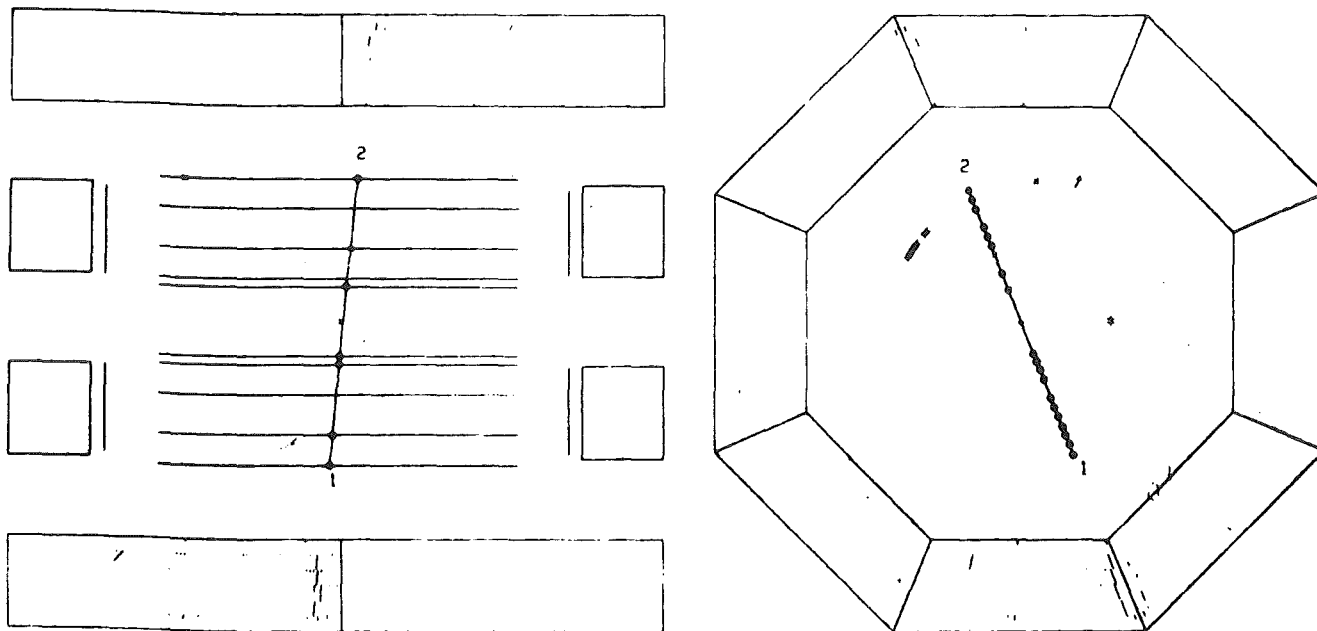
Figure 39. Bhabha event rejected by scan. Although both tracks enter a gap between calorimeter modules they still can be clearly recognized as electrons.

Bhabhas are suppressed effectively by the cuts in total energy, acolinearity and acoplanarity. Bhabhas which pass these cuts are either due to hard radiation or they passed because one electron enters one of the 2 cm wide gaps between the calorimeter modules. They are removed effectively at the scan (see Figure 39 on page 57).

In the same way all other ee events, which are mainly due to electron pair production in two photon collisions, are removed on the basis of their typical showering behavior in the calorimeter and energy-momentum matching (see Figure 36). The maximum contamination from Bhabha scattering or two photon electron pairs has been estimated to be less than 1 % respectively.
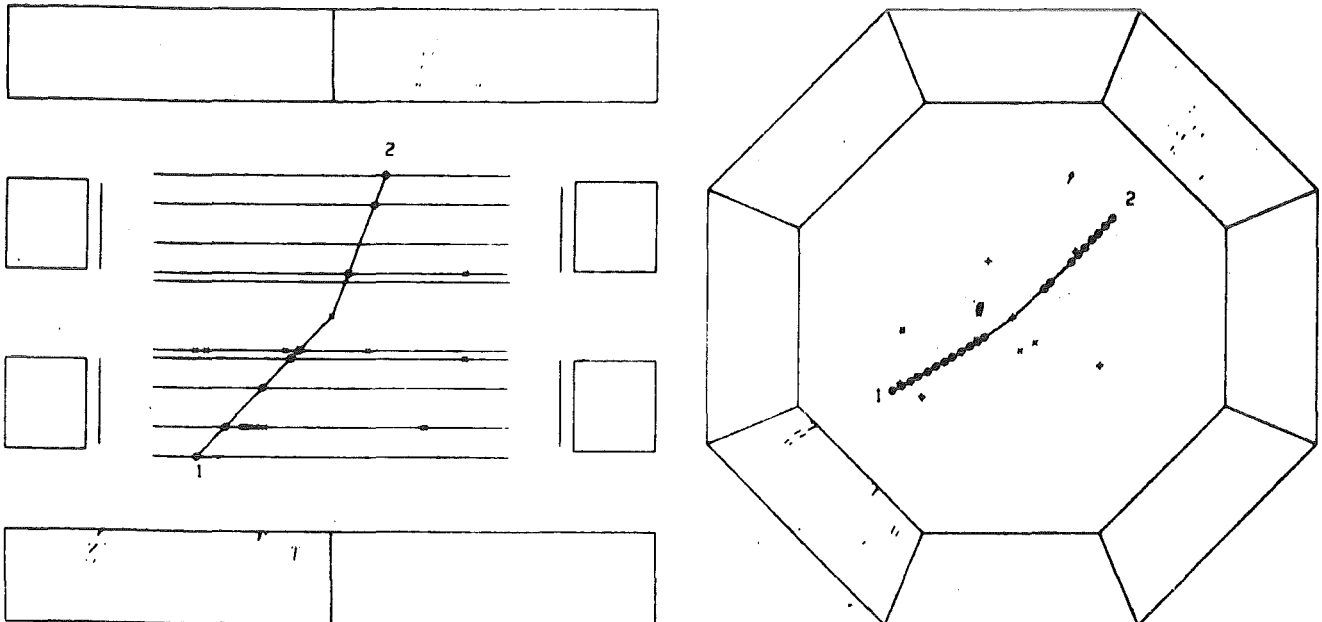
Figure 36.   Two electron event (probably from ee → ee ee) rejected by scan

Since events with two minimum ionizing tracks are rejected, the process $e^+e^- \rightarrow e^+e^-\mu^+\mu^-$ can fake τ pair events only if one electron and one muon appear under large angle while the other two tracks remain outside the detector's acceptance. A Monte Carlo simulation shows that we expect one event in our data sample, corresponding to a contamination of .4 %. Half of these events will have two equal sign tracks, and we actually find one $e\mu$ event with equal sign tracks in our data sample.

μ pair events with hard radiation can fake $\mu\rho$ events if the invariant mass of one μ and the radiated photon is within the ρ band. A Monte Carlo study shows that we expect one event of this kind in our data sample.

The most important background in the multi prong topologies is feed down from low multiplicity multihadron events. It has been estimated by pass-
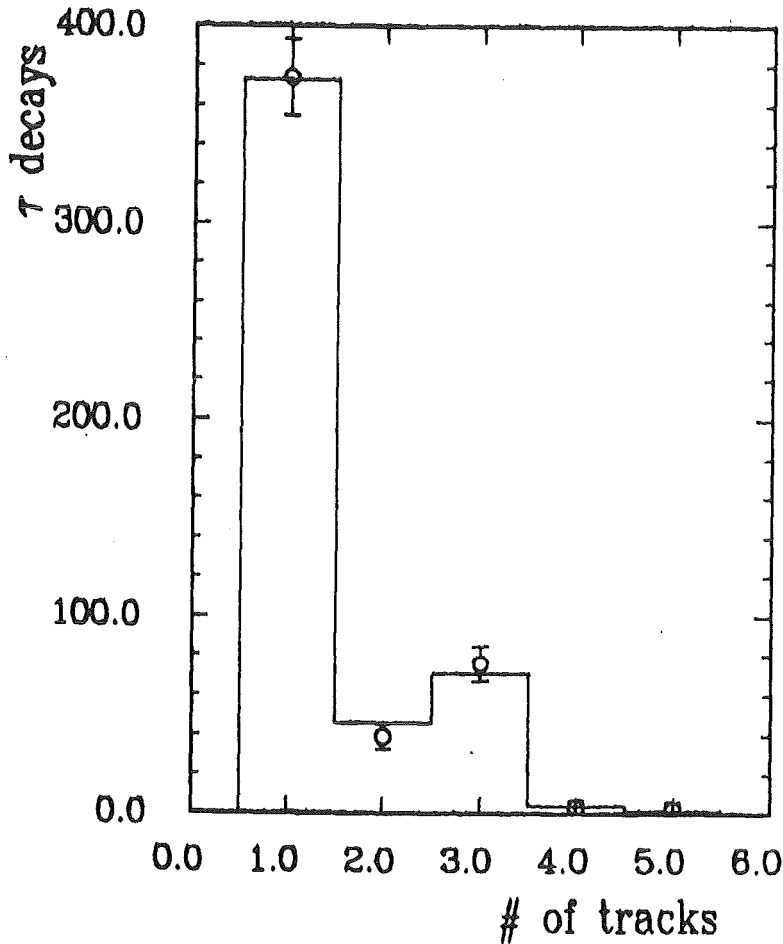
Figure 37. τ decay multiplicity   for tracks with

- distance from vertex in rΦ < 2.4 cm   and
- p > 500 MeV.

ing Monte Carlo multi hadron events through the multi prong selector and subjecting the output to the same scan criteria as used for the data. From this we expect a multi hadron contamination of (2.4 ± 1.0) %.

τ pairs from two photon collisions $(e^+e^- \to e^+e^-\tau^+\tau^-)$ are strongly suppressed by the invariant mass or visible momentum requirements in the 2 and multi prong selector respectively. A Monte Carlo Study shows that we expect (2.5 ± 1.0) % contamination from this production mechanism.

The acolinearity distribution (Figure 38) is sensitive to background from two photon processes and a large background from hadron production would show up in the decay multiplicity distribution (Figure 37 on page 59). Both show a good agreement between data and Monte Carlo prediction.
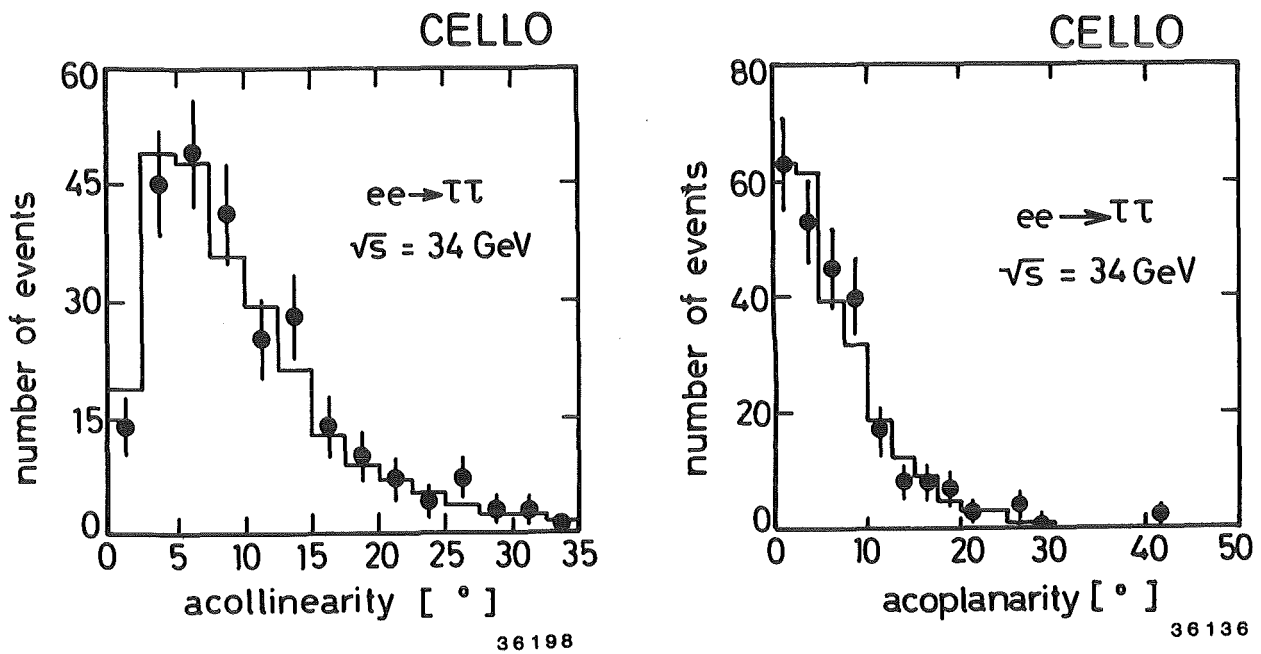
Figure 38. Acolinearity and acoplanarity of τ pair events, compared with Monte Carlo calculation

VII. PARTICLE IDENTIFICATION AND FINAL STATE SEPARATION

For determining branching fractions and extracting laboratory momentum spectra of τ decay products which can give limits on the polarization of the outgoing τ's (see chapter II.2) it is neccessary to separate the various τ decay channels.

This has been done for the one prong channels $\tau \to e\nu\nu$, $\mu\nu\nu$, and $\pi\nu$.

To extract momentum spectra one has to determine selection efficiencies and misidentification probabilities per momentum bin.

The starting point was the decay product identification from the scan. Each one prong decay was classified as electron (e), minimum ionizing track ($\mu\pi$), track with hadronic shower (π), or "ρ", defined as non showering track with additional photon(s).

If one wants to determine efficiencies and misidentification probabilities, this eye judgement is not appropriate. Therefore well defined cuts were formulated to separate e's from π's, π's from μ's, and π's from ρ's. For an overview of the data flow in this decision process see Figure 40 on page 62.
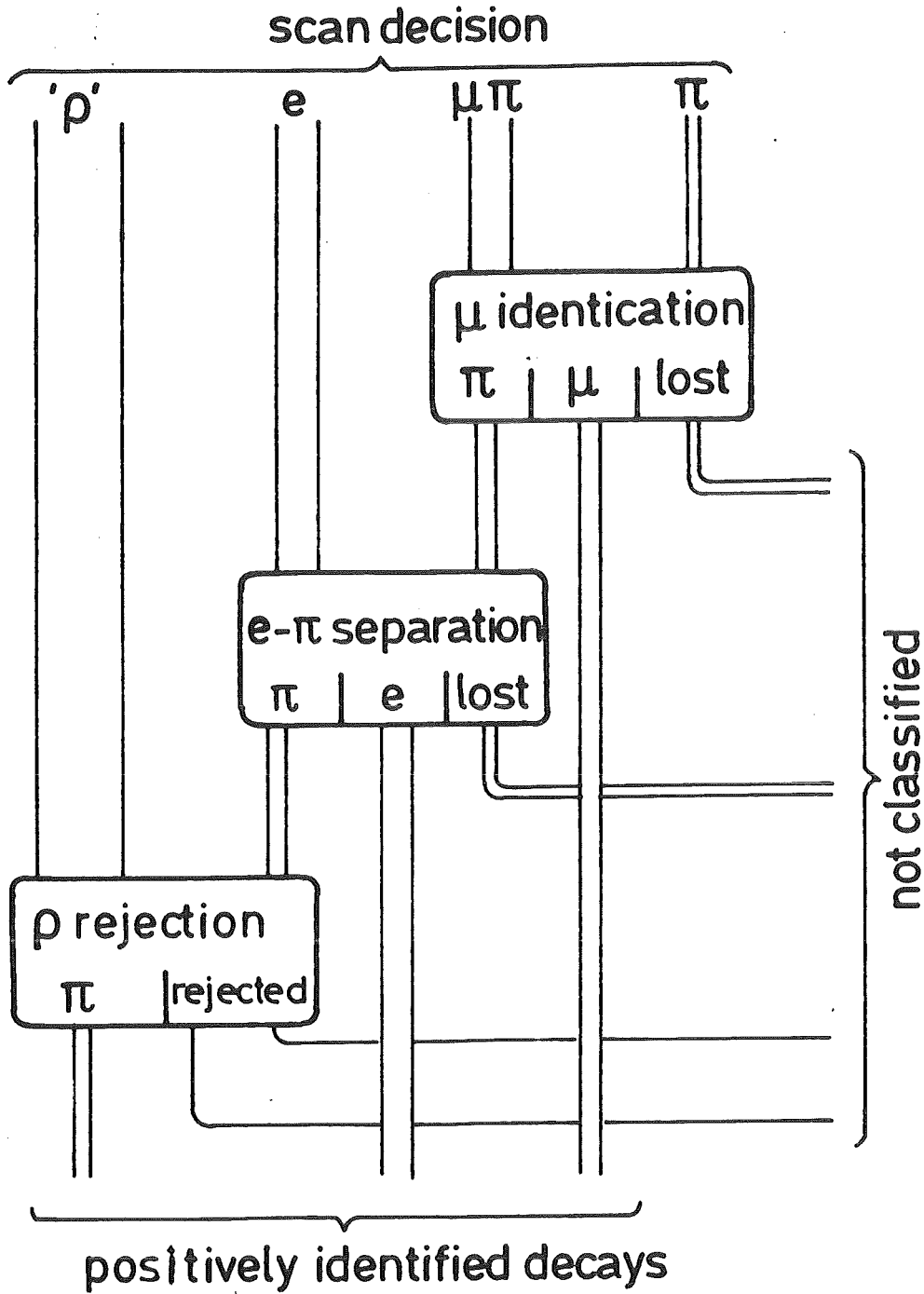
Figure 40. Data flow in particle identification decision. For more details of the separation cuts see text. The thickness of the lines indicates the number of particles in each pass.

a.) μ Identification

Muons and pions were separated using the fact that muons penetrate the iron absorber and reach the muon chambers while pions are absorbed in the iron.

The following requirements were made:

*   track momentum > 2 GeV to make shure that the μ has sufficient energy to penetrate the absorber

*   the track has to point into a working muon chamber (fiducial area cut). The μ chamber coverage within the track acceptance definition ($|\cos \Theta| < .85$) was 83 %.

i.e. tracks with p < 2 GeV or tracks which don't point into an operating muon chamber were discarded.

The charged track is extrapolated through the detector material (coil, calorimeter, iron absorber) into the muon chambers. The error in the extrapolation due to both multiple scattering and the error in momentum measurement is calculated.
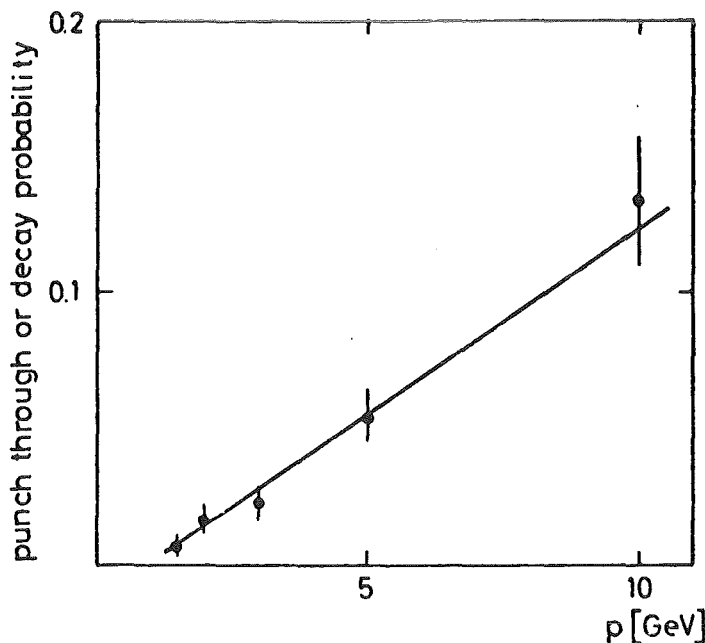
Figure 41.   Pion punch through and decay probability. Errors are statistical only. An additional systematic error of 50 % has been added.

For a track to be identified as a muon it is required to have a hit in the muon chamber within 3 σ from the extrapolated crossing point. All other tracks were treated as pion candidates.

We have two sources of misidentification:

- muons are misidentified as pions due to inefficiencies in the muon chamber system. The chamber efficiencies have been determined experimentally chamber by chamber using cosmics. The overall efficiency of the system has been calculated using a solid angle coverage weighted mean of the single chamber efficiencies to (96 ± 4) %.

- pions are misidentified as muons by giving a signal in the muon chambers either because of punch through or due to decay in flight. This background was estimated by a full Monte Carlo simulation of the behaviour of pions in the detector material. This study was not completely finished at the time this analysis was done. Therefore, to be conservative, I added a 50 % systematic error on the preliminary $\pi \to \mu$ misidentification probability. Figure 41 on page 63 shows the momentum dependence of pion punch through and decay.

  Since this process gives only a small correction to the μ spectrum anyway, and the errors are dominated by statistics, this crude determination of $p_{\pi-\mu}$ is completly sufficient.

b.)　　e-π Separation

Electrons and pions were separated with the help of their characteristic showering behaviour in the calorimeter. Electron showers start early, are relatively narrow and the full energy is deposited in the calorimeter. In contrast pions pass the calorimeter as minimum ionizing tracks until they undergo an hadronic interaction, starting a wide shower which is in general not contained in the calorimeter (roughly 50 % of the pions start a shower inside the calorimeter, the other look just like minimum ionizing particles).

So mainly two cuts were applied to separate electrons from pions, namely a cut in the shape of the longitudinal shower development and a cut in the ratio of calorimetric energy to track momentum.

First I required

- a track momentum above 1 GeV

- the track has to enter the fiducial volume of a calorimeter stack.

If there was no shower associated with the track the particle was considered as pion. If there was a linked shower, at most one more shower in the vicinity of the track was allowed (sometimes the electron radiates a photon, or showers are split by the reconstruction program). If the additional shower was less than 5.5 cm apart from the one linked to the track, its energy was added to the calorimetric energy associated with the track.

Then a shape factor S was defined as the ratio of the energy deposition in the first two lead layers ($< 5 \; X_0$) to the total shower energy and a combined cut in shower shape and energy-momentum matching was done to separate electrons from pions (see also Figure 42 on page 66)

To improve in electron-hadron separation only the energy deposited in the first 3 lead layers ($< 11 \; X_0$) was considered. Most of the electromagnetic shower of an electron is contained within this depth, whereas pions start an hadronic interaction in general late in the calorimeter.

For electrons

- E(calorimeter) / p(ch. tracks) > .56　　　and

- shape factor S > 20 %

was required. Oppositely for π's we asked for
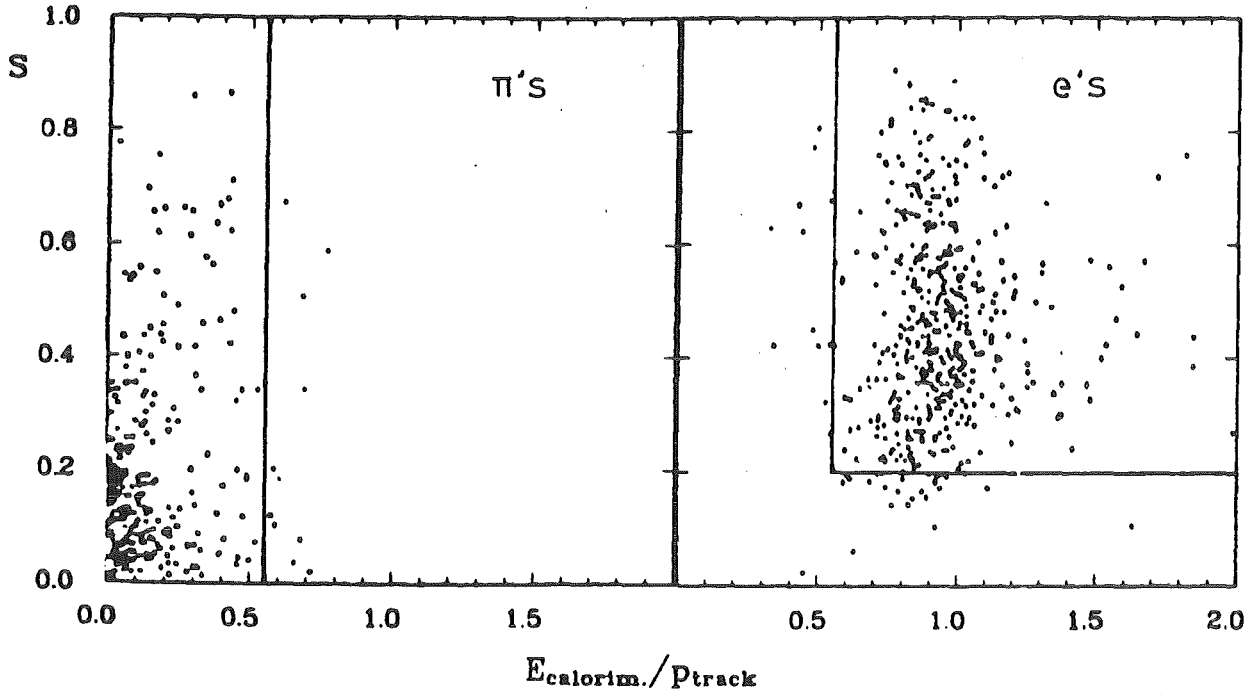
Figure 42. Shape factor S (see text) over energy/track momentum:
a.) pions from τ decay
b.) electrons from τ decay
Also shown are the separation cuts.

• E(calorimeter) / p(ch. tracks) < .56

Tracks which don't fulfill either criterion were not classified. With these cuts a momentum independent efficiency of ~ 95 % for electrons and ~ 88 % for pions was achieved. These numbers dont't take into account the track acceptance cuts. The $\pi \to e$ misidentification probability is $p_{\pi-e}$ ~ 1.5 % and $p_{e-\pi}$ ~ 2 %.

c.) ρ Rejection

The decay $\tau \to \rho\nu \to \pi\pi^0\nu$ represents a considerable background for the decay into a pion since it can for instance happen that the π^0 has very low energy or that it decays very asymmetrically and the high energetic photon escapes detection. An other reason is that there are almost three times as many ρ's as π's, on the one hand because of the larger branching fraction into ρ and on the other because the photons from the π^0 decay trigger the energy requirements of the prefilter.

From these considerations it is obvious that it is neccessary to define cuts for ρ rejection and determine the $\rho\to\pi$ misidentification probability.

First I required

* a momentum greater than 2 GeV   and

* the track entering the calorimeter's fiducial volume

Then I consider all showers within a cone of 45° half opening angle not assciated to the track. To include also those pions whose fragments of the hadronic shower fake photons, up to two additional showers are allowed if the invariant mass between all the showers and the track is less than 200 MeV. (see Figure 43 on page 68)

A Monte Carlo simulation tells us that the pion efficiency of this procedure is $\varepsilon_\pi \sim 85$ %. The $\rho\to\pi$ misidentification probability is $p_{\rho-\pi} \sim 8$ %.
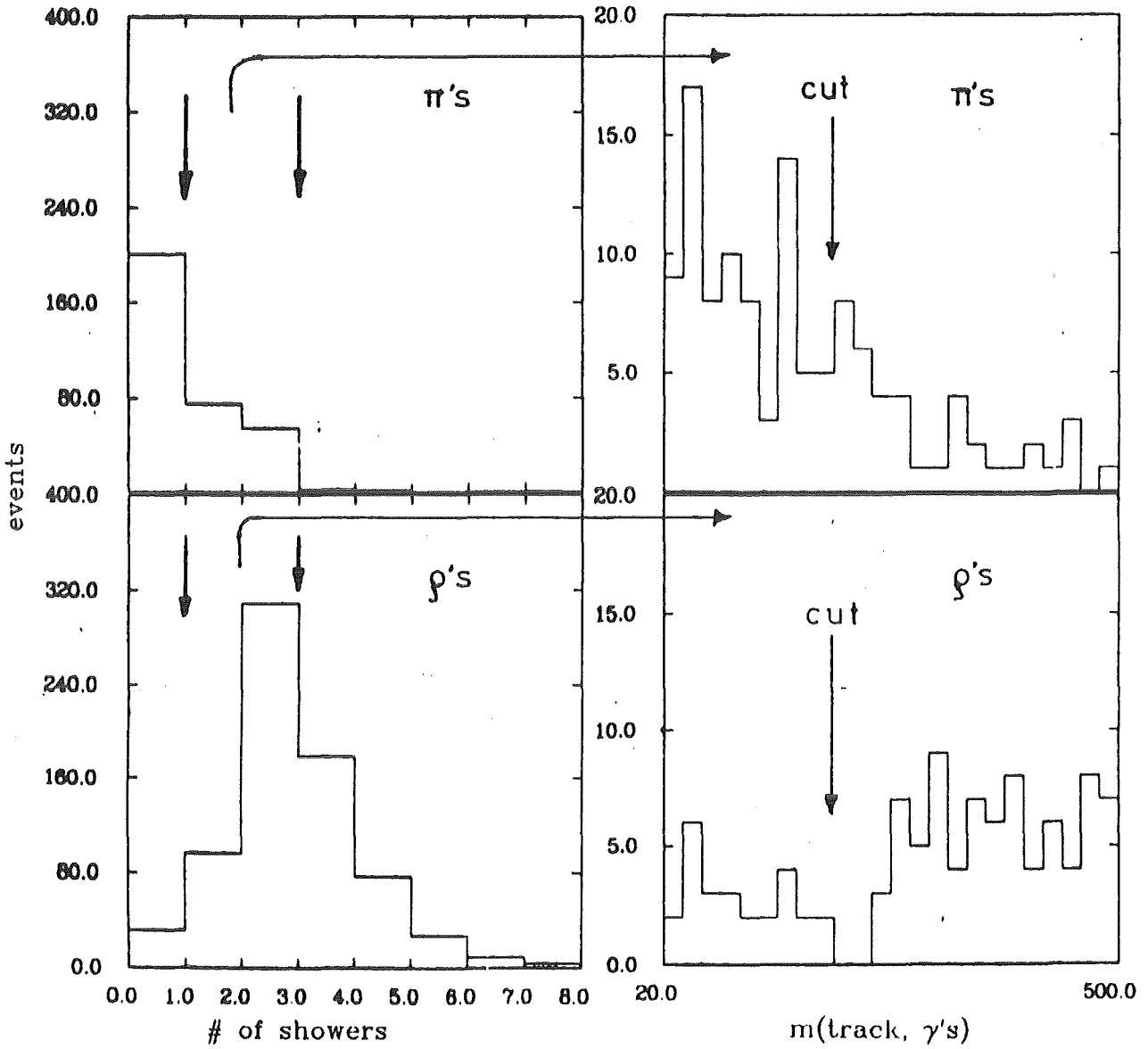
Figure 43. Cuts for rho rejection:
 top: pions
 bottom: all π + $\geq$ 1 π^0 final states
On the left the number of 'showers' in a 45° half opening
angle cone around the track is shown.
The right hand side shows the invariant mass between
track and showers for $1 \leq n_{sh} \leq 2$

A scan of Monte Carlo τ pair events showed that no ρ's were wrongly classified as electrons. From this I concluded that the $\rho \to e$ misidentification probability is small.

Figure 44 summarizes the three τ decay samples, identification efficiencies, and background contributions. Figure 45 on page 70 shows the uncorrected lab. momentum spectra.

channel	# of cand.	ε [%]	# π	# e	# μ	# π + ≥1 π^0
$\tau \to \pi\nu$	34	47.5 ± 4.4		.7 ± .7	1.4 ± 1.4	5.4 ± 1.2
$\tau \to e\nu\nu$	60	72.9 ± 4.1	.5 ± .5		0	< .5
$\tau \to \mu\nu\nu$	47	64.0 ± 4.6	4.6 ± 2.0	0		< .5

Figure 44.   Summary of the three τ decay samples, Identification efficiencies (number of positively identified decays over total number expected in the τ pair sample), and background contributions.
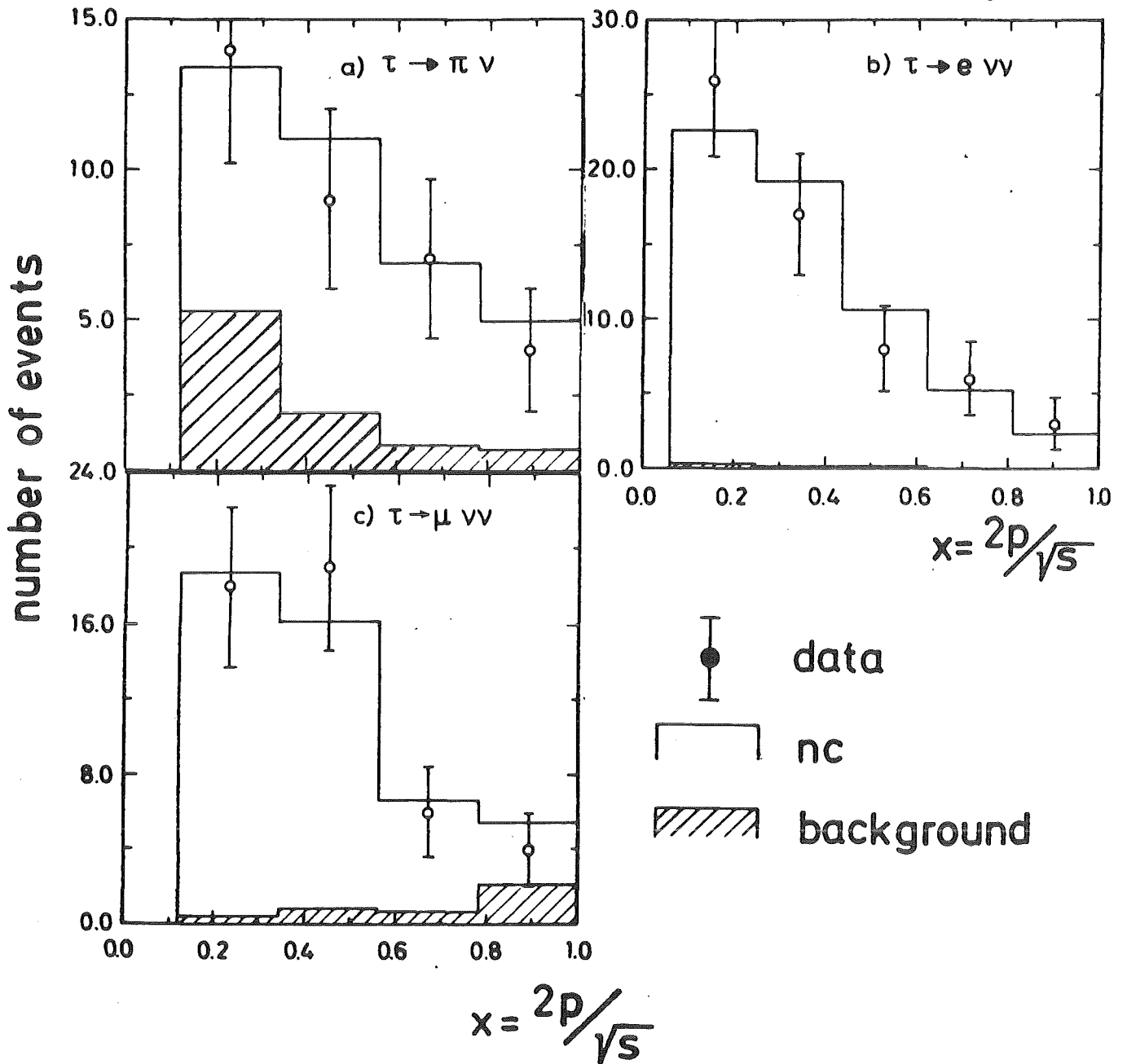
Figure 45.   Uncorrected lab. momentum spectra,   all decays with p > E_{beam} were put into the last bin.

In both e-π separation and ρ rejection one has to rely heavily on the correct Monte Carlo simulation of electromagnetic and hadronic showers in the liquid argon calorimeter.   Therefore it is essential to have a good understanding of the Monte Carlo and to test it as thoroughly as possible.

The simulation electromagnetic showers I have checked carefully by comparing Monte Carlo generated electrons to one prong electron data, mostly from radiative Bhabha scattering. The agreement was found to be excellent (see Figure 46 on page 71 and Figure 47 on page 72)

The case is more difficult for hadronic showers since it is very hard to find a clean sample of high energy pions. We did content ourselves with a few events from the τ decay channel $\tau \to \rho\nu \to \pi\pi^0\nu$ were the pion is tagged the accompanioning photons from π^0 decay. Besides the small statistic one has also the problem of pion-photon overlap. Within the very limited statistical accuracy the agreement between Monte Carlo and data is good (see also /33/)

For the hard particle spectra from τ decays also a good understanding of the momentum resolution is essential. It has been studied by looking into large angle Bhabha scattering events (see " 2.1 Inner Detector" on page 29) and it has been made shure that the Monte Carlo reproduces the momentum resolution observed in the data.
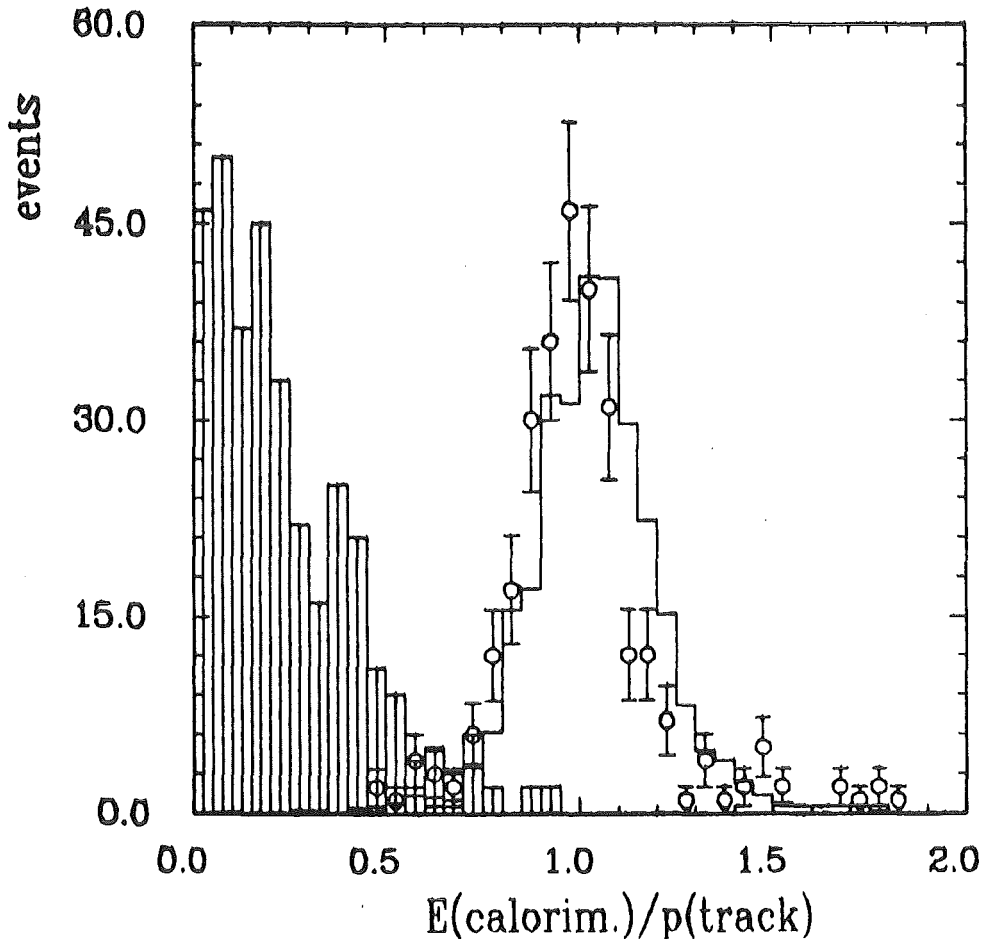
Figure 46. Calorimetric energy / track momentum, electrons and pions (shaded).
Histograms are MC simulation, points with error bars are electron data.
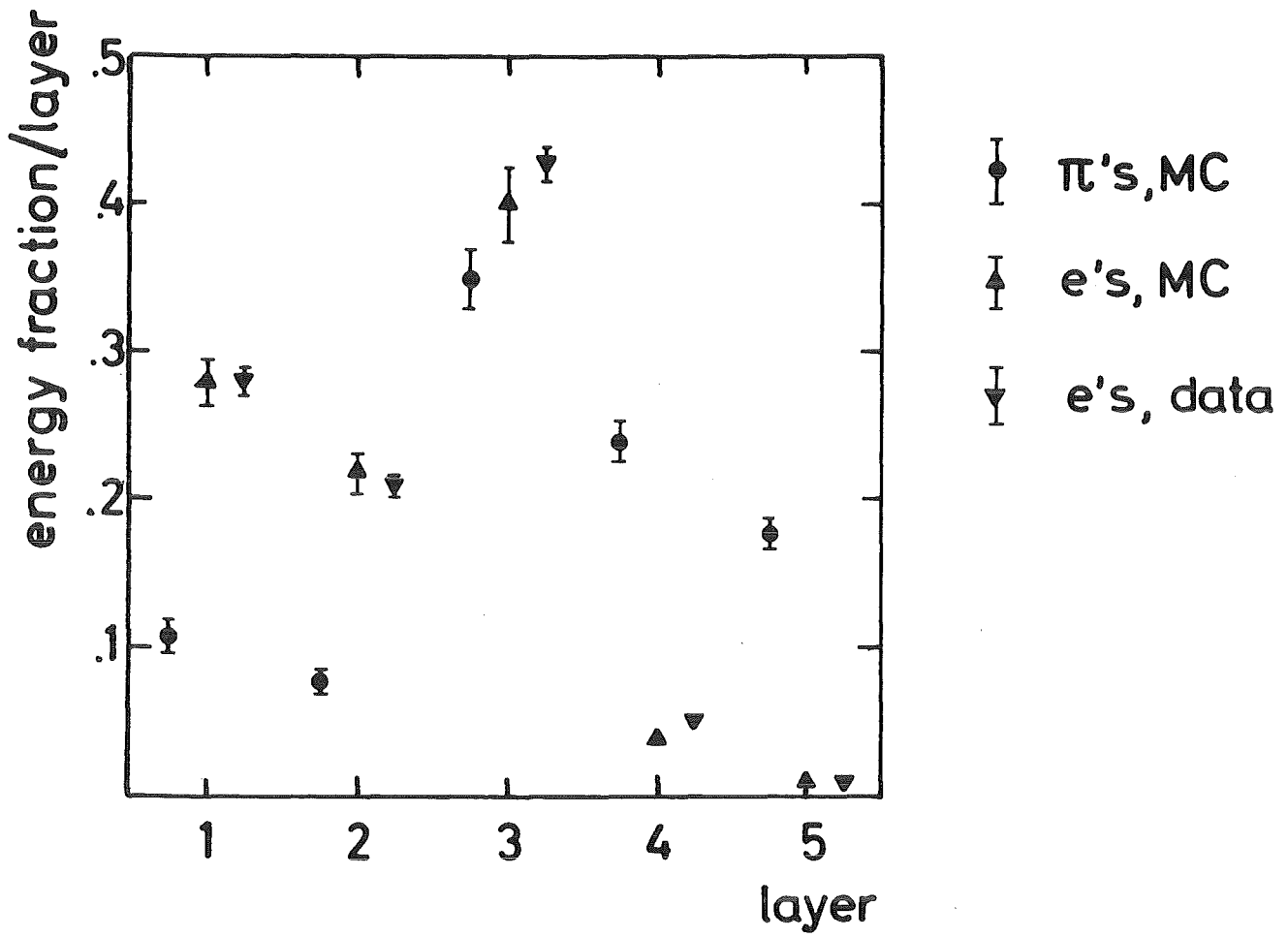
Figure 47. Longitudinal shower development measured by the fractional energy deposition in the five lead layers.

1. TOTAL CROSS SECTION

By combining the number of observed τ pairs with the τ acceptance and the luminosity determined from large angle Bhabha scattering I obtain

$$R_\tau = \sigma_{\tau\tau}/\sigma_{point} = .94 \pm .06(\text{stat.}) \pm .06(\text{syst.})$$

Small corrections have been applied for background contamination ($-(2.5 \pm 1.0)$ % each for hadronic events and τ pairs from 2 photon collisions) and scanning losses $+(2.0 \pm 2.0)$ %.

The systematic error is due to luminosity determination (3.5 %), background contributions (2 %), scanning losses (2 %), radiative corrections (2 %), and uncertainties in acceptance calculation (4 %). They are added in quadrature.

This cross section can be translated in the following values for the cutoff parameter Λ (see " 1.1 Production" on page 6):

$$\Lambda_- = 103 \text{ GeV}$$
$$(95 \text{ % confidence level})$$
$$\Lambda_+ = 151 \text{ GeV}$$

In other words: the τ, a particle twice as massive as the proton, behaves pointlike down to distances of $2 \cdot 10^{-3}$ fm, and QED is valid up to momentum transfers squared of $Q^2 \sim 1200$ GeV.

2. DIFFERENTIAL CROSS SECTION AND A(τ)

To obtain a differential cross section it is neccessary to determine both the τ direction of flight and the charge sign of at least one of the τ's. In 240 out of 242 events a charge assignment was possible. Only those events have been considered in the differential cross section. The polar range has been restricted to $|\cos \Theta| < .8$ to avoid edge effects.

The event axis is defined as the vector difference of the two jet momenta which in turn are the vector sum of the charged τ decay products. Figure 48 shows the angle between the event axis of the τ^+ and τ^- and the event axis determined from the observed charged decay products. One sees immediately that at these energies the τ decay products are boosted sufficiently to reconstruct the original τ direction.

A small positive asymmetry (+1.1 % within our acceptance and acolinearity cuts) is caused by higher order QED diagrams which were not included in the original τ pair generator. A correction for this small effect has been applied to the angular distribution /12/. Figure 49 on page 75 shows the differential cross section corrected for acceptance and higher order QED contributions. The dashed line is a fit of pure QED to the data, the solid line corresponds to QED + electro weak contributions, allowing a forward
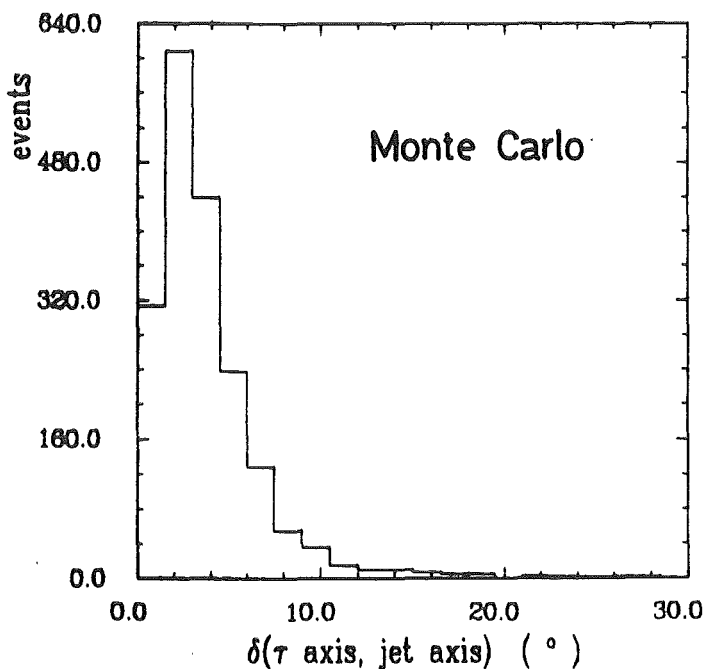
Figure 48. Angle between $\tau^+\tau^-$ events axis and event axis determined from   the observed charged decay products.
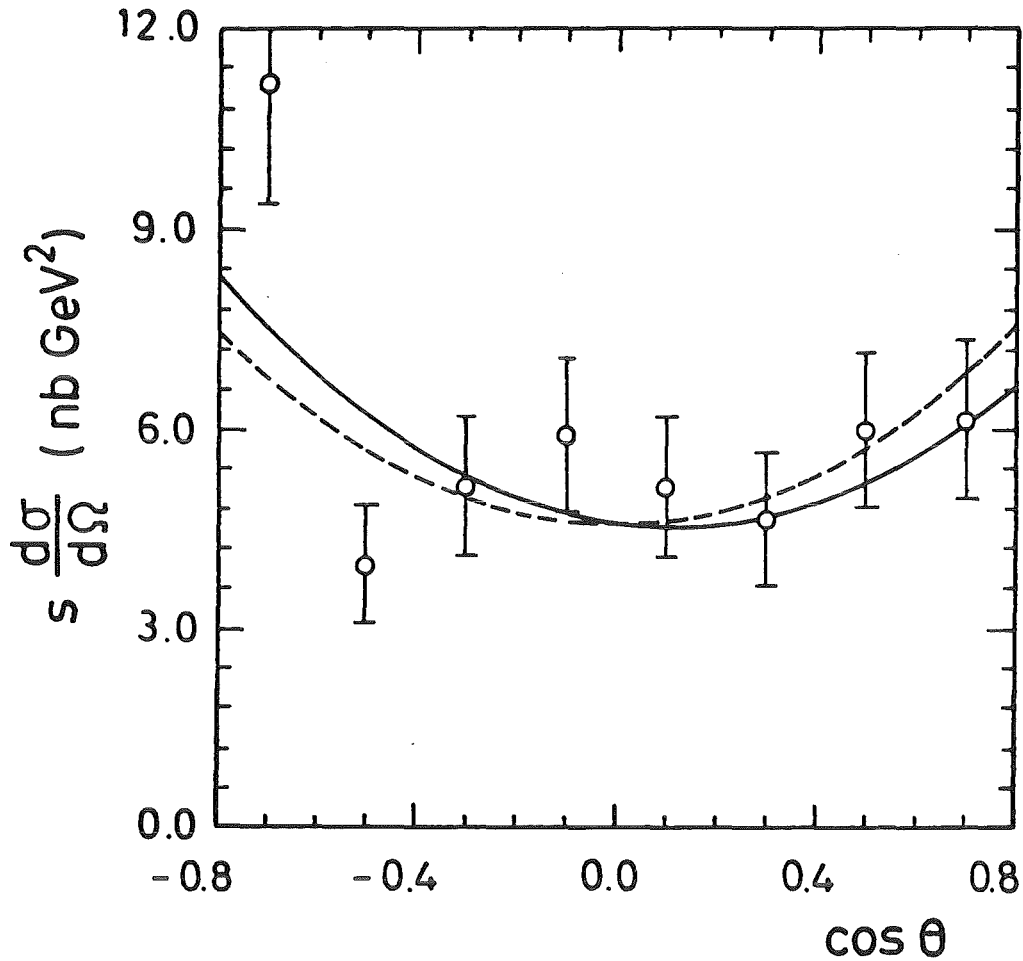
Figure 49. τ pair differential cross section corrected for acceptance and higher order QED contributions.

- dashed line: fit of pure QED $\propto (1 + \cos^2\Theta)$ to the data
- solid line: fit of electro weak interference to the data

backward asymmetry. Figure 50 on page 76 shows the quantity $A_\tau(\cos \Theta) \cdot (1 + \cos \Theta)$. A fit yields an asymmetry over the full solid angle of

$$A_\tau = - (9.0 \pm 6.6) \, \%$$

in good agreement with the Standard Model prediction of -9.3 %.

The systematic errors due to wrong charge assignment or background contributions are small and have been estimated to be less than 1.5 %.
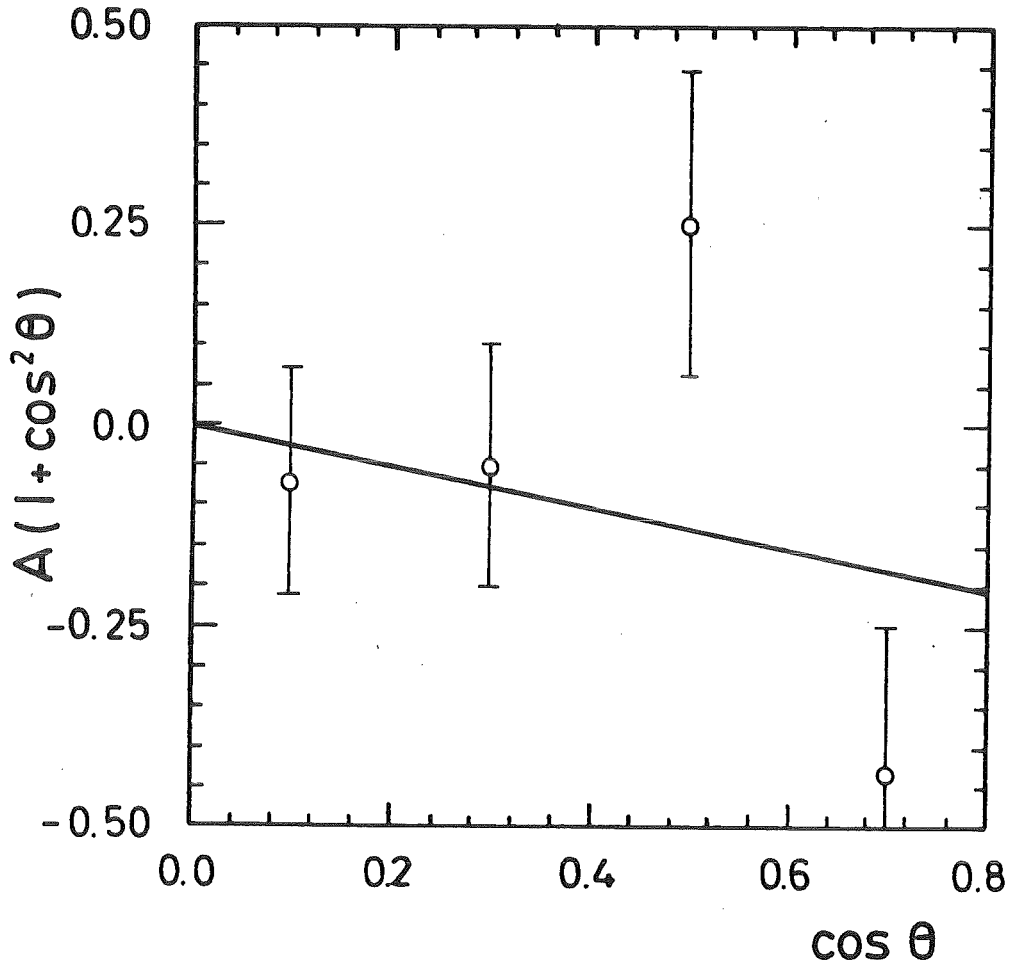
Figure 50. Forward backward charge asymmetry. The line is a fit to the data and corresponds to an integrated asymmetry of – 9.0 %.

Combining this asymmetry measurement with the value of $a_e = -1.06 \pm .07$ measured in νe scattering one obtains for the axial vector coupling of the τ to the weak neutral current

$$a_\tau = -.94 \pm .69$$

3. BRANCHING RATIOS

τ branching ratios have been measured at both SPEAR and DORIS. (see Figure 8 on page 14 and references therein) At higher center of mass energies far above the production threshold, however, the signature of $\tau^+\tau^-$ events is much cleaner, offering for the first time the possibility to extract a virtually background free sample of τ pairs incorporating all decay topologies. Since all τ decay channels are observed it was possible to normalize the branching ratios to the actually observed number of τ pairs rather than to QED expectation. Therefore, the systematic errors due to normalization or background subtraction are quite different from previous measurements. This was demonstrated for instance by recent measurements of topological branching fractions at PETRA and PEP /36, 37/. They differ considerably from earlier determinations at SPEAR and DORIS /17.1/.

Combining the number of observed decays with identification efficiencies, expected background contamination, and the total number of observed τ pairs I obtain

$$B(\tau \to \pi\nu) = .099 \pm .017 \pm .013$$
$$B(\tau \to e\nu\nu) = .183 \pm .024 \pm .019$$
$$B(\tau \to \mu\nu\nu) = .176 \pm .026 \pm .021$$

where the first error is statistical and the second one systematic.

The systematic errors are due to efficiency calculation and background subtraction. (see Figure 44 on page 69) An additional error of 8.5 % is due to the overall normalization to the total number of observed τ pairs.

Since we don't distinguish experimentally K's from π's I subtract a contribution from the Cabbibo suppressed decay $\tau \to K\nu$ in the branching ratio into pions. The subtraction of the measured branching fraction $B(\tau \to K\nu)$ = .013 $\pm$ .005 /17.3/ causes an additional systematic error of 6 %.

4. INCLUSIVE DECAY PRODUCT SPECTRA, V(τ), AND H(VA)

Both total cross section and forward-backward asymmetry are parity con-
serving quantities. To look for parity violation in e^+e^- physics one has to
study polarization effects. Since e^+e^- machines with longitudinally
polarized beams are not avilable at present, the only way to observe parity
violating effects is to look for final state polarization.
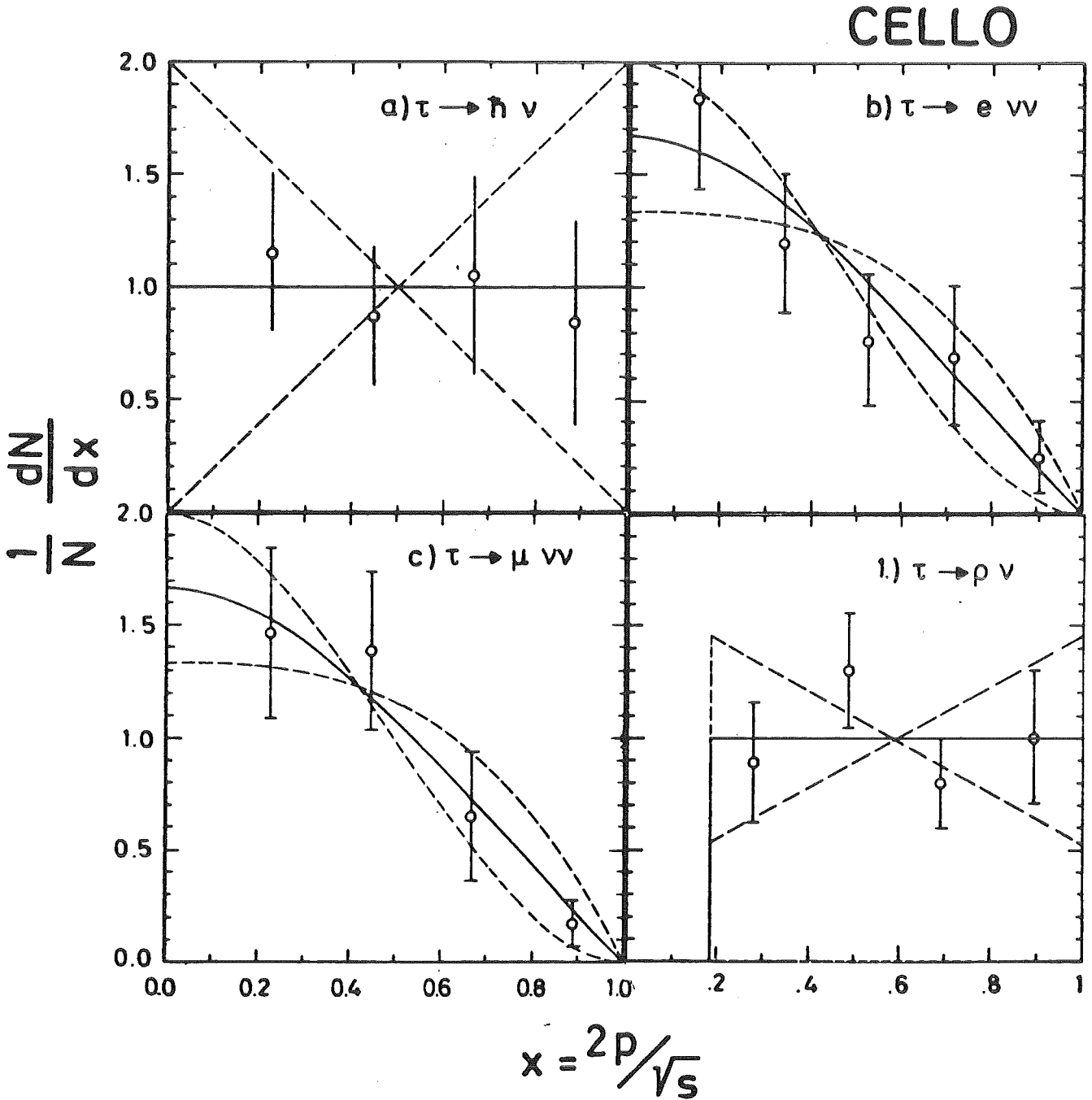
Figure 51.   Inclusive τ decay product spectra,   acceptance corrected
- solid line: no polarization
- broken lines: ± 100 % polarization

One excellent candidate for this is the τ which weak decay can be used as a polarization analyzer. A possible τ polarization would be reflected in the inclusive decay product spectra (see " 2.   Using the τ as a Probe for Electro Weak Interference" on page 17). Therefore, one can use these spectra to measure this polarization.

Inclusive spectra are obtained by applying efficiency and background corrections per momentum bin. (see Figure 51 on page 78) In the polarization fits I will include the ρ spectrum from the decay $\tau \to \rho\nu$ which has been extracted by C. Kiesling. A description of the ρ identification procedure can be found elsewhere /38/.

A combined fit to all four spectra yields a forward backward averaged mean polarization $<P_\tau> = (P_F + P_B)/2$ of

$$P_{\tau-} = -.14 \pm .22.$$
$$\text{or}$$
$$-.58 < P_\tau < .30 \qquad 95 \ \% \ \text{confidence level}$$

The polar angle dependance of τ polarization gives us a handle on the τ's vector coupling to the weak neutral current. (see chapter II.2) If one takes a_e and v_e from νe scattering data (see Figure 10 on page 18) and a_τ from the measured charge asymmetry in $e^+e^- \to \tau^+\tau^-$ ($a_\tau = -.68 \pm .24$ from the combined PETRA data), i.e. using only purely leptonic processes, it is possible to derive limits on v_τ. A fit of the four spectra of τ decay products separately for forward and backward direction gives a polarization forward backward asymmetry $A_{P\tau} = (P_F - P_B)/2$ of $A_{P\tau} = -(1 \pm 22)\%$ corresponding to

$$v_\tau = -0.0 \pm 2.9$$
$$\text{or}$$
$$-5.8 < v_\tau < 5.8 \qquad 95 \ \% \ \text{confidence level}$$

channel	v_τ	h_{VA}
$\tau \to \pi\nu$	-6.4 ± 4.4	$-.33 \pm .61$
$\tau \to e\nu\nu$	4.8 ± 8.3	$.13 \pm 1.15$
$\tau \to \mu\nu\nu$	-3.0 ± 7.8	$-.15 \pm .97$
$\tau \to \rho\nu$	7.8 ± 5.3	$-.49 \pm .92$
all 4 ch.	0.0 ± 2.9	$-.25 \pm .42$

Figure 52.   Fit results for $v+_\tau$ and h_{VA}

This measurement of v_τ can be compared with $v_e = -.04 \pm .06$ from νe scattering data. Within the large errors our result is compatible with universality.

For the contributions of the single decay modes see Figure 52 on page 79. One sees that the semihadronic two body decays give the most severe constraint, but the lepton channels also contribute significantly.

Another possibility to limit v_τ is to look at the total cross section:

$$R_\tau = 1 + 2X \cdot v_e v_\tau + X^2(a_e^2 v_\tau^2 + a_e^2 a_\tau^2 + v_e^2 v_\tau^2 + v_e^2 a_\tau^2) .$$

Note that the interference term gives no constraint on v_τ since v_e experimentally is compatible with zero. But a purely weak term $\propto a_e^2 v_\tau^2 X^2$ turns up where X is the propagator term, X(34 GeV) = -.06. (see chap. II.2)

From the total cross section measurement we get $R_\tau < 1.17$ (95 % C.L.) which leads to $-10.8 < v_\tau < 14.9$ (95 % C.L.) taking into account the uncertainty in the measurement of v_e in νe scattering.

It is interesting to compare our limit on v_τ with a recent first measurement of v_μ performed by the BCDMS collaboration at CERN using polarized
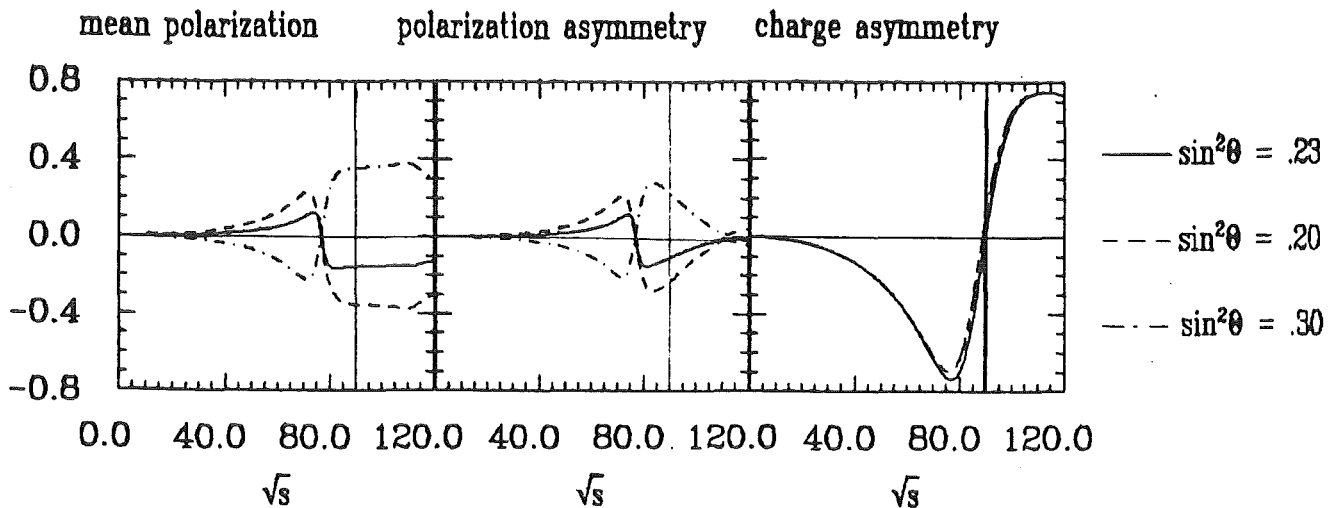
Figure 53. Energy dependence of
lepton mean polarization : $(P_F + P_B)/2$,
polarization asymmetry $(P_F - P_B)/2$,
and lepton charge asymmetry
for three values of the Weinberg angle. The Z^0 mass
(assumed to 90 GeV) is indicated by the vertical bar. In
the Standard Model the charge asymmetry practically
vanishes on the Z^0.

muons scattered on a carbon target /39/. They measure the asymmetry of the cross sections for positively polarized μ^- or negatively polarized μ^+ on carbon. Combining this measurement with PETRA data on μ pair charge asymmetry one obtains $v_\mu = -.24 \pm .32$, though this is not a purely leptonic process and one has to assume the quark axial vector couplings predicted by the Standard Model.

It is worth noting that the error on P_τ and thus on v_τ is completely dominated by statistics. A high statistics (~ 100 pb^{-1}) experiment at $\sqrt{s} = 42$ GeV could improve the error on v_τ by a factor of ~ 5.

Most interesting, however, will be a measurement of τ final state polarization on the Z^0 resonance. Here the mean polarization is dominated by a term $(v_e^2 + a_e^2)v_\tau a_\tau$. A measurement of this quantity will allow a precision determination of the mixing between electromagnetic and weak neutral current in a purely leptonic reaction, independent of the mass of the neutral vector boson. The other observables in lepton pair production, namely charge asymmetry and total cross section, are not very sensitive to $\sin^2\Theta_W$ (see Figure 54). Moreover, in both quantities the vector coupling enters squared, thus making impossible to resolve the ambiguity on $\sin^2\Theta_W$ around 1/4. On the other hand, a precision measurement of both
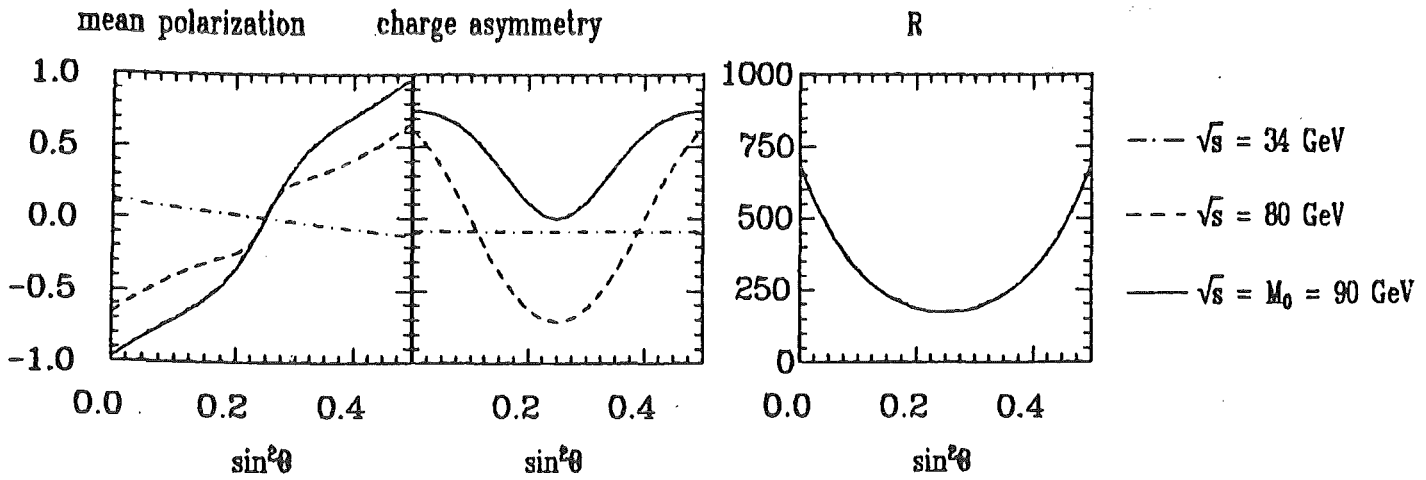
Figure 54. Sensitivity of
lepton mean polarization, :
lepton charge asymmetry,
and total cross section
on the Weinberg angle at $\sqrt{s} = 34$, 80, and 90 GeV (M_0). The polarization is very sensitive on $\sin^2\Theta_W$. Moreover, it is apparent that only in the polarization measurement it will be possible to resolve the ambiguity on $\sin^2\Theta_W$ around 1/4.

v_τ and the relative sign of the vector and axial vector couplings will be possible.

Assuming that the polarization could be measured with a systematic uncertainty of 4 % which seems experimentally feasible the precision obtained would be $\Delta(\sin^2\Theta_W) \sim .005$ and $\Delta v_\tau \sim .02$.

Sakurai has parametrized the weak neutral current in e^+e^- annihilation in a model independent way, only assuming universality (i.e. $a_\tau = a_e = a$, $v_\tau = v_e = v$), by introducing three parameters h_{VV}, h_{AA}, and h_{VA} /23/. h_{VV} and h_{AA} are measured in the total cross section and charge asymmetry respectively. Effects measuring h_{VA} are parity violating, i.e. one has to look for polarization effects.

In the interference region h_{VA} is directly proportional to the final state polarization. A fit yields

$$h_{VA} = -.27 \pm .42$$
$$\text{or}$$
$$-1.11 < h_{VA} < .57 \qquad 95\ \%\ \text{confidence level}$$

h_{VA} can be expressed in terms of the lepton couplings, namely $h_{VA} = C\ a\cdot v$. If factorization holds one expects in the Standard Model $C = 1/4$. The above measurement can be compared with $1/4\ a\cdot v < .04$ (95 % C.L.), determined from νe scattering. Our measurement is clearly compatible with factorization.

5. CONCLUSIONS

τ pair production has been measured at an energy where electro weak interference effects start to become measurable.

Due to the clean signature of τ events at these energies and the good particle identification and homogeneous acceptance of the CELLO detector a high efficiency selection sensitive to all τ decay channels could be achieved.

Both total and differential cross section have been measured. The latter shows indications of electro weak interference.

Branching ratios of the one prong channels $\tau \rightarrow \pi\nu$, $\tau \rightarrow e\nu\nu$, and $\tau \rightarrow \mu\nu\nu$ have been determined.

From the inclusive momentum spectra of τ decay products for the first time limits on final state polarization have been obtained.

From the polarization measurement the τ's vector coupling to the weak neutral current has been determined, though the errors are still large. Whithin the limited precision of this first measurement v_τ has been found to be in agreement with universality.

h_{VA} measured from final state polarization has been found to be compatible with factorization.

REFERENCES

/1/   M.L. Perl et al., Phys. Rev. Lett. 35(1975),1489; 38(1976),117

/2/   PLUTO coll. (J. Burmester et al.), Phys. Lett. 68B(1977),297; 68B(1977),301

/3/   DASP coll. (R. Brandelik et al.), Phys. Lett. 74B(1978),109

/4/   For a review see
       M.L. Perl, Ann. Rev. Nucl. Part. Sci. 30(1980), 299

       or more recently
       G. Kalmus, Proceedings of the 21st Int. Conf. on High Energy Physics, Paris(1982)

/5/   S. Weinberg, Phys. Rev. Lett. 19(1967),1264

       A. Salam, Proc. 8th Nobel Symposium, Stockholm(1968)

/6/   G.J. Feldmann, SLAC-PUB-2839 (1981)

/7/   S.W. Herb, Phys. Rev. Lett. 39(1977),252

       W.R. Innes, Phys. Rev. Lett. 39(1977),1240

/8/   see for instance
       CELLO coll. (H.J. Behrend et al.), DESY 81/29 (1981)

/9/   S.L. Glashow, Nucl. Phys. 22(1961),579

       A. Salam, J.C. Ward, Phys. Lett. 13(1964),168

/10/   S.L. Adler, Phys. Rev. 177(1969),2426

       M.A.B. Beg, A. Sirlin, Rockefeller University preprint, RU82/B/21 (1982)

/11/   S.L. Glashow, J. Iliopoulos, L. Miani, Phys. Rev. D2(1970),1285

/12/   F.A. Berends, R. Kleiss, Nucl. Phys. B177(1981),237

/13/   Y.S. Tsai, Phys. Rev. D4(1971),2821

/14/   H.B. Thacker, J.J. Sakurai, Phys. Lett. 36B(1971),103

/15/   F.J. Gilman, D.H. Miller, Phys. Rev. D17(1978),1846

/16/   T.N. Pham, C. Roiesnel, T.N. Truong, Phys. Lett. B78(1978),623

/17.1/   Particle Data Group, Phys. Lett. 111B(1982),1

/17.2/   MARK II coll., SLAC-PUB-2839 (1982)

/17.3/   MARK II coll., Phys. Rev. Lett. 48(1982),1586

/17.4/   MARK II coll., Phys. Lett. 109B(1982),119

/17.6/   MARK II coll., Phys. Rev. Lett. (1981),215

/18/   DELCO coll. (W. Bacino et al.), Phys. Rev. Lett. 42(1979),749

/19/   J. Jaros representing the MARK II coll., Proceedings of the 21st Int. Conf. on High Energy Physics, Paris(1982)

/20/   A.M. Cnops et al., Phys. Rev. Lett. 40(1978),144

/21/   P. Fritze et al., Phys. Lett. 96B(1980),427

/22/   new results have been presented by JADE (G. Heinzelmann), MARK J (J. Burger), and TASSO (D. Lüke) at the the 21st Int. Conf. on High Energy Physics, Paris(1982)

/23/   P.Q. Hung, J.J. Sakurai, Ann. Rev. Nucl. Part. Sci. 31(1981),375

/24/   J.E. Augustin, Proceedings of the LEP Summer Study, CERN 79-01, 499

/25/   G. Goggi, Proceedings of the LEP Summer Study, CERN 79-01, 483

/26/   H.D. Bremer et al., DESY 81/26 (1982)

/27/   F.M. Renard, Basics of Electron Positron Collisions, Editions Frontieres, Paris (1981)

/28/   The members of the CELLO collaboration are

H.J.Behrend, Ch.Chen[1], H.Fenner, U.Gümpel, M.-J.Schachter, V.Schröder, H.Sindt
Deutsches Elektronen Synchroton, DESY, Hamburg, Germany

G.D'Agostini, W.-D.Apel, S.Banarjee, J.Bodenkamp, J.Engler, G.Flügge, D.C.Fries, W.Fues, K.Gamerdinger, G.Hopp, H.Küster, H.Müller, H.Randoll, G.Schmidt, H.Schneider
Kernforschungszentrum und Universität Karlsruhe, Karlsruhe, Germany

W. de Boer, G.Buschhorn, G.Grindhammer, P. Grosse-Wiesmann, B.Gunderson, C.Kiesling, R.Kotthaus, U.Kruse[2], H.Lierl, D.Luers, H.Oberlack, P.Schacht
Max Planck Institut für Physik und Astrophysik, München, Germany

P.Colas, A.Cordier, M.Davier, D.Fournier, J.F.Grivaz, J.Haissinski, V.Journe, A.Klarsfeld, F.Laplanche, U.Mallik, J.-J.Veillet
Laboratoire de l'Accelerateur Lineaire, Orsay, France

J.H.Field[3], R.George, M.Goldberg, B.Grossetete, O.Hamon, F.Kapusta, F.Kovacs, G.London, L.Poggioli, M.Rivoal
University of Paris, Paris, France

R.Aleksan, J.Bouchez, G.Carnesecchi, G.Cozzika, Y.Ducros, A.Gaidot, Y.Lavagne, J.Pamela, J.P.Pansart, F.Pierre
Centre d'Etudes Nucleaires, Saclay, France

December 1982

[1] Visitor from the Institute of High Energy Physics, Chinese Academy of Science, Peking, People's Republic of China
[2] Visitor from the University of Illinois, Urbana, USA
[3] On leave of absence from DESY, Hamburg, Germany

/29/ CELLO coll. (H.J. Behrend et al.), Physica Scripta 23(1980),610

/30/ H.J. Behrend, Comp. Phys. Comm. 22(1981),365

/31/ C. Jacobs, L. McCulloch, CERN 1976, unpublished

/32/ P. Grosse Wiesmann, PhD thesis

/33/ C. Kiesling, CELLO note M-123 (1982), unpublished

/34/ EGS, R.L. Ford and W.R. Nelson, SLAC report 210 (1978)

/35/ HETC code, RSIC Cmputer Code Collection, Oak Ridge National Laboratory, CCC-178

/36/   CELLO coll. (H.J. Behrend et al.), Phys. Lett. 114B(1982),282

/37/   MARK II coll. (C.A. Blocker et al.), Phys. Rev. Lett. 49(1982),1369

/38/   CELLO coll. (H.J. Behrend et al.), DESY 83/19 (1983), to be published

/39/   A. Argento et al., Phys. Lett. 120B(1983),245